Contents

List of Figures

List of Tables

Abbreviations

CVD	Chemical vapor deposition
DLTS	Deep-level transient spectroscopy
EBD	electron beam deposition
EBE	Electron beam exposure
FET	Field effect transistor
FWHM	Full width at half maximum
LA	Longitudinal acoustic
LO	Longitudinal optical
LED	Light emitting diode
L-DLTS	Laplace-transform deep-level transient spectroscopy
MBE	Molecular beam epitaxy
MFC	Mass flow controller
MOCVD	Metallo-organic chemical vapour deposition
MOS	Metal oxide semiconductor
MS	Metal semiconductor
RE	Resistive evaporation
RBS	Rutherford backscattering spectrometry
SBD	Schottky Barrier diode
SRIM	Stopping range of ions in matter
TA	Transverse acoustic
TO	Transverse optical
UV	ultra violet
XRD	X-ray diffraction

Physical Constants

Boltzmann constant	k	=	$1.380\ 658 \times 10^{-23}$ JK^{-1}
Elementary charge	e	=	$1.602\ 177 \times 10^{-19}$ C
Electron rest mass	m_e^*	=	$9.109\ 390 \times 10^{-31}$ kg
Electron-volt energy	eV	=	$1.602\ 177 \times 10^{-19}$ J
Vacuum permittivity	ϵ_0	=	$8.854\ 188\ 58 \times 10^{-14}$ C^2 $\mathrm{N.m}^{-2}$
Planck's constant	h	=	$6.626\ 076 \times 10^{-34}$ Js
Exponential constant	exp	=	2.718 282
Pi	π	=	3.141 593

Symbols

I-V	Current-voltage
C-V	Capacitance-voltage
A.C.	Alternating current
D.C.	Direct current
ϕ_{Bn}	Schottky barrier height
ϵ_s	permittivity of a semiconductor
ϕ_{IV}	I-V barrier height
ϕ_{CV}	C-V barrier height
$\rho(x)$	Charge density of a semiconductor
$\phi(x)$	Electrostatic potential
ϕ_m	Metal work function
χ_s	Electron affinity of a semiconductor

Kuna baba na amai

Chapter 1

Introduction

Silicon carbide has become the backbone of the power electronics industry. The first known device made from the material was a solid state detector patented by Dunwoody in 1906. It was a point contact diode for receiving radio waves. A year later, Pierce (1907) presented the first current-voltage characteristics showing diode rectifying behavior. Since then, several milestones have been reached in improving the semiconductor in order to attain an optimum quality, suitable for commercial electronic applications. Today it is used to produce small high voltage devices with higher efficiencies and minimal losses when compared to those made from elemental semiconductors.

As the demand for faster, high power miniature devices continues to grow, SiC finds itself as a suitable candidate for newer co-integrated technologies which have multiple applications. The main challenge in the growth of silicon carbide has been a difficulty in controlling the processes involved resulting in crystals with a high defect density. Micropipes and some native intrinsic defects are almost always present in electronics grade wafers (Nakamura *et al.*, 2004). The problem is compounded by the metastability of some of these defects which change configuration under various conditions. An understanding of the impact of defects on device properties is essential for successful device design and fabrication.

Defect studies are particularly important in SiC because of the identification of a room temperature single photon source in the material by Castelletto *et al.* (2014) which was linked to the carbon antisite-vacancy pair ($C_{Si}V_C$). The defect has immense potential for use in quantum computational applications. However, research still needs to be done in device implementation and to establish sound fabrication protocols.

1.1 Motivation

A detailed account of growth, implantation and process induced defects, their identification and characterization is given by Kimoto and Cooper (2014). Claeys and Simoen (2013) gave a summary of the irradiation induced defects and their formation mechanisms. In both narratives, the future of 4H-SiC looks promising but many challenges are also presented. The general consensus which is also shared in many other publications was that defects are detrimental for device performance in the semiconductor and must be eliminated (Hemmingsson *et al.*, 1998b). Since then there has been major improvements in measurement techniques, instrument resolution and growth techniques. Further, defects have been shown to play major beneficial roles in novel SiC technologies (Castelletto *et al.*, 2015). Thus, there is a need to apply physics principles in defect studies so as to positively exploit them.

Metalization is a crucial processing step in the semiconductor industry. Several studies have reported that deposition techniques with high energy incident particles introduce electrically active defects in semiconductors. Most of these defects have been shown to be detrimental to device performance. From a defect engineering perspective, however, incident particles have been used to induce defects that have been used for refined control and to optimize semiconductor device performance (Seebauer and Noh, 2010). It is therefore important to investigate if the incident particles which emanate from metal deposition processes can also be used to engineer beneficial defects.

Migration of device contact metals and their related compounds during subsequent device processing steps or operation in high temperature environments is a source of contamination in electronic devices. In miniature microelectronic devices, the influence of ultra-low contamination from formation of silicides and carbides on metal-4H-SiC structures and interfaces becomes highly critical to device fabrication yield and determines their lifetime (de Luca *et al.*, 2014). Laplace-DLTS is highly sensitive for defect detection at low concentrations (Peaker *et al.*, 2012). Its capability in tracking diffusion of impurities at very low concentrations still needs to be established. The technique presents a low-cost alternative to expensive spectroscopies like RBS (Rutherford backscattering spectrometry) or ToF SIMS (time of flight secondary ion mass spectroscopy) which have high equipment budgets for the same purpose. ToF SIMS is destructive, which is sometimes detrimental to what is being measured.

Raman spectroscopy can also be used to characterize defects in SiC. The position, relative intensity and width of Raman spectra can be related to defects in the crystal

structure (Ward *et al.*, 2004). The technique continues to evolve and confocal Raman mapping can now produce depth profiles of outstanding resolution along cross sections. Its effectiveness in mapping defects introduced by incident radiation in SiC needs to be established.

1.2 Objectives

This work set out to investigate the defects induced in 4*H*-SiC by some standard industrial procedures that are employed in device manufacturing and processing. Whilst the generally accepted viewpoint is that defects in 4*H*-SiC are detrimental to device performance, the approach was to determine whether these defects can be engineered for beneficial purposes. The defect of interest was the V_{Si} which has been successfully used to produce a single photon source after transforming to $C_{Si}V_C$ through annealing. Our objectives were:

- To produce high quality Schottky barrier diodes (SBDs) and use their physical attributes to probe electrically active defects in the bandgap of 4*H*-SiC.
- Characterization of defects introduced by the sputter deposition process in 4*H*-SiC and to explore the possibility of adopting the process for the defect engineering of V_{Si}.
- Characterization of defects introduced during the annealing of SBDs and to track their migration in the lattice structure using Laplace DLTS.
- To apply 2D confocal Raman mapping in the characterization of defects introduced by swift heavy-ion irradiation of 4*H*-SiC and 4*H*-SiC devices.

1.2.1 Layout of the dissertation

- **Chapter 2** covers the theoretical aspects of defects in semiconductors and 4*H*-SiC in particular.
- **Chapter 3** discusses electrical measurements that are used to probe the defect characteristics in semiconductors. These formed the basis of all investigations in this thesis.

- **Chapter 4** explains the experimental techniques that were applied during fabrication and characterization of devices. The instrumentation used is also described in detail.
- **Chapter 5** is a presentation and discussion of results obtained.
- **Chapter 6** concludes the study and describes the future work arising.

1.3 4*H*-SiC as a semiconductor

4*H*-SiC has a wurtzite structure comprising of Si atoms, each covalently bonded to four neighboring C atoms; by sharing electrons in sp^3 hybrid orbitals to form a tetrahedron (Saddow and Agarwal, 2004). The direction normal to the Si – C bi-layers is known as the *c*-axis. Bi-layers arrange in a stacking sequence with three possible site configurations conventionally denoted by A,B and C. As illustrated in Figure 1.1 there is an ABCBABCB.....stacking sequence in 4*H*-SiC along the *c*-axis with a periodicity of 4. The lattice parameter is 10.0820 Å but it can vary depending on temperature and doping density. In the nomenclature 4*H*-SiC, the number 4 refers to periodicity (i.e number of bi-layers in one repeating unit), and *H* denotes the hexagonal structure.

The strength of the Si – C chemical bonding gives it robustness (high Young's modulus), inertness and high electrical conductivity. It also bestows on the material, extreme thermodynamic properties, meaning that growth can only be accomplished at high temperatures (Fraga *et al.*, 2015). Bulk growth of the material can be achieved through sublimation, solution, high temperature chemical vapor deposition and physical vapor transport. Epitaxial growth can be done on bulk substrates using chemical vapor deposition, molecular beam epitaxy and liquid phase epitaxy. Attaining perfect polytype control is always a challenge during growth processes, because other polytypes tend to appear. There is also difficulty in controlling defect densities. Extended defects like micropipes, dislocations and faults are almost always present.

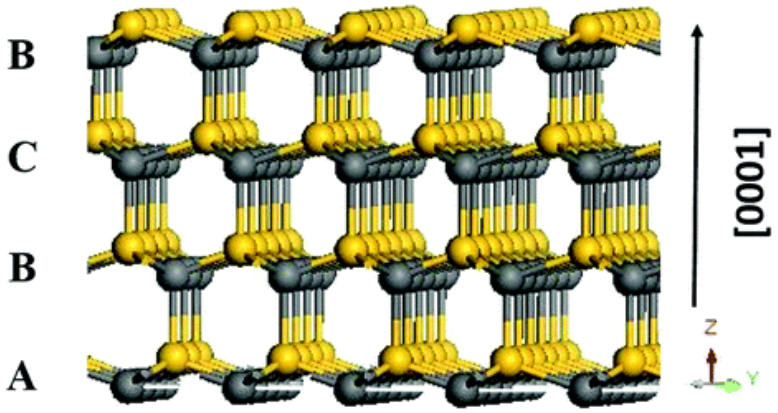

Figure 1.1: Schematic representation of the crystal structure of 4H-SiC. The grey entities represent silicon and the gold entities represent carbon.

CVD is the most widely used and successful technique for 4H-SiC homo-epitaxy. The growth is usually executed in two steps starting with in-situ etching of the substrate (usually bulk material) in a chamber to remove subsurface damage and to even the surface (Sukkaew *et al.*, 2018). Thereafter, the substrate is exposed to chemical precursors which can be monosilane and propane or ethylene. This is done in the presence of an argon or hydrogen carrier gas at around 1600 °C. A SiC layer is then formed on the substrate via nucleation. N-type doping is achieved by introducing nitrogen or phosphorous during growth. P-type doping is achieved by introducing beryllium, boron, aluminum or gallium. In a *hot-wall* CVD reactor, the SiC substrate is constantly heated during deposition for a uniform deposition that is not susceptible to warping.

The 4H polytype was chosen as the subject of this thesis because it is the one in which the single photon sources were reported (Lohrmann *et al.*, 2016).

1.3.1 Properties and applications

The table below lists some of the physical properties of 4*H*-SiC.

Table 1.1: Physical properties of 4*H*-SiC (Kimoto and Cooper, 2014)

Bandgap (eV)	3.2 – 3.3
Electric field breakdown (MV/cm)	2.0 – 3.0
Hole mobility (cm^2/ Vs)	115 – 200
Thermal conductivity (W/cm^2)	3 – 5

SiC is an indirect semiconductor with a wide bandgap leading to an inherent large carrier lifetime (Shul, 2001). In addition, the wide bandgap implies that higher thermal energy is required for intrinsic conductivity allowing the material to be used for high temperature applications of up to 300 °C without breakdown (Lamichhane *et al.*, 2014). The high electric field breakdown strength, allows high voltage applications and enables devices to withstand an electric field breakdown up to 10 times, when compared to an elemental semiconductor like silicon (Jayant, 2006). As a result silicon-carbide devices are smaller and more compact relative to those made from other semiconductors.

Thermal conductivity can be a measure of the ability of a material to dissipate heat. It's high value implies less cooling is necessary and so the devices can withstand much larger power densities and harsher environments (Feng, 2017). Furthermore, the material has a native oxide layer which makes it possible to fabricate the whole family of MOS based electronic devices. It can easily be doped as n-type or p-type in a wide range of more than 5 orders of magnitude.

Several electronic devices have been implemented on 4*H*-SiC to date. SBDs have been incorporated in a variety of power systems together with JFETs and MOSFETs which act as power switching devices. These have revolutionized the power electronics industry where performance of semiconductor devices is critical for efficiency. The weight of a power supply or inverter which was traditionally silicon based can be reduced by a factor of 4-10 when silicon carbide is incorporated. The drift layer of a SiC transistor is a tenth of the thickness in transistors reducing resistance and minimizing power loss.

- Insulated gate bipolar transistor (IGBT) modules which are made up of SiC Schottky diodes and MOSFETS are used in wind turbines enabling good temperature and load cycle stability at high power density (Rahimo *et al.*, 2015).
- SiC solar inverters convert D.C. supplied by solar panels to A.C. to adapt it to power levels of the grid and feed it to the grid (Wilhelm *et al.*, 2010).
- In energy storage, active front end converters made of SiC are used for charging and discharging batteries in an energy storage network tripling battery switching frequency and reducing filter costs (Madhusoodhanan *et al.*, 2013).
- In utility vehicles like forklifts or municipal garbage collection vehicles SiC main drive controllers supply high voltages at high power ranges (Saddow and Agarwal, 2004).
- SiC SBDs have a negligible reverse recovery time, therefore switching loss is dramatically reduced, and switching frequency is increased leading to down sizing of power components. In power factor correction circuits that are used in AC-DC power converters they have contributed to significantly smaller devices (Jovanovic and Jang, 2005).
- Portable electric car-chargers have been made 10 times smaller by the use of SiC MOSFETs. This has made electric cars more reliable (Vorel and Červinka, 2014).

All these devices are commercially available.

Chapter 2

Defects in semiconductors

2.1 Introduction

Defects are always present in crystalline solids. They have been shown to significantly affect the performance of silicon carbide based devices. This chapter examines defects found in semiconductors. Several ways in which they can be classified depending on the material in which they exist are listed. Only n-type 4H-SiC is discussed in this thesis. Detailed descriptions of the most prominent defects found in n-4H-SiC are given as well as some background theory on the diffusion process. In this work only zero dimensional defects were investigated, and they will be referred to as point defects. Point defects form the medium for diffusion in semiconductors.

2.2 Point defects

Examples of point defects (Figure 2.1) are:

- Vacancies: arise when a component is missing from a regular lattice point. In ionic compounds vacancies can pair up on cation and anion sub-lattices to form Schottky defects (Feng, 2017).
- Interstitials: formed when host atoms are located at an interstitial point instead of a regular lattice position. In ionic compounds when an ion occupies an interstitial position other than its own lattice site, a Frenkel defect is formed (Jimenez and Tomm, 2016).

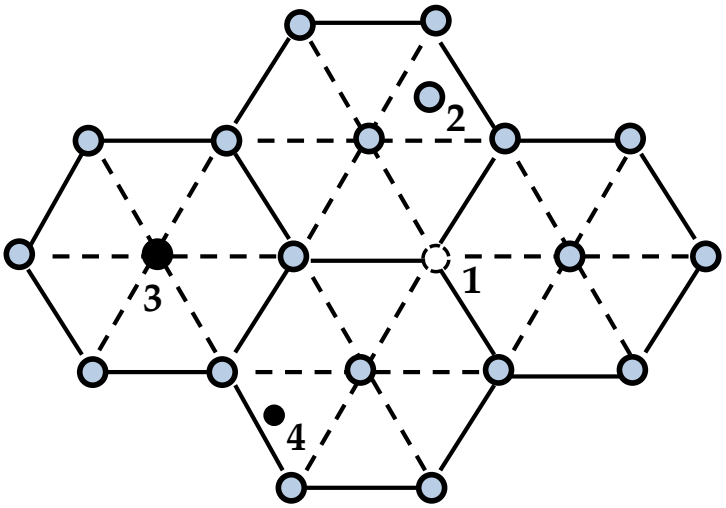

Figure 2.1: An illustration of (1) a vacancy, (2) a self interstitial, (3) a substitutional impurity (4) an interstitial impurity shown for the basal plane of a model hexagonal close packed lattice.

- Impurities: these are foreign atoms found isolated inside the lattice (Enderlein and Horing, 1997).
- Antisites: formed when certain concentrations of components exchange positions in sub-lattices (Queisser *et al.*, 2003).

Thermodynamically, defects can be classified based on the Gibbs potential (ΔG) (Paul and Divinski, 2017)

$$\Delta G = \Delta H - T\Delta S \tag{2.1}$$

where ΔH is the change in enthalpy, ΔS is entropy and T is temperature.

i) Equilibrium defects

They decrease the free energy causing the material to be more thermodynamically stable. This is because their production results in an increase in configurational enthalpy. They usually arise in the lattice during material growth (Smith and Wagner, 1987).

ii) Non-equilibrium defects

They increase the free energy causing the material to be more unstable. The increase in enthalpy dominates the increase in entropy. In the presence of sufficient thermal energy the system will try to minimize these defects. Examples are irradiation induced or damage induced defects (Ryoken *et al.*, 2005).

2.2.1 Shallow and deep level defects

Defects can be classified as shallow or deep levels. Shallow levels arise due to small perturbations of the lattice potential by an electrostatic potential generally created by a substitutional doping atom, able to bind an electron (if created by a donor atom) or a hole (if created by an acceptor atom), the same way an electron is bound by an H^+ ion, i.e. the trapped carrier sees a long-range $1/r$ potential.The properties of a shallow level can be approximated by the Bohr model of the hydrogen atom (Poole and Charles, 2004). They can be intentionally introduced in a semiconductor to control the Fermi level in a semiconductor.

Deep levels are defects with properties deviating from those predicted by the Bohr model of the hydrogen atom. The perturbations to the lattice potential are much larger in the trap's vicinity. They have a steep potential and their electron wave functions are localized at the defect site.

2.2.2 Capture and emission

The occupancy of deep levels is changed through carrier transitions between bands Schroder (2006) as shown in Figure 2.2. The possible transitions are

i) Carrier regeneration

ii) Electron trapping

iii) Hole trapping

iv) Recombination

On Figure 2.2 a recombination event occurs in the order (1) then (3). A regeneration happens if (4) occurs after (2). If (1) is followed by (2) or (3) is followed by (4) then the event is classified as trapping.

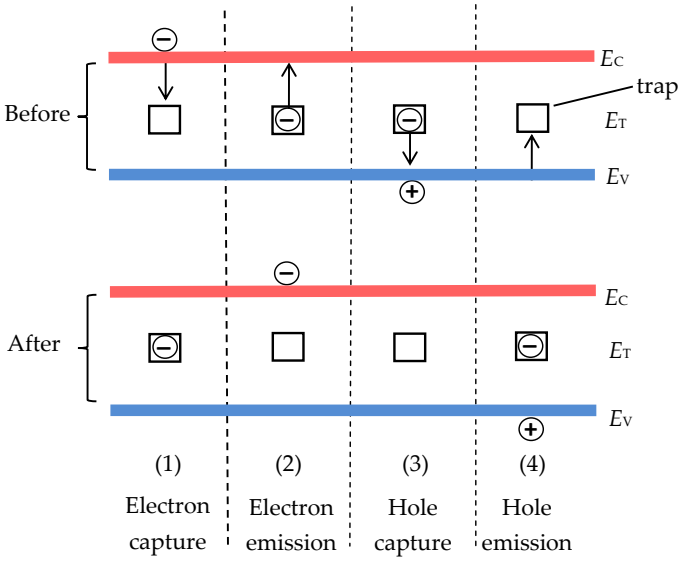

Figure 2.2: Possible interactions between a defect level and the energy bands, E_T is the effective energy of the trap, E_V is the valence band and E_C is the conduction band.

Figure 2.3 shows interactions that the point defects undergo with the conduction (E_C) and valence bands (E_V) (Bourgoin, 2012).

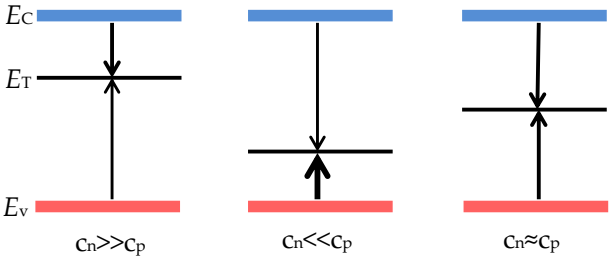

Figure 2.3: Capture and emission characteristics of traps and recombination centers.

- If $c_n >> c_p$ where c_n is the rate of electron capture and c_p is the rate of hole capture then the defect is termed an electron trap.
- If $c_n << c_p$ then the defect is termed a hole trap. If a hole trap becomes more negatively charged when it emits a hole it is referred to as an acceptor.
- It is called a midgap level or a recombination center when both c_n and c_p are similar.

The electron capture rate c_n and the capture cross section are related by

$$c_n = \sigma_n \langle v_{th} \rangle n \tag{2.2}$$

and similarly the hole capture rate is related to the capture cross section by

$$c_p = \sigma_p \langle v_{th} \rangle p \tag{2.3}$$

where p and n are the hole and electron trap concentrations, σ_p and σ_n are the capture cross sections and $\langle v_{th} \rangle$ gives the average thermal velocity of free electrons.

$$\langle v_{th} \rangle = \sqrt{\frac{3kT}{m_e^*}} \tag{2.4}$$

where m_e^* is the effective mass of the electron. A similar equation holds for holes. Using the principle of detailed balance, the emission rates of electrons to the conduction band is given by (Auret and Deenapanray, 2004)

$$e_n(T) = \frac{g_0}{g_1} \sigma_{ap} \langle v_{th} \rangle N_c \exp\left(-\frac{E_C - E_T}{kT}\right) \tag{2.5}$$

$E_C - E_T$ is the energy separation of the deep state from the conduction band, g_0/g_1 is the degeneracy between filled and empty levels and N_C is the effective density of states in the conduction band given by (Blood and Orton, 1978)

$$N_C = 2M_C \left(\frac{2\pi m_e^* kT}{h^2}\right)^{\frac{3}{2}} \tag{2.6}$$

M_c is the number of equivalent band minima. An Arrhenius plot of log (e_n/T^2) versus $1/T$ produces a straight line whose slope gives $E_C - E_T$ whilst extrapolation to the $1/T$ axis gives the apparent capture cross section.

2.3 The $Z_{1/2}$ defects in n-4*H*-SiC

The prominent defect levels observed in as-grown $4H$-SiC in the temperature range (20 – 380 K) we studied are known as the $Z_{1/2}$ centers observable in conventional DLTS scans at an energy of approximately 0.56 – 0.71 eV below the conduction band minimum. These defects limit the carrier lifetime in high purity epitaxial layers (Son *et al.*, 2012). Several different viewpoints exist in literature pertaining to their

identity. Eberlein *et al.* (2003) carried out theoretical calculations and they showed that the $Z_{1/2}$ was thermally stable and bistable. They modeled the defect as a pi-bonded di-carbon interstitial complex next to a nitrogen atom. Contrary to this, Trinh *et al.* (2013) theoretically linked the defects to a carbon vacancy.

The $Z_{1/2}$ has been shown by Son *et al.* (2012) to be related to a carbon vacancy and made up of two negative U centres with inverted ordering. Negative U behaviour is when one defect traps two electrons simultaneously with the second one being more strongly bound than the first (Thang, 2015). The $Z_{1/2}$ is, therefore, made up of two negative U centers namely the Z_1 with a donor level at approximately $E_c - 0.43$ eV and an acceptor level at approximately $E_c - 0.67$ eV, whereas for the Z_2 defect the donor level is at approximately $E_c - 0.46$ eV and the acceptor level is at $E_c - 0.71$ eV (Eberlein *et al.*, 2003). Hemmingsson *et al.* (1998a) had earlier given evidence of inverted ordering.

Doyle *et al.* (1998) showed that in VPE grown material, the Z_1 center originated from a defect of an intrinsic nature. Using secondary ion mass spectroscopy (SIMS) they proved that the defect was not linked to transition metals. Further, Zhang *et al.* (2003) showed that the concentration of intrinsic defects in the semiconductor was a factor of growth temperature. Pintilie *et al.* (2002) investigated the formation of the Z_1 defect by varying nitrogen dopant concentrations and C/Si ratios during CVD. The formation of the defect was also observed to be altered by the C/Si ratio. They, therefore, correlated it to the incorporation of nitrogen doping and suggested that it was a nitrogen complex with carbon interstitials or silicon vacancies.

Asghar *et al.* (2007) used DLTS to characterize defects in hot layer CVD grown epi-layers and they observed the Z_1 at $E_c - 0.61$ eV and an additional overlapping level introduced by the radiation which they attributed to the Z_2 overlapping with the pre-existing Z_1 peak. They reported that alpha particle irradiation transforms the Z_1 into the $Z_{1/2}$ and they related the Z_2 to the silicon vacancy.

The temperature range that was studied does not include the $EH_{6/7}$ but it is also an important defect in 4*H*-SiC.

2.4 Irradiation induced defects in 4*H*-SiC

The non-ionizing energy loss (NIEL) hypothesis has been successful in estimating energy displacements that account for damage in lattice structures. Conventionally

NIEL can be calculated as (Gao *et al.*, 2017)

$$\text{NIEL} = \alpha \int_{E_d}^{T_{max}} T \frac{d\sigma}{dT} G(T)\, dT \tag{2.7}$$

where α is the atomic density of the target material, T is the kinetic energy of the recoil material, T_{max} the maximum energy that can be transferred to a recoil nucleus by an incident particle, E_d is the threshold displacement energy, $d\sigma/dT$ is the differential interaction cross section, and $G(T)$ the Lindhard energy partition function (Lindhard *et al.*, 1963).

4H-SiC has been shown to be stable under harsh radiation environments (Nappi and Seguinot, 2004). Its threshold displacement energy is remarkably high, being 35 eV in Si and 20 eV in C (Jiang *et al.*, 2016). These values are almost triple those of gallium arsenide which is also considered a radiation hard material (Claeys and Simoen, 2002). Threshold energy refers to the minimum energy a lattice atom receives before being displaced to an interstitial position in an ion-solid interaction at cryogenic temperatures (Crawford and Slifkin, 2013). In order to apply silicon carbide to radiation hard devices, an in-depth knowledge of its response in such environments is required for refined control purposes.

Several studies have been carried out to create harsh radiation conditions from heavy ions on 4H-SiC under controlled environments, and probe the ensuing material perturbations. In an electrical study, Kalinina *et al.* (2002) irradiated 4H-SiC with 245 MeV Kr ions, and showed that it increased the concentration of Z_1 levels. Thereafter Kalinina *et al.* (2015) also irradiated 4H-SiC UV detectors with 167 MeV Xe ions and showed that the service life and radiation endurance of the devices increased at higher temperatures (23 – 180 °C).

Storasta *et al.* (2004) irradiated 4H-SiC epi-layers with low energy electrons (80 – 250 keV) and observed a linear increase in defect concentration with increasing radiation dose. They, therefore, speculated that no vacancies or di-vacancies were induced by the radiation. (Hemmingsson *et al.*, 1997) studied electron irradiated epitaxial layers and showed that the capture cross section of the induced defects is temperature dependent. Doyle *et al.* (1998) showed that the $E_c - 0.32$ eV, $E_c - 0.62$ eV and $E_c - 0.68$ eV levels introduced by electron irradiation annealed out at room temperature in VPE grown material.

Paradzah *et al.* (2015) irradiated Ni/4H-SiC Schottky diodes with 5.4 MeV alpha particles and revealed that the alpha particle irradiated devices had degraded diode characteristics. Omotoso *et al.* (2015) irradiated 4H-SiC Schottky diodes with high

energy electrons and showed that it induced the $E_c - 0.22$ eV,$E_c - 0.40$ eV and $E_c - 0.71$ eV levels. They also showed that after irradiation, the Richardson constant significantly increased, implying that it exacerbates inhomogeneity of the Schottky barrier.

Castelletto *et al.* (2014) realized an ultra-bright, photo-stable single photon source in 4*H*-SiC through optimized electron irradiation and annealing. They attributed the source to the carbon-antisite vacancy pair created by electron irradiation

2.5 Defects induced by metalization processes in n-4*H*-SiC

Metallization is a crucial processing step in the semiconductor device manufacturing industry. Deposition of metals on semiconductors is accomplished by evaporation or sputtering. Magnetron sputter deposition is arguably the most versatile technique for thin metal films. The technique is highly efficient because it can rapidly deposit metals with high melting points resulting in uniform films with good adhesion properties. It can be optimized to produce metal films with desired stoichiometric composition for particular purposes (Yeom *et al.*, 2017). In some cases, the technique has been used to enhance semiconductor properties (Kim *et al.*, 2017). Several types of nanostructures and films have been established on silicon carbide through sputtering (Gou *et al.*, 1999; Zhu *et al.*, 2013).

Due to the involvement of an incident plasma and metal particles, sputter deposition has been shown to introduce atomic scale surface damage which causes lattice distortions (Volpi *et al.*, 2004). These impact the rectification properties of devices and in some cases introduce defects in the bandgap. In n-type gallium arsenide it has been shown that devices fabricated by sputter deposition have lower barrier heights which have been ascribed to introduction of donor like defects in the semiconductor during sputter deposition (Auret *et al.*, 1997).

Electron beam deposition (EBD) is also another metalization technique which has been shown to introduce defects in n-4*H*-SiC. Omotoso *et al.* (2016) showed that the electron beam deposition of tungsten Schottky contacts introduced the $E_c - 0.42$ eV, $E_c - 0.70$ eV defects which had the same electronic properties as high energy electron irradiation (HEEI) induced defects. In an effort to understand the fundamental physics of defect formation during EBD a technique called electron beam exposure was designed by Coelho *et al.* (2013). They came to the conclusion

that defect formation was accounted for by intrinsic non-localized excitations, which modify defects deeper in the surface rendering them observable. According to them energy which formed was transferred through phonon activity (Archilla *et al.*, 2015).

2.6 Point defects and diffusion

In semiconductors diffusion is solely point defect based. The process is represented by Fick's first law which shows that the diffusing flux (J) in the x direction is directly proportional to a concentration gradient (Mehrer, 2007).

$$J_i = -D_i \frac{\partial C_i}{\partial x} \tag{2.8}$$

where D_i is the diffusion coefficient, C is the number of atoms of type i per unit volume. The negative sign makes a positive flux down the concentration gradient. For non-steady-state diffusion Fick's first law can be modified by the continuity equation to give Fick's second law (Paul *et al.*, 2014)

$$\frac{\partial C_i}{\partial t} = D_i \frac{\partial^2 C_i}{\partial^2 x} \tag{2.9}$$

The driving force of diffusion can be a potential gradient, thermal gradient, stress gradient or thermal vibrations. In the case of thermal vibrations components diffuse by overcoming an energy barrier. The required kinetic energy comes from thermal energy of atomic vibrations ($E \sim k_B T$). In the absence of a driving force random diffusion occurs driven by maximization of the system's entropy.

The following are brief descriptions of the diffusion mechanisms that occur through point defects.

2.6.1 Vacancy diffusion

This involves an impurity or lattice atom jumping from a lattice site to a vacancy (Laskar *et al.*, 2012). An empty lattice site exchanges positions with a neighboring occupied site. The probability for any atom in a solid to move is a factor of the probability of finding a vacancy in an adjacent lattice site. The number of vacancies

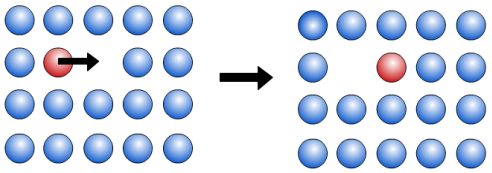

Figure 2.4: Vacancy diffusion.

per unit volume is given by

$$N_V = N\exp\left(-\frac{E_V}{k_B T}\right) \tag{2.10}$$

w here N is the total number of atomic sites, E_v is the energy required to move the atoms from a lattice site within the solid crystal to the vacancy, k_B is the Boltzmann constant and T is the absolute temperature. The number of vacancies present at anytime is therefore directly influenced by the temperature.

2.6.2 Interstitial diffusion

Interstitial diffusion involves smaller atoms moving through the crystal structure in between lattice atoms. The path is constrained by the crystal structure. The energy barrier to overcome is low due to the smaller atom and a large number of vacant sites to diffuse to. This is the mechanism when an impurity is added to a lattice structure. It essentially moves from one interstitial position to another interstitial position. An example is silicon self diffusion (Südkamp and Bracht, 2016) .

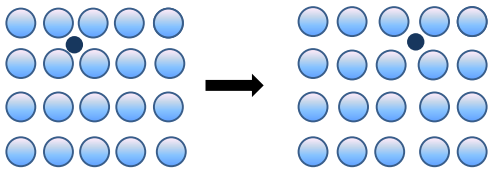

Figure 2.5: Interstitial diffusion before and after a jump.

2.6.3 Kick-out mechanism

In the kickout mechanism, a semiconductor atom is pushed from a crystalline lattice by an impurity atom simultaneously replacing it in the process by assuming the

former's position (Tilley, 2008). The atom is moved to an adjacent site. In this mechanism, the impurity atom may have come through the lattice via direct interstitial mechanism prior to replacing a semiconductor atom. Bracht *et al.* (2000) gave experimental and theoretical evidence of this mechanism in 4*H*-SiC.

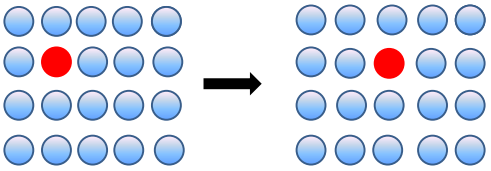

Figure 2.6: The kickout mechanism.

2.6.4 The Kirkendall effect

When two solids A and B of different elemental composition are brought into semi-finite contact and annealed to allow diffusion between them, they are called a diffusion couple. In such a situation, inter-diffusion of each species occurs towards each other. The intrinsic diffusion of the materials will not be at the same rate which results in a net drift in the direction of the one with a lesser diffusivity. There is a motion of the interface so that the lattice remains stationary, this is known as the Kirkendall effect (Sequeira and Amaral, 2014). The diagram below shows an illustration. Equation 2.8 can be adopted to diffusion of vacancies at the couple with solids A and B (Darken, 1948)

$$J_A = -D\frac{\partial C_A}{\partial x} \tag{2.11}$$

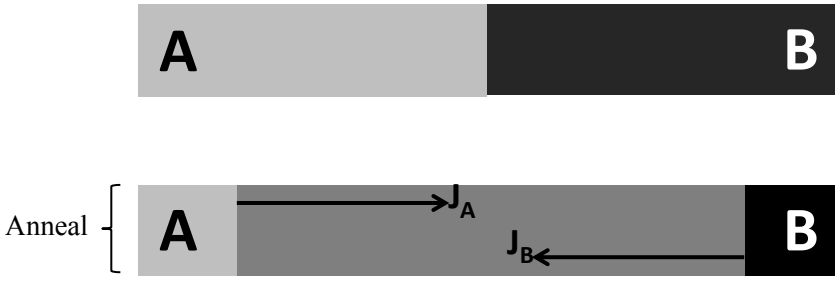

Figure 2.7: An illustration of the Kirkendall effect where J_A and J_B represent the flux of solids A and B.

where $D = N_A D_B + N_B D_A$, N_A is the atomic fraction of A and N_B is atomic fraction of B and D_A and D_B are the diffusivity of A and B respectively.

2.7 Defect annealing

The prominent annealing mechanisms of vacancies and interstitials are

i out-diffusion to the surface.

ii diffusion to extended defects.

iii recombination of vacancies with interstitials (Choyke *et al.*, 2003).

Annealing is used in the semiconductor industry for activating dopants, correcting positions of implanted ions, re-establishing a crystal structure after amorphization due to radiation damage and sometimes to eliminate excess defects introduced during processing (Perevostchikov and Skoupov, 2005). The annealing process i.e. time dependent change of the defect concentration, N_t occurs according to

$$\frac{dN_t}{dt} = -\alpha K N \tag{2.12}$$

The prefactor K is a reaction velocity constant and α represents the order of reaction $\alpha = 1$ single defect reaction (migration or dissociation of defects), $\alpha = 2$ two defects of the same concentration recombine. The prefactor K can be written as

$$K = K_o \exp\left(\frac{\Delta E}{k_B T}\right) \tag{2.13}$$

with K_o the frequency factor related to the vibration frequency of the crystal and k_B is the Boltzmann constant. Equation 2.13 shows that the success of an annealing process is highly dependent on the annealing temperature. ΔE is the activation energy of the annealing process.

Storasta *et al.* (2008) developed a technique which involved annealing 4H-SiC after carbon implantation. They successfully eliminated the $Z_{1/2}$. Løvlie and Svensson (2011) showed that the required annealing temperature for silicon carbide can be significantly lowered in an oxidizing atmosphere. Also Park *et al.* (2016) managed to form p-type dopant in 4H-SiC by depositing an Al foil and annealing at 1000° C.

2.8 Raman spectroscopy on 4*H*-SiC

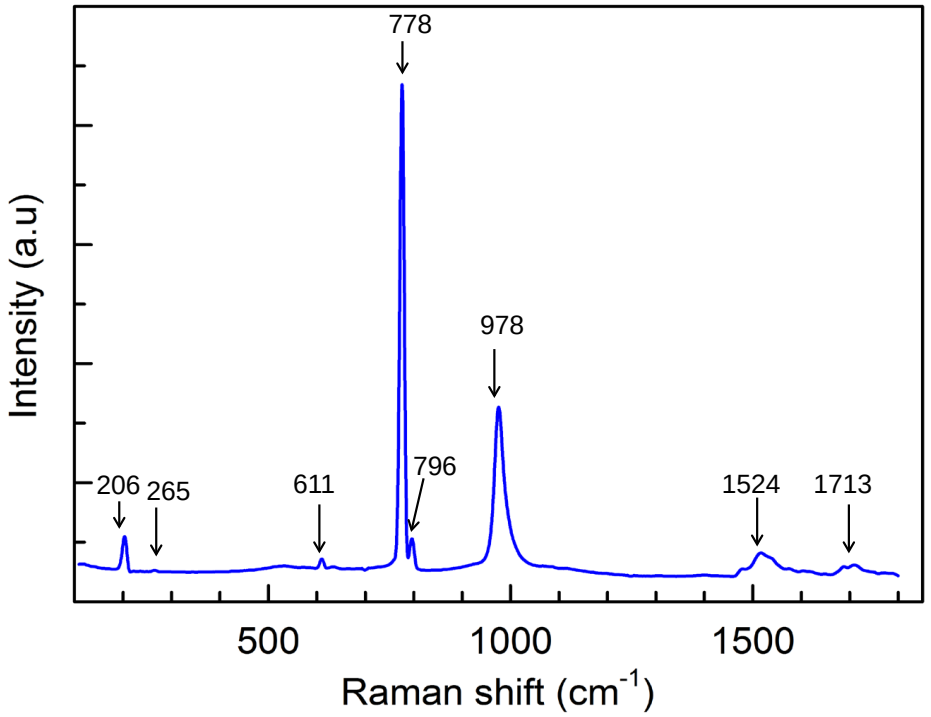

Figure 2.8: Raman spectrum of as grown n-4*H*-SiC at room temperature.

Raman spectroscopy can be used to characterize defects in 4*H*-SiC. The position and relative intensity and bandwidth of Raman spectra can be related to defects in the crystal structure (Ward *et al.*, 2004). Hundhausen *et al.* (2008) used the technique to probe the temperature dependence of defect occupation at 100 K and 200 K, based on thermal excitations of electrons to the conduction band which were observed from Raman intensities. Figure 2.8 shows the Raman spectrum of as grown 4*H*-SiC (1000) (8° off axis) measured using 532 nm wavelength light in the 100 - 1800 cm^{-1} range. The N doped wafers consisted of a 6.0 μm epitaxial layer of doping density 6.0×10^{16} cm^{-3} grown on a highly doped substrate of approximately 10^{18} cm^{-3}.

4*H*-SiC has a *c*-axis normal to the Si – C double atomic layers (Fan and Chu, 2014). Transverse phonon coupling modes are perpendicular to the *c*-axis and the axial or longitudinal phonon coupling modes are parallel to the *c*-axis (Burton *et al.*, 1998). The spectrum has peaks at 206 cm^{-1}, 265 cm^{-1} corresponding to transverse acoustic (TA) modes, and at 611 cm^{-1} peak which is a longitudinal acoustic (LA) mode (Sorieul *et al.*, 2006). The optical transverse (TO) and longitudinal (LO) peaks are observed at (778 cm^{-1}, 796 cm^{-1}), and 978 cm^{-1} respectively. The LO at 978

cm^{-1} is intrinsically present, but its position and shape is sensitive to free carrier concentration (N-doping) (Nakashima and Harima, 1997). In addition, a low intensity broad peak around 1524 cm^{-1} and 1713 cm^{-1} are also observed, corresponding to the optical branches. At around 500 cm^{-1} a pedestal is observed, which according to Burton *et al.* (1998) is a feature of Raman scattering not luminescence.

2.8.1 Confocal Raman microscopy

Confocal Raman microscopy refers to the ability to spatially filter the analysis volume of the sample, in the XY (lateral) and Z (depth) axes (Toporski *et al.*, 2018). Analysis can be done on layers of as thin as a μm in dimension (Giridhar *et al.*, 2017). Figure 2.9 shows a depth profile and associated spectra obtained from as-grown 4*H*-SiC specified in section 2.8.

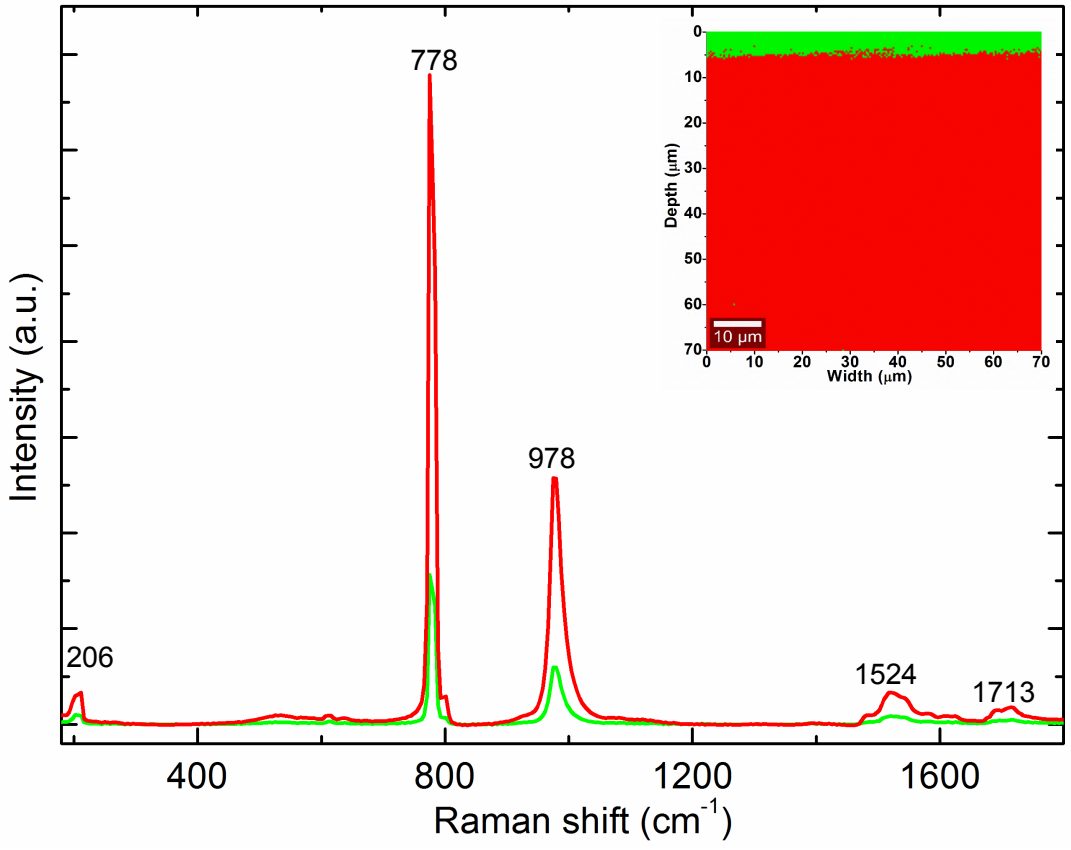

Figure 2.9: (inset)Depth profile of as grown 4*H*-SiC obtained from cluster distributions showing an epitaxial layer (green) and the bulk layer (red). The graphs show the cluster average raman spectra for the depth profile

On the profile, the top layer (green) is approximately 6μm thick. This is consistent with the thickness of the epitaxial layer as specified by the suppliers. The average cluster spectra shown in Figure 2.9 are therefore a representation of the wafer structure with the spectrum for the epitaxial layer in green and the one for the bulk material in red.

Chapter 3

Electrical measurements

3.1 Introduction

For successful electrical measurements, it is prerequisite that high quality contacts are fabricated to produce a metal-semiconductor device (Schottky diode). This will allow for formation of a depletion region so as to probe physical properties such as capacitance. From the capacitance information pertinent to defect properties such as their activation energy, capture cross section and doping concentration can be deduced. In this chapter the formation of a depletion region is explained during contact formation. In addition detailed explanations on current-voltage, capacitance-voltage and DLTS measurements are given.

3.2 Depletion region

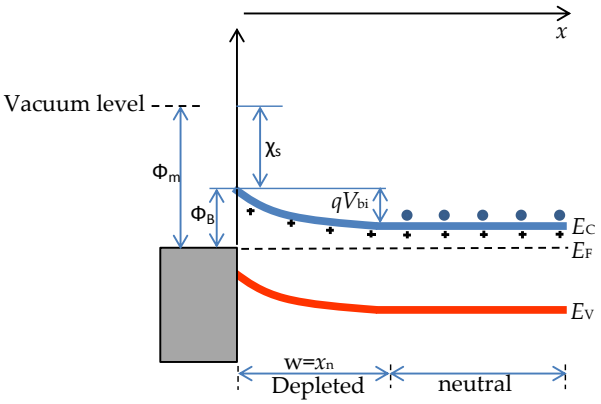

Figure 3.1: Energy band diagram showing a Schottky barrier formed at a metal-semiconductor interface (Grundmann, 2006).

Figure 3.1 shows the energy band diagram which results when a particular metal is deposited on an n-type semiconductor. For ideal contact formation, a metal and a semiconductor with different Fermi level positions relative to the vacuum level are brought into intimate contact. The Fermi levels align and become continuous as illustrated (Li, 2012). In-order to attain this continuity in the Fermi levels the bands bend with a characteristic barrier height (Φ_B).

$$\Phi_B = \Phi_m - \chi_s \tag{3.1}$$

The barrier height is defined as the difference between the metal work function (Φ_m) and the electron affinity of the semiconductor (χ_s) (Mishra and Singh, 2007). This is known as the Schottky-Mott rule.

Because of the thermodynamic contact between the metal and the semiconductor, electrons traverse the junction from the semiconductor into the lower energy states of the metal in-order to lower their energy. The band bending sets a barrier to current flow across the metal-semiconductor junction. Ionized donor atoms corresponding to the zone depleted of electrons remain in the semiconductor, with a positive charge equal in magnitude to that accumulating at the metal surface, forming a space charge region (depletion width).

The depletion width x_n is defined as the distance between the metal semiconductor interface and normal bulk behavior on the semiconductor side of the junction (Blood and Orton, 1992).

The semiconductor's conduction and valence bands (E_C and E_V) form a definite energy relationship with the metal's Fermi level at the interface (Mönch, 2013). This relationship serves as a boundary condition to the solution of Poisson‘s equation in the semiconductor. In the one dimensional case, the electric field in the depletion width is determined from Poisson's equation (Sze and Kwong, 2006)

$$\frac{d^2\Phi}{dx} = \frac{dE}{dx} = \frac{\rho(x)}{\epsilon_s} \tag{3.2}$$

where Φ is the electrostatic potential, $\rho(x)$ is the charge density and ϵ_s is the permittivity of the semiconductor. Using the depletion width approximation i.e. assuming that it is possible to divide the semiconductor into two regions namely:

1. The depletion region, directly below the metal, which is devoid of free carriers,

2. The bulk of the semiconductor, which is electrically neutral and of uniform doping density (N_D) (Neamen, 2012).

$$\rho(x) = \begin{cases} eN_D, & \text{if } x < x_n. \\ 0, & \text{if } x > x_n. \end{cases} \tag{3.3}$$

where $w = x_n$ (Figure 3.1) is the width of the depletion region. Integrating equation 3.2 twice with respect to x and applying the boundary conditions we obtain the electric field as

$$E = -\frac{eN_D}{\epsilon_s}(x_n - x) \tag{3.4}$$

Which is a linear function of the distance x. The depletion width may be calculated for a uniformly doped semiconductor as

$$w = x_n = \left[\frac{2\epsilon_s(V_{bi} + V_R)}{eN_D}\right]^{1/2} \tag{3.5}$$

at a reverse bias V_R (Neamen, 2012). V_{bi} is a built in potential barrier. It is the barrier seen by electrons in the conduction band trying to move into the metal from the semiconductor side. If the semiconductor is heavily doped, then the depletion width becomes very narrow and an ohmic contact is formed.

3.3 Capacitance-voltage measurements

Capacitance-voltage measurement were done following the Schottky-Mott theory. The junction capacitance per unit area is given by (Brillson, 2012)

$$\frac{C}{A} = \left[\frac{e\epsilon_s N_D}{2(V_{bi} + V_R)}\right]^{1/2} \tag{3.6}$$

For a SBD, the diode capacitance is measured as a function of an applied reverse bias. A small A.C. voltage is superimposed on a reverse biased diode, altering the depletion width (Sharma *et al.*, 2011). The differential capacitance is analyzed following the equation (Sze and Kwong, 2006)

$$C^{-2} = \left[\frac{A^2\epsilon_s eN_D}{2(V_{bi} + V_R - kT/q)}\right] \tag{3.7}$$

where, A is the diode cross sectional area, V_{bi} the diffusion potential at zero bias obtained from the extrapolation of linear C^2-V plots to the V axis ($V_0 = V_{bi} - kT$) (Figure 3.2). The gradient $2/A^2\epsilon_s q N_D$ can be used to deduce the donor concentration. The $C-V$ barrier height can be determined as

$$\phi_{CV} = \phi_n + eV_0 + kT \tag{3.8}$$

V_0 is the potential difference between the conduction band minima and the Fermi level in the neutral part of the semiconductor (Karatas and Altndal, 2005):

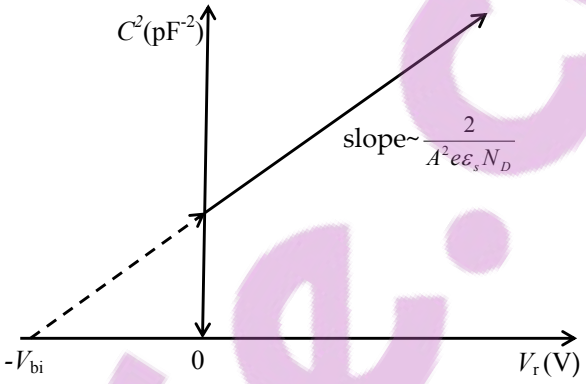

Figure 3.2: Schematic C-V dependence of a Schottky diode (Brillson, 2012).

3.4 Deep level transient spectroscopy (DLTS)

DLTS is a high frequency thermal scanning technique used for detection and identification of electrically active defect states. It is based on Equation 2.5 and is attributed to Lang (1974) who presented a way of displaying emission data spectroscopically as a function of temperature (Peaker *et al.*, 2012). As a result, the fundamental properties of traps in the bandgap of a semiconductor can be probed by perturbing their occupancy and their charge density then observing the relaxation. Defects will be detected at a temperature determined by their capture cross section and position in the energy gap. A voltage pulse is employed to fill and empty charge traps.

The depletion width (w) of a Schottky barrier diode extends with applied bias (V_A). The corresponding junction capacitance is a function of the junction area (A). This

implies that the magnitude of the bias during a pulse time t_p determines the magnitude of w (Benton, 1990). Hence we can monitor the concentration of holes or electrons trapped by deep levels using capacitance.

$$C = \frac{\epsilon A}{w} = A\sqrt{\frac{e\epsilon_s N_D}{2(V_{bi} + V_R)}} \tag{3.9}$$

A form of Equation 3.6.

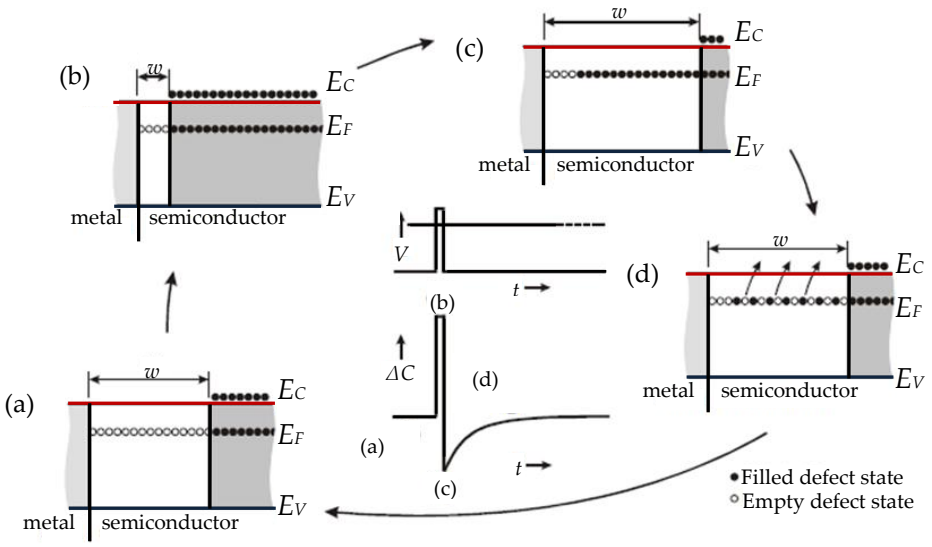

Figure 3.3: Variation in trap occupancy for a DLTS scan cycle a) reverse bias b) filling pulse c) directly after pulse removal, c) time t after pulse removal (Schroder, 2006).

In Figure 3.3(a), under a steady state with reverse bias V_R, traps in the depletion region below the Fermi level are assumed empty, extending the depletion region. When the filling pulse (V_P) is applied (Figure 3.3(b)) the depletion width is reduced, allowing free carriers to enter the depletion region corresponding to the applied bias, enabling the trapping to occur. V_R and V_P (Filling pulse) determine the section of the space charge region where the trapping deep levels are accessed (Simoen *et al.*, 2015). Upon entry the electrons are captured by empty traps at an exponential rate given by

$$N(t) = N_T[1 - \exp(-c_n t)] \tag{3.10}$$

where N_T is trap density (Auret and Deenapanray, 2004). c_n, the electron capture rate is defined in Equation 2.2 At the end of the pulse V_R returns to its steady state value. In Figure 3.3(c) electrons quickly acted upon by the junction electric field are

emitted. Finally in Figure 3.3(d) trap occupancy exponentially relaxes and there is thermal emission of the charges.

In a DLTS scan the sequence is repeated periodically. The capacitance transient's time constant is a function of the trap's emission rate. Probability of finding a deep level unoccupied at the beginning of the capacitance transient is determined by the pulse width.

The parameter space of DLTS is made up of the following

1 Filling pulse.

2 External reverse bias V_R.

3 Duration of the pulse width t_p.

4 Rate window frequency.

5 Sample temperature.

3.4.1 The rate window scan

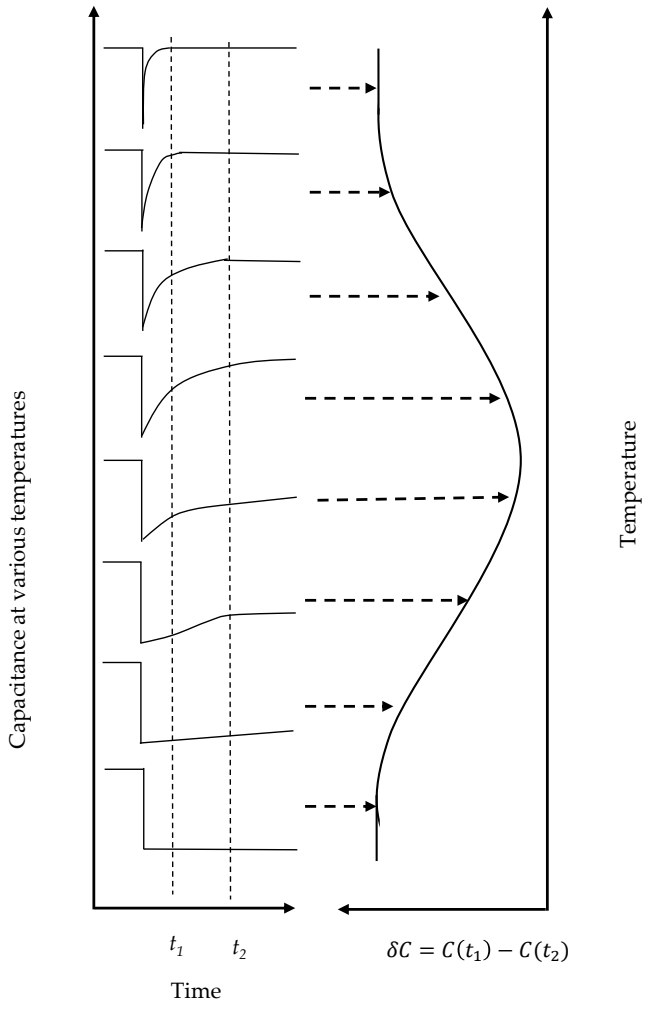

Figure 3.4: Left: change in the capacitance transient with increasing temperature Right: DLTS obtained from plotting δC (Schroder, 2006).

A trap exhibits a typical temperature at which a peak in the DLTS signal is observed. At lower temperatures, the emission rate will be slow and at higher temperatures the emission rate will be faster. As a result the nature of the time constant is expected to vary with increasing or decreasing temperature (Simoen *et al.*, 2015). In a rate window scan the capacitance is monitored over an observation time window, (t_1 - t_2). The difference in capacitance C(t_1) - C(t_2) gives a peak shaped curve as shown in Figure 3.4.

The peak maximum corresponds to an emission rate given by (Lang, 1974)

$$\tau_n = \frac{t_2 - t_1}{ln(\frac{t_1}{t_2})} \tag{3.11}$$

If the scan is repeated for several rate windows $(t_1 - t_2)$ pairs, Arrhenius analysis can be done according to Equation 2.5 from the slope of the linear fit(least squares) of a $\ln(e_n/T^2)$ versus (1/T) curve to get the activation energy from the slope and the capture cross section from the y-intercept.

3.5 Laplace transform DLTS

Conventional DLTS has poor time constant resolution and cannot decipher the fine structure of any closely spaced defects with almost similar emission rates. A quantitative improvement in DLTS resolution was introduced by Dobaczewski *et al.* (1994). This technique is based on the assumption that capacitance transients are characterized by a spectrum of emission rates. It makes use of Tikhonov's regularization to separate the constituent exponentials by imposing a constraint on the second derivative (Eiche *et al.*, 1992). Then using inverse Laplace transforms we obtain

$$f(t) = \int_0^\infty F(s)e^{-st}\,ds \tag{3.12}$$

where $F(s)$ is the spectral density function, an inverse function of $f(t)$ the recorded transient (Dobaczewski *et al.*, 1994). $F(s)$ is a delta function therefore a plot of $F(s)$ versus emission rate produces a spectral function which can be used as a defect signature. The area below each peak is directly proportional to the trap concentration and is a function of the emission rate. Up to 32000 transients can be captured at a fixed temperature and averaged. Fixing the temperature improves the time constant resolution. A good signal to noise ratio provides an order of magnitude better resolution than conventional DLTS (Dobaczewski *et al.*, 2004).

3.6 Defect depth profiling

According to Zohta and Watanabe (1982) defect concentration N_T for an applied DLTS pulse V can be described by

$$\frac{N_T(x_m - \lambda_m)}{N_D(x)} = \frac{1}{\left(1 - \frac{\lambda}{x}\right)^2 - \left(\frac{x_p - \lambda_p}{x}\right)^2} \cdot \frac{2\Delta C}{C} \tag{3.13}$$

where ΔC is the change in capacitance due to the pulse (at $t = 0$ just after pulsing), x is the width of the depletion layer ($x = z + \lambda$) and z is a distance measured from the surface into the semiconductor depletion width. The defect levels in the depletion width ($0 \leq z \leq x$) are empty in the layer $0 \leq z \leq x - \lambda$, and $x - \lambda$ is the plane where the deep levels cross the bulk Fermi level. The subscript p represents variations during the pulse and

$$x_m - \lambda_m = \frac{1}{2}[(x - \lambda) + (x_p - \lambda_p)] \tag{3.14}$$

The subscript m represents relaxation. This method gives an accurate defect concentration and eliminates limitations of other simpler methods in terms of accuracy. By fixing the reverse bias and varying the applied Laplace-DLTS pulse at a fixed temperature, a depth profile of the defect concentration versus depth below MS junction can be plotted.

3.7 Current-voltage measurements

The current-transport across a MS junction is due mainly to majority carriers. For a moderately doped semiconductor, the current transport can be adequately described by thermionic emission theory because it is the principal current transport mechanism. For pure thermionic emission, the relationship between the current I and the applied bias voltage V in the forward direction assuming that $V > 3kT/e$ is given by:

$$I = AA^*T^2 \exp\left(-\frac{e\Phi_0}{kT}\right)\left[\exp\left(\frac{e(V - IR_s}{nkT}\right) - 1\right] \tag{3.15}$$

where e is the electronic charge, k the Boltzmann constant, T the absolute temperature, R_s the series resistance obtained from ohm's law, $\phi_0 = \phi_{IV}$ the zero-bias barrier height, A the diode area and A*(=146 A cm^{-2}K^{-2}) is the Richardson's constant

(Roccaforte *et al.*, 2003). The pre-factor of the second exponential in Equation 3.15 gives the reverse saturation leakage current, I_S. The ideality factor n is given by

$$n = \frac{e}{kT}\left(\frac{dV}{d(\ln I)}\right) \tag{3.16}$$

where $0 \leq n \leq 1$ is a measure of the adherence to pure thermionic emission and it reflects barrier deformation under bias (Sze and Kwong, 2006). The zero bias barrier height, (Φ_0) is obtained from (I_S):

$$\Phi_0 = \frac{kT}{e}\ln\frac{AA^*T^2}{I_s} \tag{3.17}$$

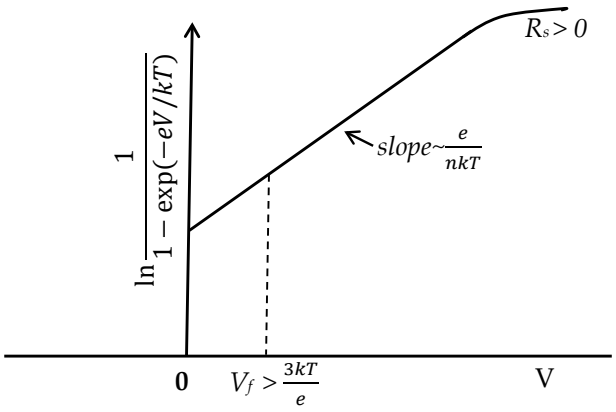

Figure 3.5: Schematic I-V characteristic of a Schottky barrier diode (Brillson, 2012).

Reverse leakage current refers to the maximum current that flows through the junction at a particular reverse bias (Crofton and Sriram, 1996). Its value is obtained as the intercept of the current axis when $V = 0$.

The conventional activation energy/Richardson plot of $\ln(I_s/T^2)$ vs $1000/T$ is obtained after linearizing Equation 3.17 yielding

$$\ln\left(\frac{I_s}{T^2}\right) = \ln(AA^*) - \frac{e\Phi_0}{kT} \tag{3.18}$$

Splitting of the Richardson plot into two linear regions has been observed after measuring $4H$-SiC devices and has been explained as due to two distinct conduction mechanisms, spatial in-homogeneous barrier heights and potential fluctuation at the

interface that consist of low and high barrier areas (Yue-Hu *et al.*, 2011; Huang and Wang, 2015).

Chapter 4

Experimental techniques

4.1 Introduction

In this chapter we briefly describe the apparatus and experimental techniques that were utilized. Nitrogen doped, n-type (0001) oriented $4H$-SiC (8 deg off axis) wafers supplied by Cree. Inc. were used. The wafers consisted of a 6.0μm epitaxial layer with a doping density 6×10^{16} cm^{-2} grown on a highly doped substrate of approximately 1.0×10^{18} cm^{-2}

4.2 Device fabrication

4.2.1 Cleaning procedure

Before fabrication of MS devices meticulous cleaning is required, as adsorbents can contribute to generation of undesirable interface states at the junction. Stringent guidelines have to be followed for consistency. Dedicated glassware and fluoroware tweezers are used for each cleaning stage. Firstly degreasing is done using organic solvents in-order to remove surface contaminants. The degreasing procedure was performed in four steps which involved boiling for 5 minutes each in

- trichloroethylene,
- acetone,
- and methanol.

- thereafter the samples were rinsed thrice in deionized water of resistivity $18\text{M}\Omega\text{cm}^{-1}$

The samples were then wet etched in-order to remove the native oxide layer by

- Submerging in 5 % hydrofluoric acid for half a minute. Finaly the samples where blow-dried using flowing nitrogen gas.

Transfer of samples after etching are quickly done to minimize regrowth of the native oxide layer.

4.2.2 Ohmic contacts

Immediately after etching, samples were rapidly transferred into the vacuum chamber of an Edwards 306 resistive coating unit, inorder to minimize the likelihood of re-growth of native oxide layer. The chamber pressure was pumped down to $\sim 1 \times 10^{-7}$ mbar. Nickel was deposited on the highly doped sides of the samples. Thereafter the contacts were annealed for 10 minutes at 950 °C in Ar to allow for formation of Ni silicides so as to lower the contact resistance (Kuchuk *et al.*, 2008).

4.2.3 Schottky contacts

A cleaning procedure similar to the one followed in Section 4.2.1 was followed. However, instead of boiling the samples were placed in an ultrasonic bath at room temperature during the degreasing. Once etched the samples were loaded into either a resistive deposition chamber or a sputter deposition chamber. (The concentration of HF and duration of the etch were experimentally tested and chosen so that they cannot be sufficient to remove the already deposited ohmic contacts) High purity metals were deposited through a metal mask with circular perforations, to make contacts of 0.6 mm radius. Figure 4.1 is an illustration of the cross sectional profile of a fabricated Schottky barrier diode with an ohmic contact and Schottky contacts. Nickel and tungsten were used as contact metals.

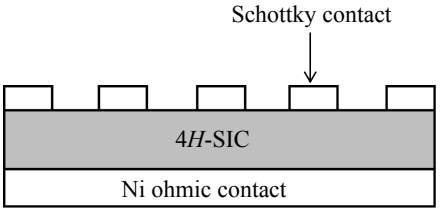

Figure 4.1: Schematic representation of the cross section of a SBD showing fabricated metal contacts.

4.2.4 Resistive evaporation (RE)

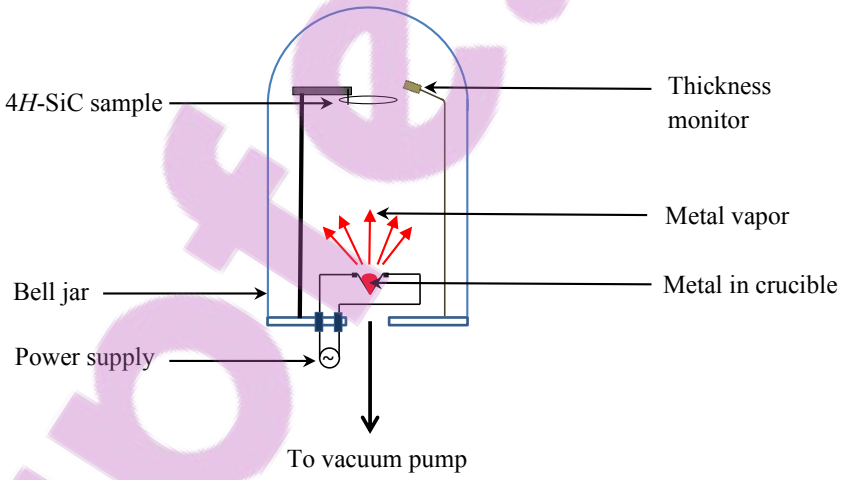

Figure 4.2: Schematic representation of resistive evaporation system.

Resistive evaporation systems are made up of a vacuum chamber, resistive wire shaped into a crucible, a substrate holder and a quartz thickness monitor. A large current is passed through the crucible heating it and melting the metal sufficiently to cause the metal to start evaporating under vacuum. The vapor travels from the crucible to the 4*H*-SiC substrate where it condenses and forms a thin film. A typical vacuum of approximately 1.0×10^{-7} mbar is required to evacuate gas molecules which can impede the motion of the metal vapor or contaminate them. The quartz crystal monitor records the thickness of the deposited material.

4.2.5 DC magnetron sputter deposition

A D.C. magnetron sputter system is made up of a vacuum chamber, magnetron cathodes, a target metal, a vertical center rod where the substrate sample is mounted (anode) and gas inlets. With the substrate mounted, the vacuum chamber is filled with Ar gas then a D.C. voltage is applied between the anode and the cathode. Magnetrons (magnets behind the target cathode/metal) generate a stable plasma with high ion density by confining electrons near the target surface. Ar^+ ions bombard the target material, ejecting atoms due to momentum transfer interactions. These particles traverse the vacuum deposition chamber and coalesce as a thin film on the surface of the substrate to be coated.

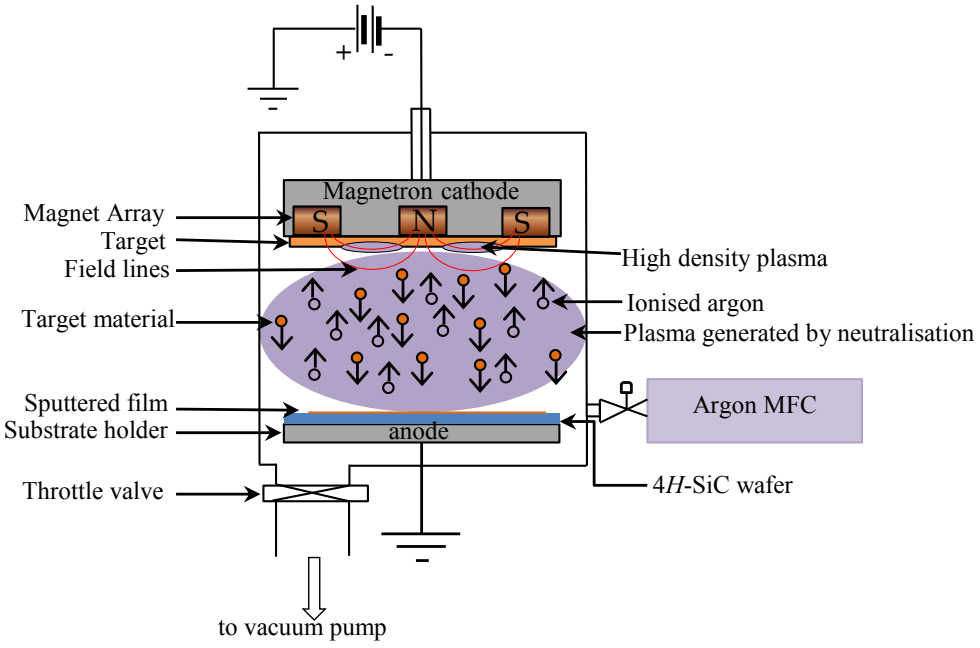

Figure 4.3: Schematic representation of sputter deposition system.

Our depositions were carried out under a D.C. power of 1000 W and an Ar pressure of 2×10^{-2} mbar. Target to sample distance was maintained at 7 cm

4.3 Swift heavy ion irradiation

Swift heavy ion irradiation was done at the Joint Institute for Nuclear Research in Dubna, Russia. Xe^{26+} ions were implanted at room temperature at an energy of 167

MeV with a fluence of 5×10^{11} cm^{-2} on samples cleaned following the procedure in Section 4.2.1. Since our interest was in studying the radiation damage a moderate flux was maintained in-order to avoid annealing out some of the damage due to an elevated sample temperature.

4.4 Annealing of samples

Isochronal annealing was done in a quartz tube placed in Lindberg heavy duty furnace at 100 °C steps. A thermocouple was placed close to the sample to monitor its temperature. The sample was placed on a silicon sample holder, which could be positioned in any part of the quartz tube, depending on the required annealing temperature. A steady flow of Ar gas was maintained by a mass flow controller. Annealing was typically done in the 100 °C – 1100 °C temperature range. The temperature was gradually ramped to a required setpoint to avoid subjecting the samples to a rapid thermal shock.

4.5 Characterization Techniques

4.5.1 *I-V* and *C-V* measurements

I-V and *C-V* measurements were carried out by a system consisting of a probe station, HP4140 pA meter/DC voltage source and a HP 4192A LF Impedance analyzer with a current limit of 1.0×10^{-14} A. The devices were placed on the probe station and all measurements were performed in the dark to avoid photo-generation of carriers. An in-house developed Labview^{TM} program controlled the data acquisition, through a graphical user interface. It can alternate between *C–V* and *I–V* measurement through a relay-switch box. The same program generates various plots and analyses them using pre-set material constants to calculate diode parameters according to Equations in Sections 3.3 and 3.7. For *C-V* characterization, an A.C. voltage with an oscillating frequency is superimposed on a D.C. bias in a desired range to obtain the capacitance. Using the interface, linear fits are then performed on $C^{\,2}$–V plots to derive the dopant concentration and Φ_{CV} amongst other parameters.

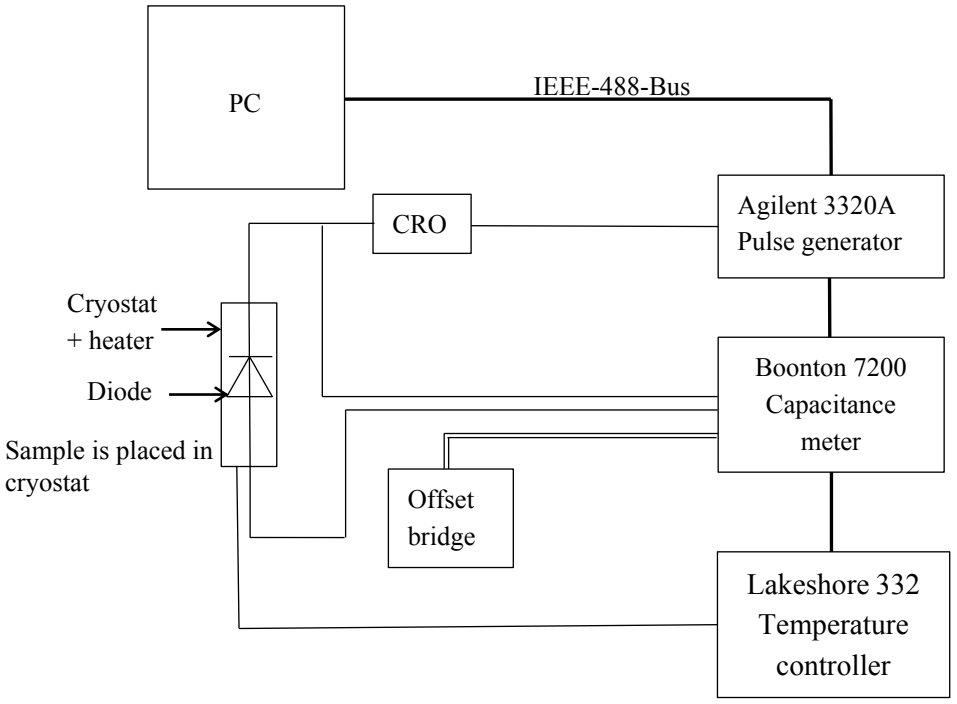

Figure 4.4: Schematic representation of DLTS and L-DLTS instrumentation.

4.5.2 DLTS measurements

The DLTS setup consists of

- A helium closed-cycle cryostat with an indium conducting stage on a sapphire platform where the sample is mounted. The stage has a built-in heater and a diode temperature sensor. The cryostat is capable of cooling to 15 K.
- A Lakeshore 340 temperature controller.
- Boonton 7200 capacitance meter with a 100 mV A.C. ripple voltage, at 1 MHz.
- A capacitance offset bridge.
- Agilent 3320A 15 MHz waveform signal generator for providing the required quiescent reverse bias and a filling pulse.
- A cathode ray oscilloscope (CRO).
- Computer with A2D card and Labview software to control the measurements and acquire data

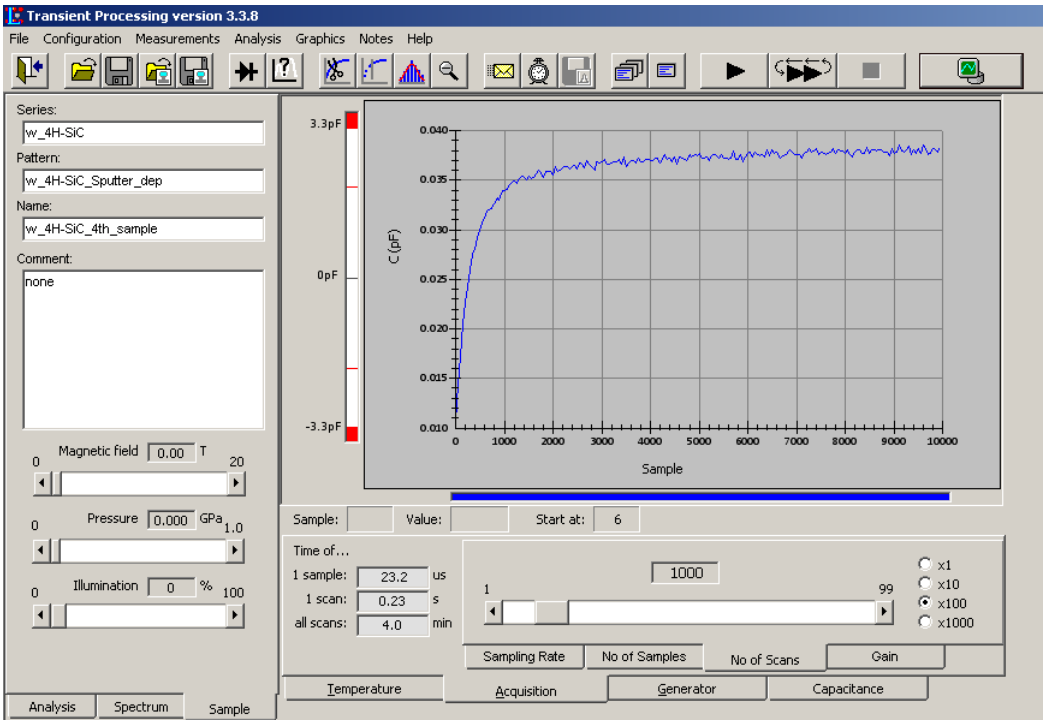

Figure 4.5: Screenshot of the front panel of Laplace transient processing software.

A block diagram for the DLTS measurement system is shown in Figure 4.4. The sample to be measured is mounted on the indium stage. Two beryllium-copper probes connect the ohmic and the Schottky contacts to the capacitance meter.

A transistor-transistor logic (TTL) pulse from the computer triggers the pulse generator which maintains a quiescent reverse bias and supplies a periodic filling pulse. As temperature is varied a DLTS spectrum is obtained. The capacitance transient is displayed on the screen of the PC during conventional DLTS scans.

The fine structure of all defects observed in conventional DLTS scans is then measured using Laplace-DLTS to get the signatures and defect concentrations. The L-DLTS software uses three mathematical routines for Tikhonov's regularization namely FITKREG, CONTIN and FLOG (Eiche *et al.*, 1992). These have to produce the same solutions for a result to be considered accurate. A screenshot of the Front panel for L-DLTS is shown in Figure 4.5

4.5.3 *X*-ray diffraction

X-ray diffraction(XRD) is a phenomenon that occurs when the atomic planes of a crystal scatter an incident *X*-ray beam causing it to interfere with another one as they leave the crystal lattice (Guinier, 2013). In-order for constructive interference

to occur, the Bragg condition

$$n\lambda = 2d\sin\theta \tag{4.1}$$

should be satisfied, where n is an integer, λ is the wavelength of the incident beam impinging on the sample, θ is the incident angle and d is the inter-atomic spacing between lattice planes (Cullity and Stock, 2014). A charge coupled device detector records intensities at the various angles of diffracted beams, which can be used as a signature to identify the chemical composition and orientation of the crystal structure (Waseda *et al.*, 2011). The direction of diffraction depends on the dimensions of the material's unit cell and the intensity depends on the nature of atoms.

XRD was used to identify inter-facial phase transitions during annealing of tungsten on 4H-SiC. A Bruker D8 Advance diffractometer was used for the measurements. The system uses a Cu ($K\alpha$) radiation source (1.54148 Å). The 2θ radiation source angle was maintained at 20°, and the detector angle scan was from 20° to 120°. The lower incident angel results in most information coming from the top layers of wafers and minimal information from the bulk. Sets of diffracted intensities and angles where compared with those found in the International center for diffraction data (ICDD) database to identify the phases present. All the measurements were carried out at NECSA.

4.5.4 Scanning electron microscopy

The evolution of surface morphology during annealing was studied using a Zeiss ultra plus field emission gun (FEG) scanning electron microscope. This instrument was developed by the microscopy department at the University of Pretoria from a conventional SEM. The source of the electron beam is a Schottky emitter not a thermionic emission filament like in conventional electron microscopes. An electric field focuses a narrow beam enabling higher spatial resolution and low signal to noise ratio. This increases density and coherence of the beam which improves the image brightness, a critical factor in the microscope‘s performance.

4.5.5 Raman spectroscopy

Raman scattering describes the inelastic scattering of light by matter. When photons interact with molecules, the photons may be scattered elastically (Rayleigh scattering) or inelastically. Inelastic scattering is referred to as Raman scattering. In the process of inelastic scattering, the scattered photon has less energy than the incident

photon, resulting in what is referred to as Stokes scattering, whereas when the scattered photon has a higher energy than the incident photon, the resultant is referred to as anti-Stokes scattering. The energy difference between the incident and scattered photon corresponds to the energy difference between two energy states of a material (Figure 1(a)). At room temperature, the ground state has more molecules than in the excited state. This results in a higher probability for Stokes scattering, hence Raman spectra are typically the number of Stokes scattered photons plotted as a function of the difference between the incident and scattered photon energy. This energy difference is usually given in terms of the Raman shift or wavenumber.

In Raman spectroscopy a sample is irradiated with a monochromatic laser beam, which interacts with the molecules of the sample and generates an infinitesimal amount of scattered light (Larkin, 2017). The scattered light is detected by a charge coupled device camera which then is used to produce a Raman spectrum. From the characteristic fingerprinting of Raman spectroscopy, the changes in molecular structure and crystalinity can be traced. Raman spectra were recorded on the epitaxial layer using a T64000 series II triple spectrometer system from HORIBA scientific, Jobin Yvon Technology, using the 514.3 nm laser line of a coherent Innova 70C series Ar laser (spot size ~ 5 μm) at a power of 0.17 mW with a resolution of 2 cm^{-1}

Confocal Raman microscopy was carried out using a Witec alpha 300 R Raman spectrometer with a 532.162 nm laser at 5.010 mW. Scans were typically between 200 cm^{-1} and 1800 cm^{-1}. Depth image scans were acquired over a width and depth of 70 m^{-2} with 200 points per line and 200 lines per image using an integration time of 1 s per point. In the measurements confocal resolution parameters were a depth resolution of 450 nm and spot size 350 nm with a 100X objective.

Clustering was done using Witec project FIVE software. It uses algorithms that group similar data sets together. A profile comprises a full Raman spectrum at each and every depth within the profile, and is then interrogated to generate intensity profiles based on material composition and structure. Raman peak intensity yields a profile of material concentration and distribution. Peak position yields a profile of molecular structure and phase, and material stress/strain. Peak width yields a profile of crystallinity and phase.

Chapter 5

Results and discussion

5.1 Introduction

Silicon carbide has become an important material in the implementation of next generation photonics. It has been recently shown to harbor the carbon antisite-vacancy pair ($C_{Si}V_C$) defect which has quantum functionality (Castelletto *et al.*, 2014). This defect is realized by first inducing the silicon vacancy and annealing it. Using defect engineering, this technology is set to surpass advances made in other similar systems because it is being developed on existing standard industrial practices, fabrication protocols and mechanisms. These include techniques such as irradiation, annealing and ion implantation. The motivation of this work was to establish sound device fabrication protocols to be used in the device implementation.

In this chapter the results will be presented. The first section (5.2) is a discussion of native defects found in as grown 4H-SiC. Section 5.3 is related to the defects induced by the sputter deposition of contacts on epitaxial 4H-SiC during device fabrication. Section 5.4 presents results obtained after annealing the fabricated devices. Finally Section 5.5 is on defects observed after exposing 4H-SiC to swift heavy ion irradiation. Unless otherwise specified, nitrogen doped 6.0×10^{16} cm^{-3} n-4H-SiC (8° off axis) epitaxially grown on highly doped substrate of 1.0×10^{18} cm^{-3} through CVD was used. The material was supplied by Cree. Inc.

5.2 Native defects

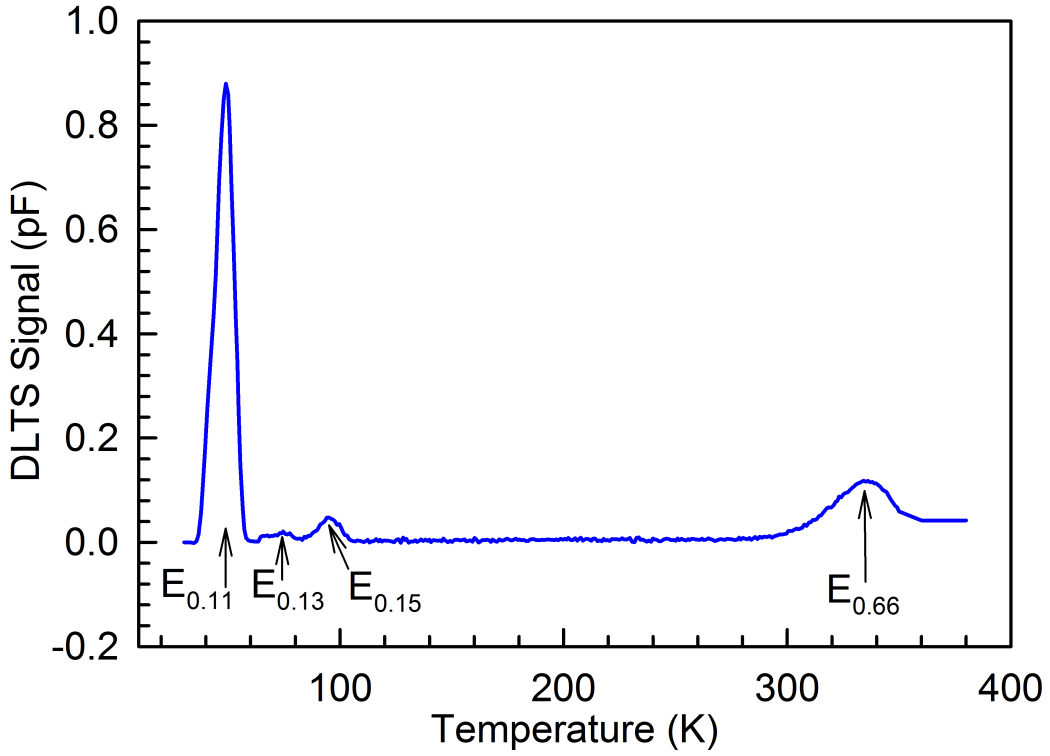

Figure 5.1: DLTS spectrum showing the electrically active defects in as grown 4*H*-SiC. The samples were Ni/4*H*-SiC Schottky barrier diodes measured at V_R= -5.0 V, V_P= 0.5 V and t_p= 1 ms.

Before processing, a comprehensive understanding of the defects in as-grown material as well as their structure are important. This allows for accurate identification of defects resulting from any subsequent processing steps. Native defects can cause high leakage currents and low breakdown voltages in devices fabricated on 4*H*-SiC, significantly limiting their performance (Kimoto *et al.*, 1999). They also result in lower carrier lifetime and affect recombination intensity in bipolar devices (Bergman *et al.*, 2001).

Figure 5.1 shows the DLTS spectrum from as-grown 4*H*-SiC showing four electrically active defects $E_{0.11}$, $E_{0.13}$, $E_{0.15}$ and $E_{0.66}$ (see Table 5.1). In the nomenclature used here E represents the electron trap and the number for example 0.11 represents activation enthalpy below the conduction band minima. The measurements were performed on Ni/4*H*-SiC Schottky barrier diodes, fabricated using resistive evaporation following the procedure in Section 4.2.

Table 5.1: Summary of electronic properties of defects in as-grown 4*H*-SiC, measured at V_R= -5.0 V, V_P= 0.5 V and t_p= 1 ms. E_T is the energy level of the defect below the conduction band minima in eV and σ_{ap} is the apparent capture cross section.

Defect label	$E_T \pm 0.02$ (eV)	σ_{ap} ±10% (cm^{-2})	Defect ID
$E_{0.11}$	0.11	1.5×10^{-11}	N impurity
$E_{0.13}$	0.13	1.9×10^{-14}	Ti impurity
$E_{0.15}$	0.15	2.5×10^{-16}	Ti impurity
$E_{0.66}$	0.66	3.7×10^{-15}	Z_1

Detection of these deep levels in DLTS scans is dependent on measurement conditions and can be influenced by temperature, minority carrier injection, exposure to light excitation and biasing (Hemmingsson *et al.*, 1998a). The $E_{0.011}$ is a shallow nitrogen donor occupying a cubic lattice site, whereas the $E_{0.13}$ and the $E_{0.15}$ are attributed to titanium (Ti) impurities (Paradzah *et al.*, 2015). Ti originates from parts of CVD reactors made from graphite, or from pumping oil (Dalibor *et al.*, 1997). The $E_{0.66}$ is also known as the Z_1 center and it exhibits negative U behavior and is discussed in Section 2.3 (Eberlein *et al.*, 2003). Table **??** gives a summary of the electronic properties of observed defects and their identities (ID).

A high quality substrate and a homogeneous temperature distribution are essential for low defect yields during growth. This is because defect structures in the substrate have been shown to replicate in the epitaxial layer (Kamata *et al.*, 2000). Also, a variable temperature distribution across the wafer results in defect structures (Zhang *et al.*, 2012). Defects like the Z_1 center have a high thermal stability of up to 1500° C (Danno and Kimoto, 2007). As a result, annealing is not a viable option for reducing their densities. Control can only be achieved by an optimized CVD growth process. This involves meticulous monitoring of the in-situ etching, C/Si ratios and the cooling process (Kimoto and Cooper, 2014) during CVD of epitaxial layers.

5.3 Sputter deposition

Metalization is a crucial processing step in the semiconductor device manufacturing industry. Magnetron sputtering is arguably the most versatile technique for depositing thin metal films. It can rapidly deposit metals with high melting points resulting in uniform films with good adhesion properties and can be optimized to produce desired stoichiometric compositions for particular purposes (Yeom *et al.*, 2017). In some cases the technique has been used to enhance semiconductor properties. Several

types of nano-structures and films have been established on silicon carbide through sputtering (Zhu *et al.*, 2013).

Due to the involvement of an incident plasma and metal particles, sputter deposition has been shown to induce atomic scale surface damage which cause lattice distortions and introduces electrically active defects (Volpi *et al.*, 2004). Incident particles have been used in the past to engineer beneficial defects in 4*H*-SiC (Castelletto *et al.*, 2014). Our aim was to examine the prospects of using incident particles which emanate from the sputter deposition process for both metalization and defect engineering. The defect of interest was the V_{Si} which has been successfully used to produce a single photon source after transforming to $C_{Si}V_C$ through annealing.

5.3.1 Experimental

Samples were cleaned and an ohmic contact was fabricated following the procedure in Section 4.2. The cleaning procedure was repeated in an ultrasonic bath at room temperature and 0.6 mm diameter circular tungsten Schottky contacts were deposited by DC magnetron sputtering on the epitaxial layer at room temperature. Tungsten was chosen because of its exceptional physical properties which make it suitable for high temperature operation (Berthou *et al.*, 2011). The deposition was carried out under a DC power of 1000 W and an Ar pressure of approximately 2.0×10^{-2} mbar. The target to sample distance was maintained at 7 cm. A thickness of 1000 Åwas deposited.

For completeness of the study, Ni Schottky contacts were fabricated on samples with the same ohmic contact as the sputtered ones following the same cleaning procedure. This is because resistive evaporation has been shown to not introduce defects during deposition and as such these samples could allow for measurements on the native defects only (Omotoso *et al.*, 2016). DLTS spectra were recorded at a scan rate of 2 K/min in the 15 – 360 K temperature range at a quiescent reverse bias of -5 V, filling pulse V_p of 0.5 V and filling pulse width of 1 ms.

In order to evaluate the suitability of the fabricated contacts for DLTS, their quality was assessed using current-voltage (I-V) and capacitance-voltage (C-V) measurements (Section 4.5.1). The Schottky-Mott rule was used to obtain C-V barrier height (Φ_{C-V}), and the carrier concentration (N_D) (Sze and Kwong, 2006). N_D was used to monitor carrier removal so that the accuracy of the DLTS measurements was not compromised through compensation of carriers (Mikelsen *et al.*, 2009). I-V barrier height (Φ_{I-V}), and the reverse leakage current at -2 V were determined using the

thermionic emission model (Grundmann, 2006). The errors in each calculation were determined based on the sensitivity of the instruments.

The samples were isochronally annealed in the 100°C - 600 °C temperature range in 100 °C incremental steps for 15 minutes.

5.3.2 Results

Figure 5.2 shows the *I-V* characteristics obtained from the SBDs made by sputter deposition of tungsten and the ones made through resistive evaporation of nickel. Table 5.2 shows the extracted diode parameters.

From the results it was observed that sputter deposition results in contacts with poorer thermionic emission characteristics when compared to those fabricated by resistive evaporation, as confirmed by the lower barrier heights and larger n values. This can be attributed to the exposure of the samples to an incident plasma together with the high energy incident particles during sputtering. It is well known that exposure of semiconductors to an incident plasma results in a change in surface

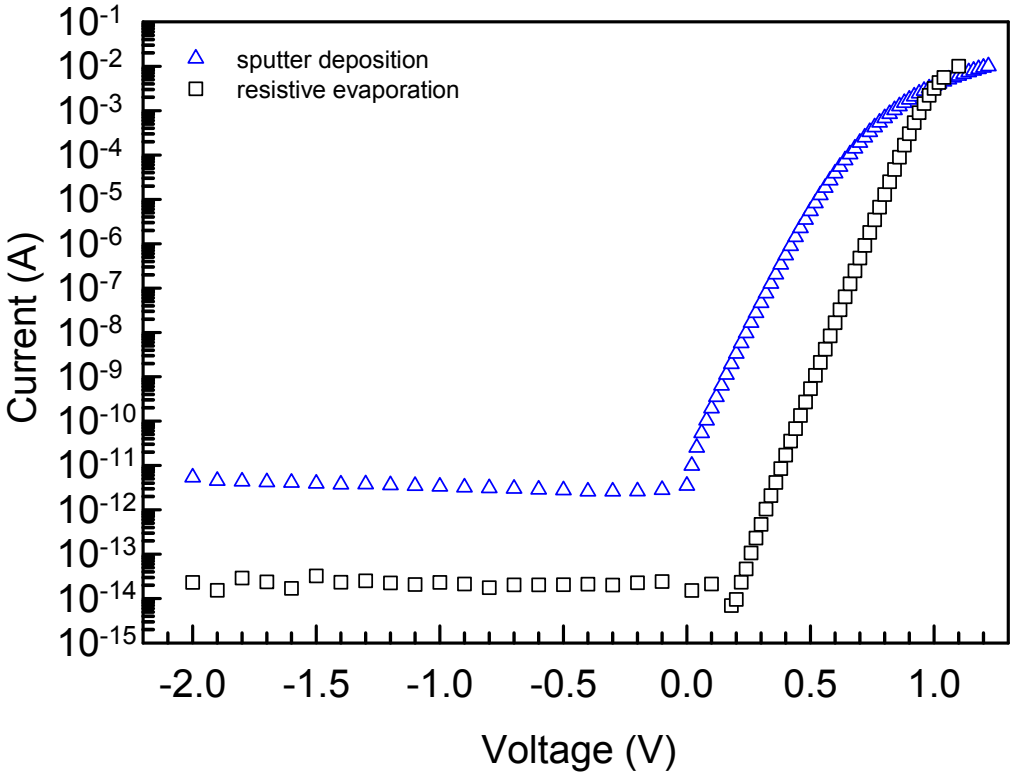

Figure 5.2: *I-V* characteristic of Schottky barrier diodes fabricated on n-4*H*-SiC using resistive evaporation and sputter deposition.

Table 5.2: Diode parameters of n-4H-SiC Schottky barrier diodes fabricated by resistive evaporation and sputter deposition.

Process	$n \pm 0.01$	$\phi_{IV} \pm 0.02$ (eV)	$\phi_{CV} \pm 0.02$ (eV)	$N_D \pm 0.1$ (cm^{-3})
Resistive evaporation	1.03	1.25	1.27	7.8×10^{15}
Sputter deposition	1.58	0.89	0.57	7.3×10^{15}

stoichiometry due to the high kinetic energy of the impinging particles (compared to resistive evaporation) altering the material's structural properties and hence introducing electrically active defects close to the surface (Auret *et al.*, 1997) This changes the position at which the Fermi level is pinned in some semiconductors which results in strong deviations in barrier height (Baca and Ashby, 2005).

The rectification properties of the measured devices were still suitable for DLTS measurements. The difference between the values of N_D of the samples fabricated by the two techniques was small in magnitude showing that sputter deposition resulted in carrier removal to a lesser extent, therefore, the accuracy of the DLTS measurements was not compromised. Figure 5.3 shows the DLTS spectra obtained at a rate window of 80 Hz

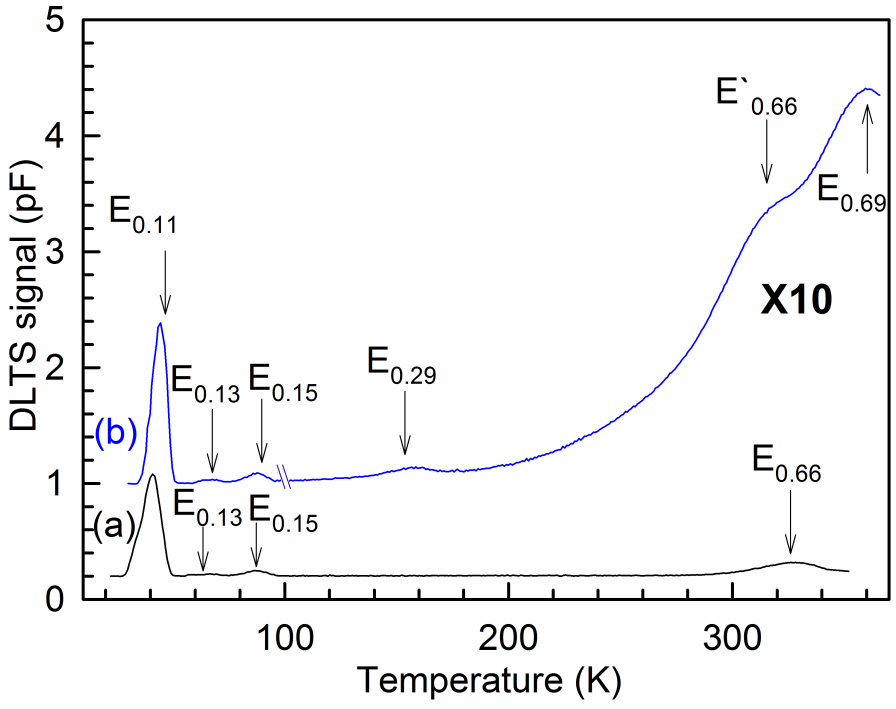

Figure 5.3: DLTS spectra of (a) the control sample obtained from Ni/4H-SiC Schottky barrier diodes fabricated by resistive deposition (b) W/4H-SiC Schottky barrier diodes fabricated by sputter deposition.(The E'$_{0.66}$ and E$_{0.69}$ have been magnified 10 times) Both spectra were observed at V_R= -5.0 V, V_P= 0.5 V and t_p= 1 ms. The E'$_{0.66}$ and E$_{0.66}$ represent the same defect after and before sputtering.

Curve (a) is the control spectrum obtained from Ni/4*H*-SiC Schottky barrier diodes fabricated using resistive evaporation. It shows the native $E_{0.11}$, $E_{0.13}$, $E_{0.15}$ and $E_{0.66}$ defects which have been discussed in Section 5.2. The energies were derived from the Arrhenius plots in Figure 5.4. For the devices produced by sputter deposition of W, Figure 5.3(b), defects observed were either native or have been reported before, except the $E_{0.29}$ which was observed for the first time in this sputtering experiment.

On spectrum (b), the peaks are observed to be sitting on a continuous skewed baseline. This baseline is detected in Laplace-DLTS measurements and inhibits accurate identification of defects as it contributes to background noise. A similar baseline has also been observed in heavy ion implanted GaN and alpha particle irradiated GaAs (van Rensburg *et al.*, 2009; Tunhuma *et al.*, 2016b). It appears that the deposition process induces a continuum of defects at the surface of the silicon carbide which are detected as the baseline. This is evidenced by the inconsistent Laplace-DLTS spectra obtained due to the baseline which gives inconsistent spectral density function peaks.

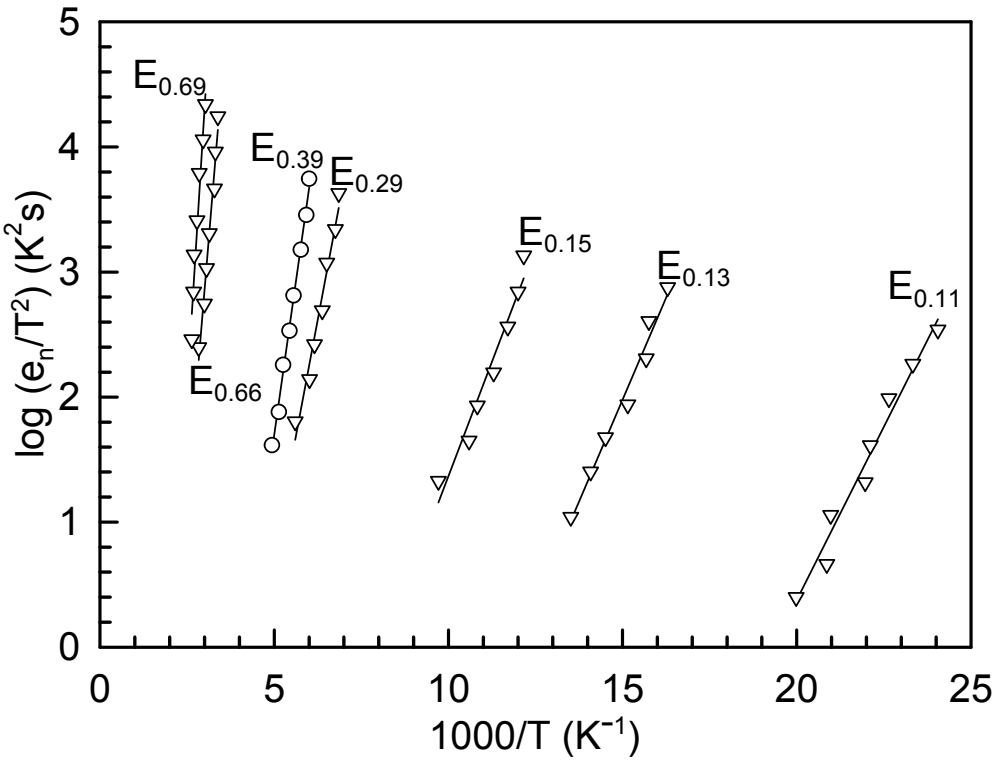

Figure 5.4: Arrhenius plots of W/4*H*-SiC Schottky barrier diodes fabricated by sputter deposition observed at V_R= -5.0 V, V_P= 0.5 V and t_p= 1 ms.

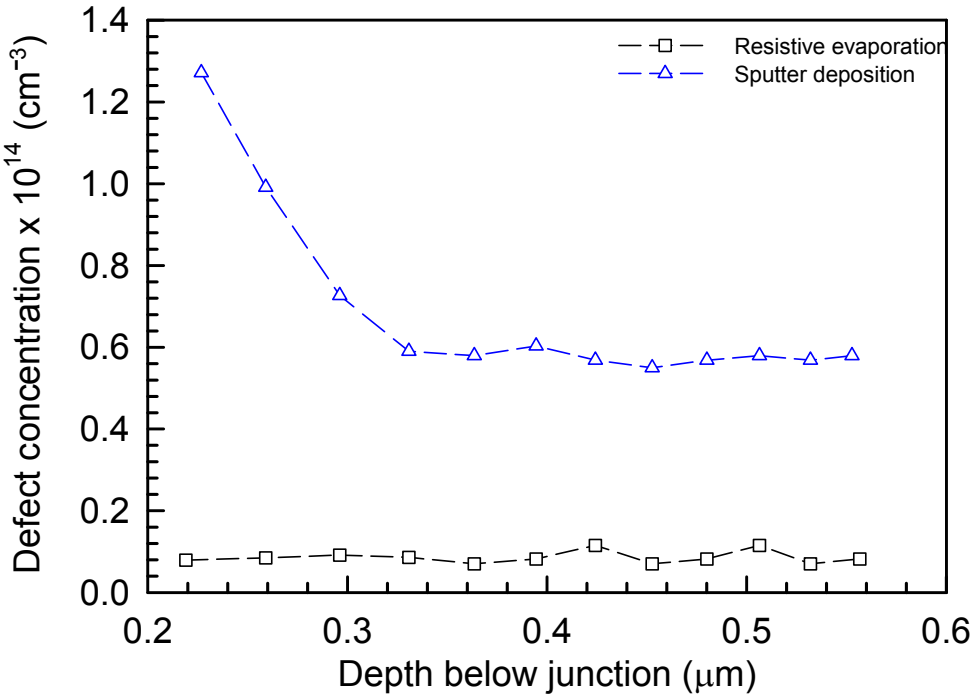

Figure 5.5: Depth and concentration of the E'$_{0.66}$ defect in W/4*H*-SiC Schottky barrier diodes fabricated by sputter deposition compared to control samples (fabricated resistive evaporation) measured at 320 K.

The fixed bias variable-pulse method was used to investigate the spatial distribution of the Z_1 center ($E_{0.66}$ defect) after irradiation and on the control sample made by resistive evaporation at 320 K. A marked increase in the defect concentration after sputter deposition was observed when compared to the resistive deposition samples (Figure 5.5). It has been reported that incident irradiation increases the concentration of the Z_1 defect (Hemmingsson *et al.*, 1998a). The defect concentration after sputter deposition shows a steady decrease with increasing depth. This could suggest that the defect is highly concentrated at the surface.

It is worth noting that this (E'$_{0.66}$)peak's defect concentration is now a summation of the concentration of the E'$_{0.66}$ and the $E_{0.69}$ defects. Due to the proximity of the two energy levels the DLTS signal will be a combination of both. As such, unless these defects are clearly split one cannot make any clear deductions about the actual concentration of the Z_1 after any form of processing or irradiation. This would require the use of Laplace-DLTS. However, Laplace-DLTS also detects the baseline on which the peaks are sitting in Figure 5.3. This appears inconsistently in the spectral density function making it impossible to observe the fine structure of the two defects ($E_{0.66}$ and $E_{0.69}$).

The $E_{0.29}$ defect is unique and has only been observed after sputter deposition in the current work. It has not been previously reported in 4*H*-SiC. The defect is induced by heavy metal or gas ions that emanate from the sputter deposition process. It may, therefore, be a cluster or a complex of impurities from the deposition residue.

Introduction of the $E_{0.69}$ close to the Z_1 center has been attributed by Asghar *et al.* (2007) to the interaction of the Z_1 with incident radiation which introduces an overlapping silicon vacancy (V_{Si}) transforming it into a complex. The overlapping vacancy is discussed in Section 2.3. Further confirmation of the identity can be found in the DLTS spectra of observed defects in Figure 5.6. V_{Si} anneals out completely at 600°C as reported by Kawasuso *et al.* (2001). This V_{Si} has been linked to complexes formed after thermal treatment that can be employed as single photon sources in 4*H*-SiC (Castelletto *et al.*, 2014; Bockstedte *et al.*, 2004). In that regard, it is proposed that sputter deposition may be used simultaneously for both metalization and to induce the V_{Si}.

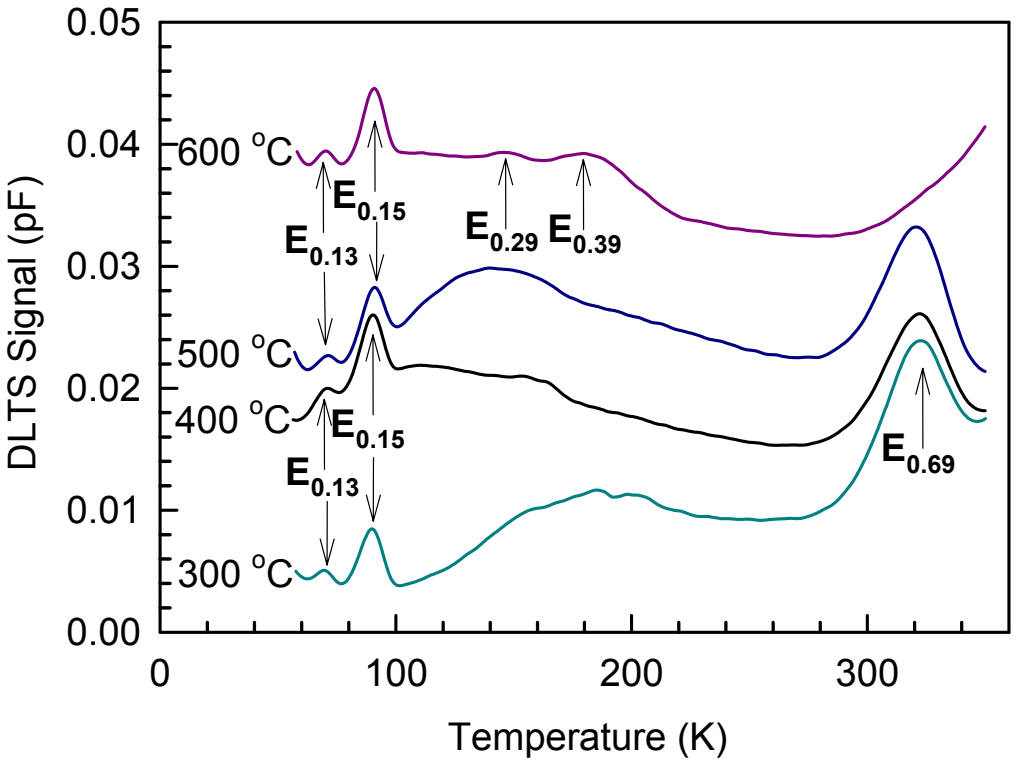

Figure 5.6: DLTS spectra of of W/4*H*-SiC Schottky barrier diodes observed during isochronal annealing recorded at a quiescent reverse bias of -2 V filling pulse 0.5 V and pulse width (t_p)of 1 ms. A reverse bias of -2 V was used to probe near surface defects only which were induced by the sputtering.

5.3.3 Concluding remarks

Sputter deposition of W on 4*H*-SiC induced the $E_{0.29}$ defect which is unique and has not been reported previously. The defect may be a cluster or complex of impurities incident on the semiconductor from the sputter deposition process. Sputter deposition also induced the $E_{0.69}$ which anneals out at 600 °C showing that it is silicon vacancy related. Irradiation induced defects, V_{Si} in particular, have been linked to single photon sources in 4*H*-SiC. The use of sputter deposition has been proposed for both metalization and to induce the V_{Si} in n-4*H*-SiC.

5.4 Annealing

5.4.1 Introduction

Once the V_{Si} defect is induced, thermal treatment plays an important role in transforming it into the $C_{Si}V_C$ (Castelletto *et al.*, 2014). In this section devices fabricated using sputter deposition were annealed in argon and the arising defects were monitored. Associated evolution in contact properties like the morphology and phase composition were studied to account for the observed changes in the bandgap. All the results will be presented first followed by an overall discussion.

5.4.2 Experimental

W/4*H*-SiC samples fabricated in section 5.3 were subjected to thermal treatment in the 100-1100 °C temperature range using a quartz tube with flowing Ar in 100 °C incremental steps. After each 15 minute annealing step the contact quality was evaluated using *I*-*V* and *C*-*V* measurements (Section 4.5.1). Changes brought about by the annealing would be noted in the process. DLTS spectra were recorded at a scan rate of 2 K/min in the 15-360 K range. Wide angle X-ray diffraction was carried out to identify any phase transitions after each annealing step. A Bruker D8 Advanced diffractometer XRD system with a Cu Kα radiation source was used at 40 kV and 45 mA. The 2θ radiation source angle was maintained at 20° and the detector angle scan was from 20° to 120° at 0.03° steps. Scanning electron microscopy (SEM) was also carried out after each annealing temperature using a Zeiss Ultra Plus FEG-SEM to study the evolution in surface morphology.

5.4.3 Results

A summary of the parameters obtained after each annealing step is listed in Table 5.3.

5.4.3.1 *I-V* and *C-V* measurements

This data is representative of a large number of samples that were measured. As the isochronal annealing steps progressed the *C-V* characteristics remained almost unchanged with a gradual decrease in ideality factor until 700 °C where there is a sharp increase in the *C-V* barrier height accompanied by an increase in the zero bias capacitance. Thereafter, there is a gradual increase in the *C-V* barrier height until 1100 °C. There is an increase in the Φ_{IV} for annealing between 700 and 1000 °C. Also, a significant decrease in the value of n is observed up to 900 °C. At 1100 °C a sharp decrease in the *I-V* barrier height and increase in *C-V* barrier height are also noted. There is a major degradation in the diode thermionic emission characteristics at the 1100 °C annealing step with an increase in n and a sharp decrease in the *I-V* barrier height and N_D. Comparing the initial and final devices, the *I-V* characteristics showed a gradual trend towards poor rectifying behavior and a decrease in reverse leakage current with increasing annealing temperature up to 900 °C as shown in Figure 5.7. Above 900 °C the leakage current starts increasing. The quality of the devices were appropriate for DLTS measurements.

Table 5.3: Diode *I-V* and *C-V* parameters obtained from as-deposited and annealed W/4*H* Schottky barrier diodes. Isochronal annealing was done for 15 minutes in the 100° C to 1100° C temperature range.

Temperature	$n \pm 0.01$	$\phi_{IV} \pm 0.02$ (eV)	$\phi_{CV} \pm 0.02$ (eV)	$N_D \times 10^{15} \pm 0.1$ (cm^{-3})
As deposited	1.58	0.89	0.57	7.8
100	1.22	0.73	0.81	7.5
200	1.21	0.73	0.83	7.6
300	1.21	0.71	0.88	7.7
400	1.18	0.82	0.97	7.7
500	1.13	0.82	1.03	7.8
600	1.12	0.82	1.09	7.8
700	1.10	0.82	1.87	5.9
800	1.15	0.90	1.15	7.7
900	1.10	0.97	1.32	7.4
1000	1.22	1.03	1.55	7.3
1100	2.37	0.82	1.87	6.7

Then overall trend shows a higher ideality factor and lower I-V barrier height and high series resistance.

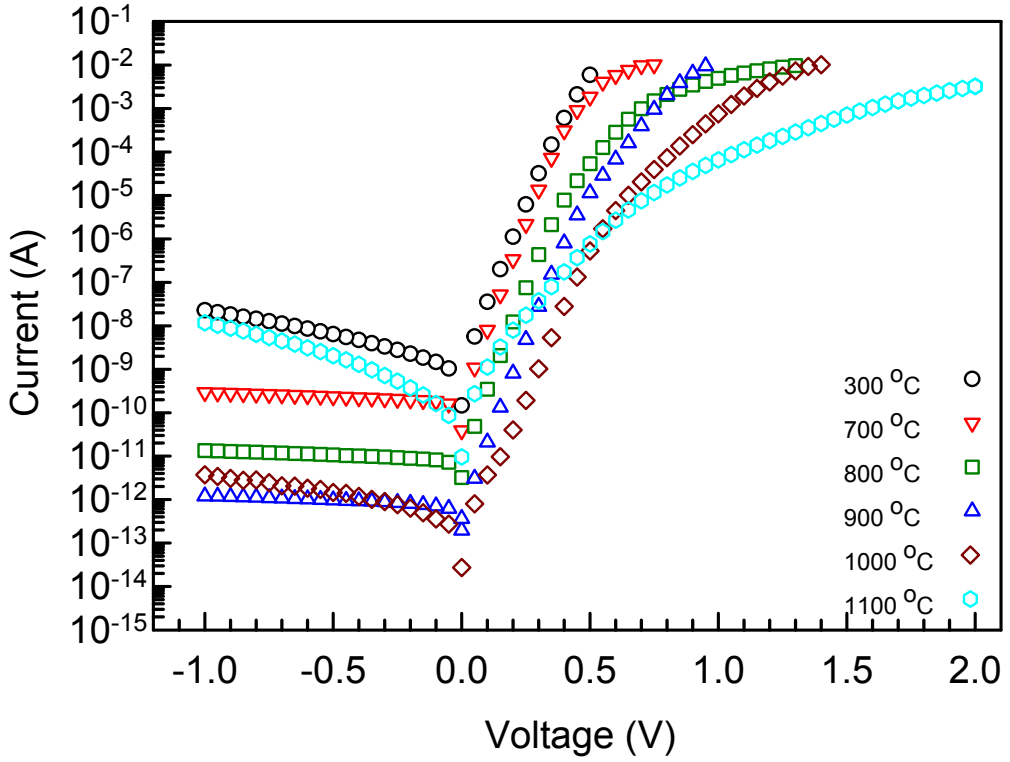

Figure 5.7: *I-V* characteristics of of W/4*H*-SiC Schottky barrier diodes observed during isochronal annealing for 15 minutes at different temperatures

5.4.3.2 DLTS

After annealing below 300 °C (Figure 5.6), the DLTS spectra showed only the native defects and sputter deposition induced damage. At 300 °C the damage due to sputter deposition annealed beyond detection. Figure 5.8 shows the DLTS spectra obtained after annealing between 700 °C and 1100 °C.

The titanium impurity related $E_{0.15}$ is observed in all spectra and the $E_{0.66}$ (Z_1) is visible in the 800 °C – 1100 °C spectra but not in the 600 °C and 700 °C spectrum. The difference between the Z_1 ($E_{0.66}$) and the Z_2 ($E_{0.69}$) are described in Section 2.3. The electronic properties of the defects observed in this study are listed in Table 5.4. From annealing spectra of sputter deposition induced defects (Figure 5.6), the Z_2 ($E_{0.69}$) center was not detected at 600 °C (Figure 5.6). This was attributed to the

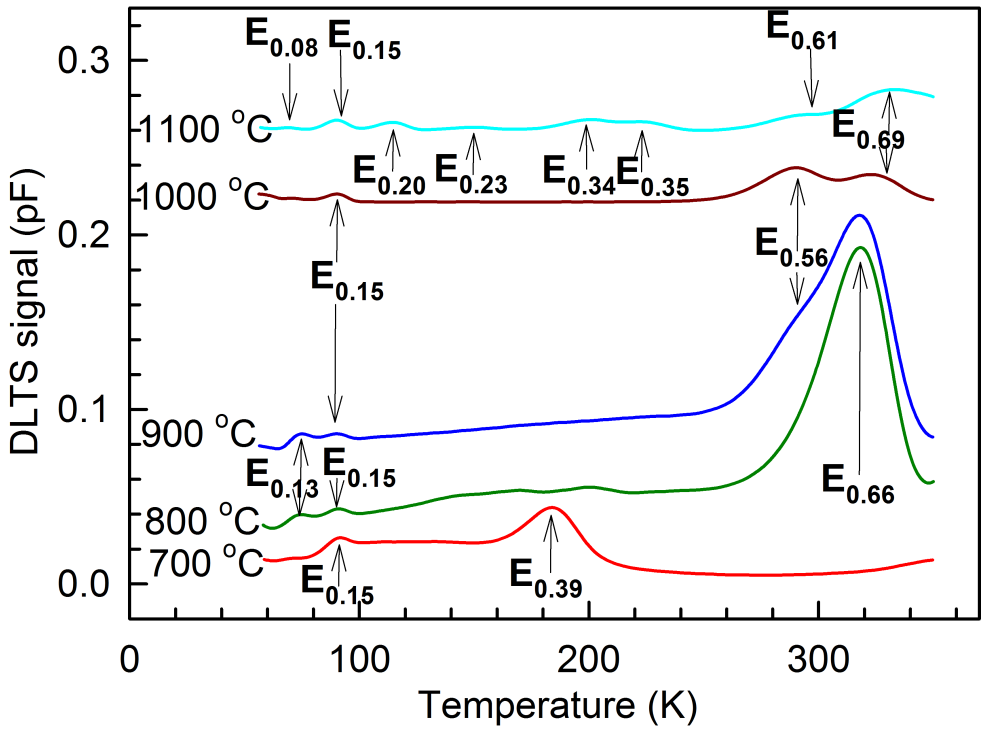

Figure 5.8: DLTS spectra of of W/4H-SiC Schottky barrier diodes observed during isochronal annealing recorded at a quiescent reverse bias of -2 V filling pulse 0.5 V and pulse width (t_p)of 1 ms.

defect being silicon vacancy related, the silicon vacancy anneals out at 600 °C. The Z_1 ($E_{0.66}$) defect reappears at 800 °C.

The $E_{0.39}$ starts to appear at 500 °C and gradually increases in size as the $E_{0.66}$ decreases in size until it goes completely beyond detection at 700 °C. At this point (700 °C) the $E_{0.39}$ is at its highest concentration. A concurrent increase in zero bias capacitance and C-V barrier height is also noticed at 700 °C as stated in Section 5.4.3.1. At 800 °C the $E_{0.39}$ was not detectable.

The $E_{0.56}$ appears after annealing at 900 °C. At 1000 °C, the $E_{0.56}$ was observed in addition to the $E_{0.69}$ defect. The $E_{0.13}$ has annealed out but the $E_{0.15}$ and $E_{0.59}$ are present and the Z_2 ($E_{0.69}$) appears. Then at 1100 °C the $E_{0.08}$, $E_{0.15}$, $E_{0.20}$, $E_{0.23}$, $E_{0.34}$, $E_{0.35}$, $E_{0.61}$ and $E_{0.69}$ where observed on the spectrum. Figure 5.9 shows Laplace DLTS spectra used to obtain the properties of the $E_{0.61}$, $E_{0.69}$ and $E_{0.82}$ defects at 303 K and 306 K. The measurements were carried out at a reverse bias of -2 V and

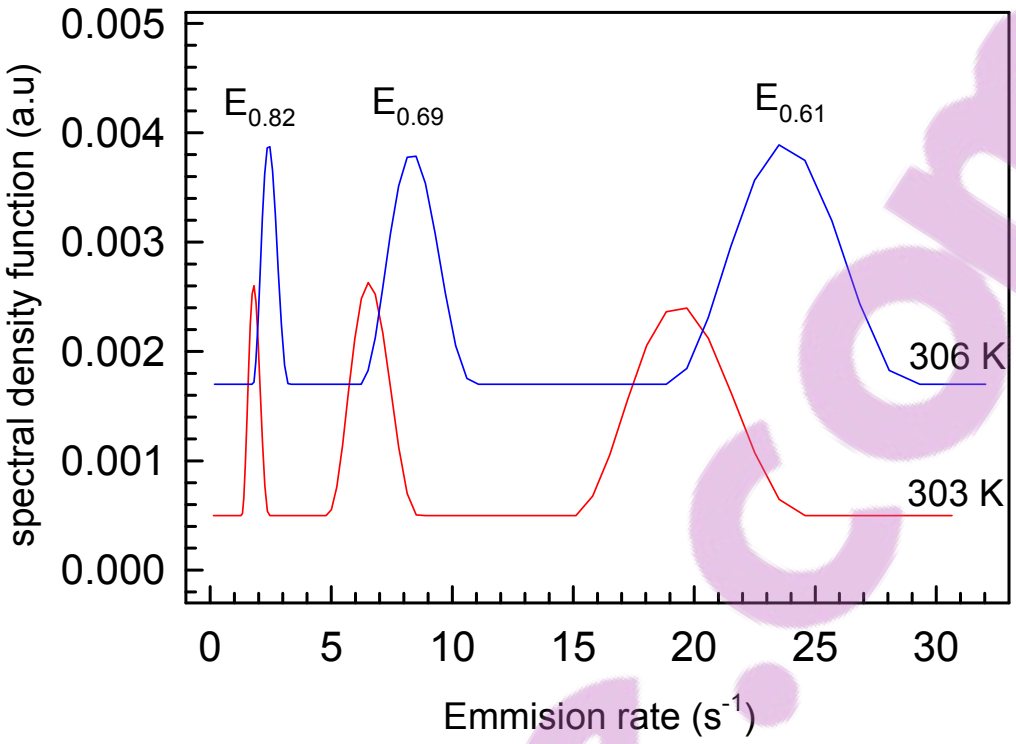

Figure 5.9: Laplace DLTS spectra showing some of the defects observed after annealing W/4H-SiC Schottky barrier diodes at 1100 °C at a reverse bias of -2 V filling pulse 0.5 V and pulse width (t_p)of 1 ms.

Table 5.4: Electronic properties of defects in W/4H-SiC observed during isochronal annealing in the 100-1100 °C temperature range. E_{T} is the energy level of the defect below the conduction band minima and σ_{ap} is the apparent capture cross section.

Defect label	$E_T \pm 2$ (meV)	σ_{ap} ±10% (cm^{-2})
$E_{0.08}$	81.2	2.7×10^{-18}
$E_{0.13}$	130	2.8×10^{-15}
$E_{0.15}$	146	3.3×10^{-16}
$E_{0.20}$	202	1.2×10^{-15}
$E_{0.23}$	231	1.9×10^{-15}
$E_{0.29}$	294	6.3×10^{-17}
$E_{0.34}$	336	1.7×10^{-16}
$E_{0.35}$	348	4.2×10^{-14}
$E_{0.39}$	392	4.2×10^{-14}
$E_{0.56}$	559	1.5×10^{-15}
$E_{0.61}$	613	9.2×10^{-16}
$E_{0.69}$	692	3.0×10^{-15}
$E_{0.82}$	818	2.2×10^{-13}

a forward bias of 0 V. The $E_{0.61}$ has been reported as the donor level of the Z_2 center (Section 2.3) (Eberlein *et al.*, 2003).

It is possible to do Laplace DLTS after annealing at 1100 °C because the continuum of defects that make up the baseline on DLTS spectra have been annealed out.

The $E_{0.08}$, $E_{0.20}$, $E_{0.23}$ $E_{0.34}$ and $E_{0.35}$ result from the thermal treatment as their introduction does not appear to be related to the $Z_{1/2}$ and other native defects. Their spatial distribution was determined using the fixed bias-variable pulse method described in Section 3.6. Depth profiling was done based on the correction proposed by Zohta and Watanabe (1982) (Equation 3.13). A reverse bias of -2 V was maintained. Depth profiles of the $E_{0.20}$, $E_{0.34}$ and $E_{0.35}$ are shown in Figure 5.10. The depth profile of the $E_{0.23}$ is not shown because it appeared to be surface state related due to the inconsistent L-DLTS spectra with multiple peaks. The signature of a defect in the bandgap can only be obtained if the spectral density function of L-DLTS is consistent in a particular temperature range.

The $E_{0.08}$ was of very small defect concentration ($< 1.0 \times 10^{10}\text{cm}^{-3}$) and is also not shown. A comparison of the depth profiles showed a similar trend with concentrations

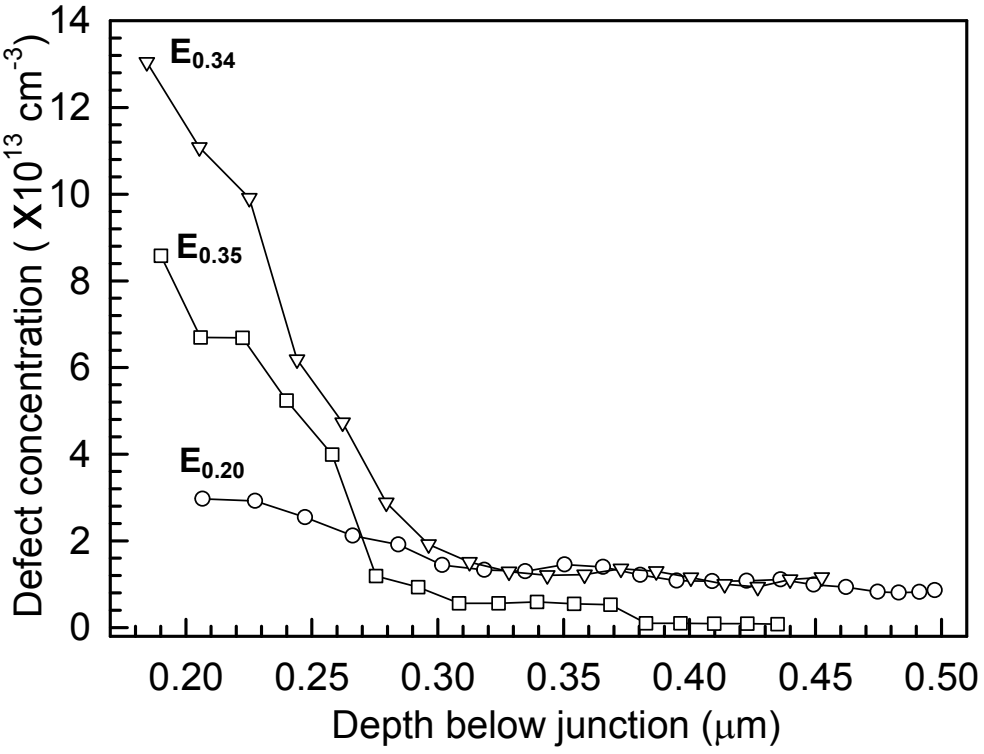

Figure 5.10: Depth and concentration of defects observed in 4*H*-SiC Schottky barrier diodes after annealing at 1100 °C.

that significantly reduced at 0.31μm confirming that they possibly emanated from the same source; most likely a reaction at the metal-semiconductor interface. This could be a carbide or a silicide formed at the surface.

5.4.3.3 X-ray diffraction

XRD results showed formation of various silicides, carbides and oxides during the thermal treatment.

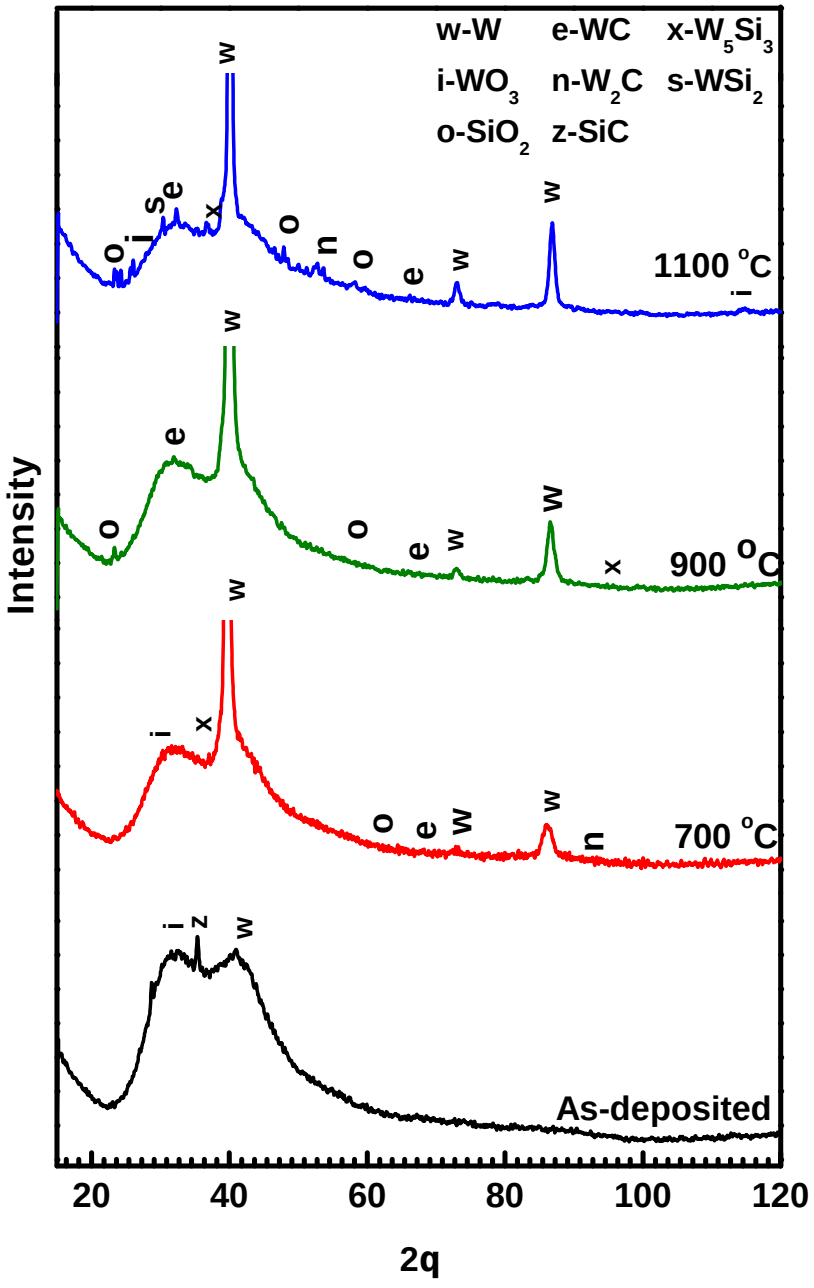

Figure 5.11: X-ray diffraction patterns of as-deposited W/4*H*-SiC samples and after annealing them at 700°C, 900°C and 1100°C in Ar for 15 minutes.

Tungsten is metastable (has stable states other than the state of least energy), and undergoes various eutectic reactions with both silicon and carbon during thermal treatment. Figure 5.11 shows the XRD patterns for the W/4*H*-SiC samples before and after annealing in Ar. The as-deposited pattern contained a WO_3 (-1 -1 1) peak at position 30.4°, a SiC (-1 -1 1) peak at 35.7° and a W (1 1 0) peak at 40.3°. Stability of these phases formed on deposition is a function of kinetics (Seng and Barnes, 2000). Previous depositions of tungsten on silicon carbide have also shown trace amounts of tungsten oxide (Lundberg *et al.*, 1996). The oxide could originate from natural oxidation in air as the samples are transferred from the deposition system to the measuring systems. It might also be introduced in small amounts in the tube furnace. The strong amorphous component is due to the deposition and unannealed nature of the W contact.

Annealing at 700 °C led to the emergence of two additional W peaks (1 0 2) and (2 2 0) at positions 73.2° and 87.4°. At 700 °C W starts forming the most thermodynamically stable phases. The material becomes more crystalline as evidenced by the narrowing width and increasing intensity of the W peak at 40.3°. Formation of silicides and carbides were observed showing that a reaction between W and SiC had taken place. The resulting phases could be associated with W_5Si_3 (4 0 0), SiO_2 (2 1 1), WC (1 1 0) and W_2C (2 2 0) at positions 37.4°, 60.4°, 70.5° and 93.7° respectively.

After annealing at 900 °C, additional peaks which could be SiO_2 (1 0 0) and WC (1 0 0) peaks were observed at positions 23.6° and 36.4°. The formation of these phases was an indication of further reaction of W and WO_3 with SiC. The samples annealed at 1100 °C had the following additional peaks: WO_3 (2 2 1), SiO_2 (3 2 7), W_2C (1 0 2) and WO_3 (5 2 1) at position 24.3°, 47.9°, 52.5° and 113.0° respectively. Formation of W_2C confirmed further reaction between W and C. These results are consistent with the predictions of the tenary phase diagrams calculated by Seng and Barnes (2000). They predicted stable phases of WC and W_5Si_3 above 700 °C. The differences are on the prediction of formation of WC and WSi_2 on the as-deposited samples.

To optimize the detection of thin surface features proper grazing incidence XRD is required.

5.4.3.4 Scanning electron microscopy

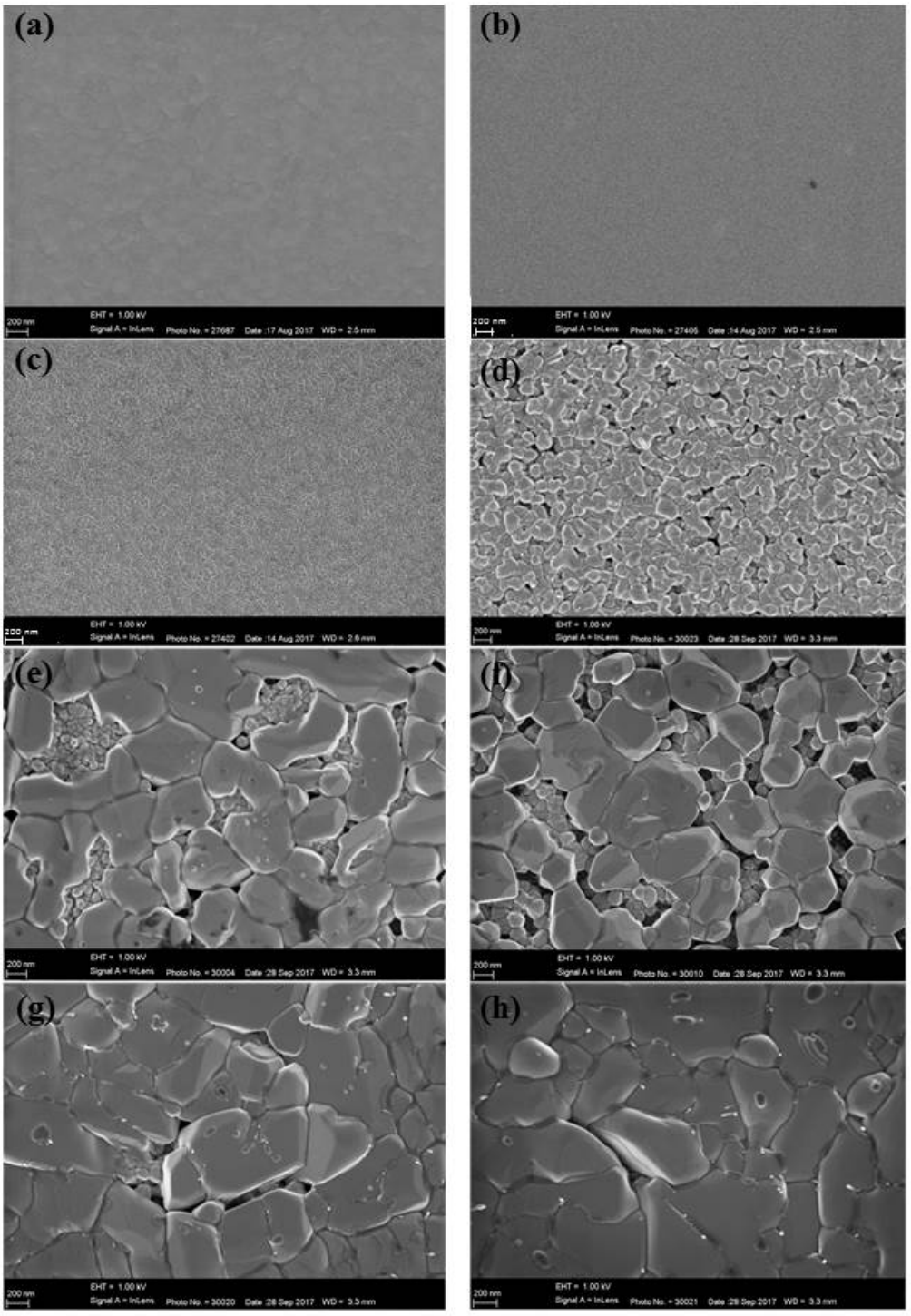

Figure 5.12: SEM images for (a) as deposited W/4*H*-SiC Schottky barrier diodes on the tungsten metal surface, and after annealing in Ar for 15 minutes at (b) 500 °C, (c) 600 °C, (d) 700 °C, (e) 800 °C, (f) 900 °C, (g) 1000 °C and (h) 1100 °C respectively.

In a previous study were inter-diffusion of tungsten into silicon carbide was confirmed, SEM analysis showed associated morphological changes to the tungsten surface (Thabethe *et al.*, 2017). The SEM micrographs of W deposited on 4*H*-SiC before and after annealing showing morphological evolution are depicted in Figure 5.12. The as-deposited sample shows a continuous tungsten surface. An uneven patterning is observed on the tungsten film. This could be resulting from the rf etching of 4*H*-SiC which was used to ensure that the surface was atomistically clean before tungsten deposition. It can be seen that the whole surface is covered with W film after deposition.

No changes were observed on the surface after annealing up to 500 °C. Annealing at 600 °C resulted in a pronounced change in the surface structure, with the continuous film breaking up into evenly distributed smaller grains of no preferred orientation. The morphological evolution after annealing at 700 °C and 900 °C shows grain coarsening with parasitic growth of bigger grains from the smaller ones. Bigger grains appear to be stacked on the smaller ones and their formation may represent phase transformations to form other phases as observed in the XRD results in the previous section. A similar rough surface was observed on a W/6*H*-SiC interface where diffusion was confirmed using Rutherford backscattering spectroscopy after annealing and they attributed it to stress assisted growth (Thabethe *et al.*, 2017).

Annealing at 1100 °C (Figure 5.12(h)) resulted in larger grains which almost cover the entire surface. Cavities were also observed and reported when W diffused into Si after annealing in oxygen and/or vacuum between 776°C and 960 °C (de Luca *et al.*, 2014).

5.4.4 Discussion of results

The gradual decrease in concentration of the $E_{0.69}$ (Z_2 center) with the introduction of the $E_{0.39}$ after annealing between 400 °C and 600 ° suggests that these levels are possibly related or emanate from the same defect. The spike in *C*-*V* barrier height at 700 °C was accompanied by the $E_{0.69}$ (Z_2 center) going below the detection limit of DLTS and the appearance of the $E_{0.39}$ on the DLTS spectrum (Figure 5.8). Such a link between *C*-*V* barrier height and defect concentration has also been reported by (Tunhuma *et al.*, 2016a) in GaAs. Asghar *et al.* (2007) also observed the Z_2 center going below detection after annealing at 600 °C for 30 minutes. They attributed the suppression to the annealing out of the silicon vacancy (Z_2) and the capture of the Z_1 by inactive sites such as dislocations and micropipes. Their assertions, however,

lacked a plausible explanation on how this related to the nature of the defect or the physical mechanism around the capture. The $Z_{1/2}$ centers are made up of two negative U centers having inverted level ordering. Negative U behavior is when one defect traps two electrons with the second one being more strongly bound than the first (Son *et al.*, 2012). Processes of the donor level capturing and the acceptor level emitting can be described by the following equations (Hemmingsson *et al.*, 1998a)

$$Z_i^+ + e^- \leftrightarrow Z_i^0, \tag{5.1}$$

$$Z_i^0 + e^- \leftrightarrow Z_i^-, \tag{5.2}$$

where the subscript $i = 1$ or 2.

From these equations four peaks would be anticipated to appear on the spectrum in a conventional DLTS scan, two for each negative U center. According to Hemmingsson *et al.* (1998a) this is not the case because the binding of the capture strengthens when the two electrons are captured by the negative U center during each filling pulse and cannot be subsequently released during a pulse relaxation. This explains the inability to detect the Z_1 at 700 °C but does not explain concurrent detection of the $E_{0.39}$.

Pulse properties and pulsing conditions have been shown to play a major role on the results of DLTS measurements in negative U centers (Seebauer and Kratzer, 2008). The $E_{0.39}$ may result from the donor level of the Z_1 negative U center. This is because a lower filing pulse was used (2.5 V) and shorter pulse length (1 ms) than previous authors who didn't see the donor level. The pulse is only long enough to fill the donor defect level with one electron altering the capture cross section in the process. As a result, the defect will not capture the second electron easily. A similar result was observed with the ES1 defect in GaN by Auret *et al.* (1999) which also is a negative U center. The DLTS pulse is therefore only sufficient for reaction 5.1 in an emission of the poorly bound electron. Gradual introduction of the $E_{0.39}$ and shefting of the peak, seems to point out that the thermal treatment actually influences the first electron to be more loosely bound.

Based on these observations, changes observed on the electrically active defects in the bandgap below 700 °C, can therefore, not be correlated with the phase transitions at the interface, but can be linked to the $Z_{1/2}$ defects undergoing changes during thermal treatment. Although the XRD results verified that there were phase reactions at the interface, by revealing the presence of WC and W_2C and WSi_2, a similar defect

behaviour of the Z_1 was observed using gold and nickel contacts on 4*H*-SiC, therefore all the observed changes in defects here cannot be correlated to W/4*H*-SiC interfacial reactions (Asghar *et al.*, 2007).

No new defects were observed after annealing at 800 °C. Lundberg *et al.* (1996) also saw that there was no reactions between tungsten and silicon carbide below 800 °C even after annealing for 2 hours. However, several defects were observed in the bandgap after thermal treatment in the 900 °C – 1100 °C temperature range. Laplace DLTS depth profiles of the $E_{0.20}$, $E_{0.34}$ and $E_{0.35}$ defects, induced by annealing at 1100 °C follow a similar trend in terms of concentration, showing that they might have emanated from same process. They were possibly created by the inter-diffusion of a reaction product formed at the metal-semiconductor interface, which was probably a carbide, silicide or oxide detected by the XRD. According to Kakanakova-Georgieva *et al.* (1999) there is a breaking of Si–C bonds, so that the tungsten interacts with liberated carbon atoms forming tungsten carbide as well as with silicon yielding tungsten silicide.

From the depth profiles for a 15 minute annealing interval the average diffusion rate of the thermal reaction product would be approximately 5.71×10^{-10} μm.s^{-1}. The depth profiles in Figure 5.10 may be for defects introduced by the diffusion of WC as was observed using time of flight secondary ion mass spectroscopy (ToF-SIMS) by Rogowski and Kubiak (2015) after annealing above 1200 °C. In this case, it was detected after thermal treatment at a lower temperature than Rogowski and Kubiak (2015) by the high resolution of Laplace DLTS. In the 15 – 360 K temperature range it has been showed that oxygen related defect centers in 4*H*-SiC occupy shallower levels than what we have observed (Dalibor *et al.*, 1998). We therefore rule out produced oxides as causes of the observed defects. From the SEM micrographs, the coarsening of grains and the accompanying formation of cavities are consistent with previous morphological observations where tungsten migrated into Si and SiC (Thabethe *et al.*, 2017).

The migration of reaction products into the lattice is not a desirable outcome for the generation of single defects. This is because the purity of the materials plays an important role in the quality of the photon source (**?**).

The introduction of the defects after annealing at 1100 °C was accompanied by a major deterioration of the device thermionic emission *I*-*V* characteristics, as well as modifications in the interfacial composition. Traps act as recombination centers, trapping electrons, and this influences the observed *C*-*V* and *I*-*V* characteristics resulting in poorer diode characteristics. A similar result has also been observed

for annealing of Al contacts on 4*H*-SiC in the 900 °C – 1100 °C temperature range (Rogowski and Kubiak, 2013). The various silicide and carbide phases produced also introduce inhomogeneities in the barrier height, which also impacts on diode *I-V* characteristics. With respect to the nature of the defects observed, it is hereby proposed that they are interstitials formed by the tungsten, or carbides or silicides occupying vacant sites which they encounter during diffusion through the lattice. This is known as the dissociative diffusion mechanism (Biderman *et al.*, 2016).

5.4.5 Concluding remarks

Thermal annealing of the W/4*H*-SiC Schottky barrier diodes in the 400 – 700 °C temperature range resulted in changes in *I-V* and *C-V* characteristics which were attributed to the negative U behaviour of the Z_1 center ($E_{0.66}$). Further, the results also show that thermally induced physical changes to contacts resulted in modification of the electronic properties of the W/4*H*-SiC devices. From the depth profiles, it appeared that inter-diffusion of silicides, carbides and other impurities produced during the thermal reactions and phase transitions above 1100 °C, at the W/4*H*-SiC interface migrate into the silicon carbide, introducing electrically active defects ($E_{0.23}$, $E_{0.34}$ and $E_{0.35}$) in the bandgap. The introduction of the defects was detected at relatively lower annealing temperatures compared to other techniques used in past studies due to the high sensitivity of Laplace-DLTS.

5.5 Swift heavy ion irradiation

5.5.1 Introduction

Having successfully induced the silicon vacancy in 4*H*-SiC using W sputter deposition; annealing the resulting devices resulted in diffusion of the metal into the semiconductor. This is an unfavourable outcome for photonics applications where purity of the semiconductor is a high priority. An alternative is to induce the silicon vacancy using noble gas particles. A noble gas is inert, therefore it will not react with the semiconductor. However, because of mass considerations, heavy noble gas ions have a high propensity to disrupt the lattice structure rendering it unusable for both electronics and photonics purposes (Hlatshwayo *et al.*, 2016). This problem is compounded by the swiftness of the ions required for irradiation or implantation. Slower ions were not consider as they cause rapid armophization of SiC.

Our aim was to use relatively low fluencies of swift heavy Xe^{26+} ion irradiation to induce the V_{Si}. Raman spectroscopy, Monte Carlo SRIM simulations and DLTS were used to probe the disorder and electrically active defects induced. The aim was to understand the nature and occurrence of defects formed under swift heavy ion irradiation. The integrity of the lattice structure would be monitored using confocal Raman spectroscopy, by performing spatial mapping of the cross section of 4*H*-SiC wafers.

5.5.2 Experimental

Nitrogen doped, n-type (0001) oriented 4*H*-SiC (8° off axis) wafers supplied by Cree inc were used. The wafers consisted of a 6.0 μm epitaxial layer of doping density $6 \times 10^{16}\text{cm}^{-3}$ grown on a highly doped substrate of approximately $1 \times 10^{18}\text{cm}^{-3}$ The samples were cleaned and a Ni ohmic contact was deposited following the procedure in Section 4.2.

Room temperature irradiation of 167 MeV, Xe^{26+} ions was done on the epitaxial layer at a fluence of 5×10^{11} cm^{-2}. One week later, Raman spectra were recorded on the epitaxial layer with a WiTec Alpha 300 Raman spectrometer, using the 514.3 nm laser line of a coherent Innova 70C series Ar^+ laser (spot size approximately 2 mm) at a power of 0.17 mW with a resolution of 2 cm^{-1}. Raman depth image scans were acquired over a width and depth of 70 μm^{-2} with 200 points per line and 200 lines per image using integration time of 1 s. Atomic force microscopy (AFM)

was performed on pristine and irradiated samples using a Bruker Dimension Icon Nanoscope 5 scanning probe microscope with ScanAsyst.

1000 Å thick, Ni circular Schottky contacts were then fabricated on the irradiated epitaxial layer using resistive evaporation. The resistive evaporation (RE) technique does not introduce defects during deposition. For this reason Ni metal was chosen as a contact metal because it can be deposited using RE, unlike W which cannot be easily deposited using RE because of its physical properties. For control purposes un-irradiated samples were also fabricated in the same procedure. DLTS measurements were performed in the 40 – 370 K temperature range at a quiescent reverse bias of -5 V and a filling pulse of 1 V. The pulse width was 1.0 ms.

5.5.3 Binary collision approximation

The radiation damage from the exposure of n-4*H*-SiC to swift heavy ions was simulated using Binary collision approximations in the SRIM (Stopping and Range of ions in matter) framework (Ziegler *et al.*, 2010). SRIM performs calculations on interactions of ions with matter using quantum mechanics based predictions of ion-atom collisions. This is achieved by employing several statistical algorithms. TRIM is the subroutine which is used to calculate displacements per atom (dpa) by an incident energetic particle. Dpa is a measure of primary radiation damage and can give insights on the density of defects induced by incident radiation on the semiconductor material as well as their spatial distribution.

The SRIM software has a graphical user interface where one can input data on the incident ions and their energy and information on the target and its properties like wafer thickness. After saving the input and running, the program calculations begin and they can be paused and resumed at any instance. Room temperature simulations were done using SRIM 2012 using displacement energies of 20 and 35 eV for the C and Si respectively. The ion fluence was converted into displacements per atom (dpa) using the following equation (Hlatshwayo *et al.*, 2016)

$$dpa = \frac{vac/ion\mathring{A}}{\rho_c}\phi \tag{5.3}$$

where ϕ is the ion fluence, ρ_c is the theoretical density of 4*H*-SiC (9.641×10^{22} at/cm^3) and vac/ionÅ is the vacancy per ion ratio obtained from SRIM.

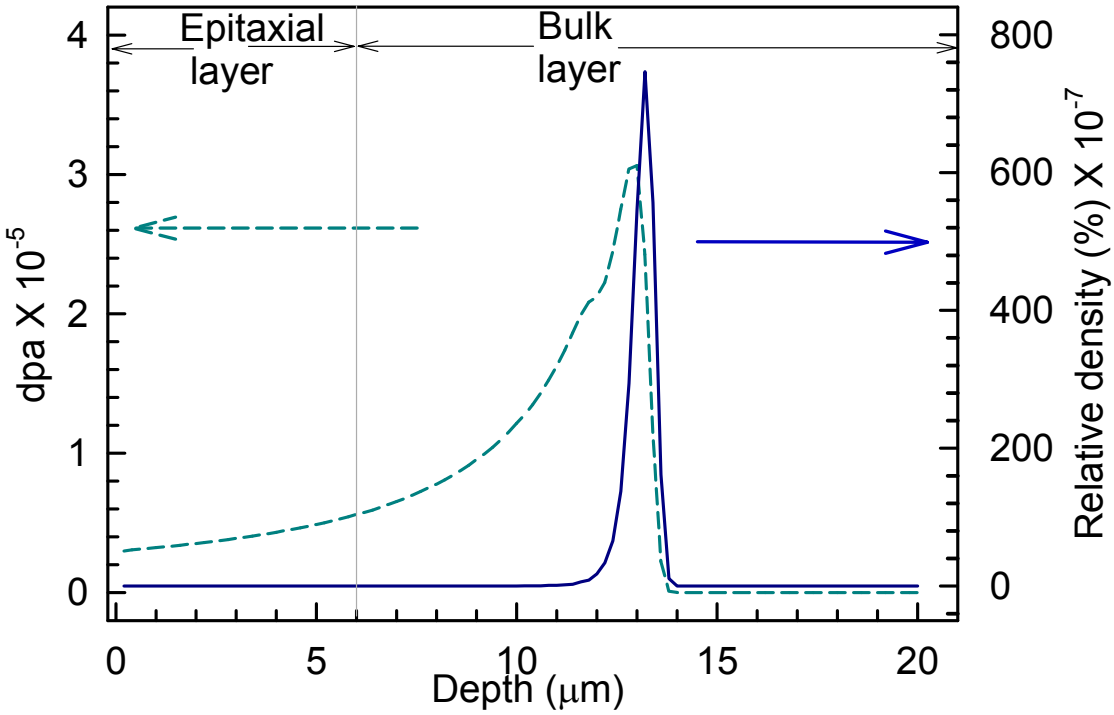

Figure 5.13: Relative Xe density and displacement per atom (dpa) as a function of depth obtained from SRIM simulations on 4H-SiC at a fluence of 5×10^{11} cm^{-2} .

From the SRIM results (Figure 5.14) at a fluence of 5 $\times 10^{11}$ cm^{-2}, the maximum dpa was found around 13 μm and the projected range was 13.02 μm. The epitaxial layer that was used had a thickness of 6.0 μm which is less than the projected range. This shows that the ions penetrated the whole epitaxial layer and were mainly concentrated in the bulk layer. Electron energy loss was therefore experienced by the epitaxial layer and so only point defects are anticipated to have formed. The maximum dpa was approximately 3.2×10^{-5} μm. It is less than the 0.3 dpa threshold for amorphization of silicon carbide (O C̃onnell *et al.*, 2014).

When exposed to incident Xe radiation, ion solid interactions result in point defect generation that leads to lattice distortions due to electronic energy loss. Two well accepted models for the aftermath of the interactions are the thermal spike model and the coulomb explosion model (Debelle *et al.*, 2012; Li and Wang, 2014). Later on, ballistic processes in the nuclear energy loss regime, result in damage cascades with vacancies trapping gas particles and creation of interstitial defects.

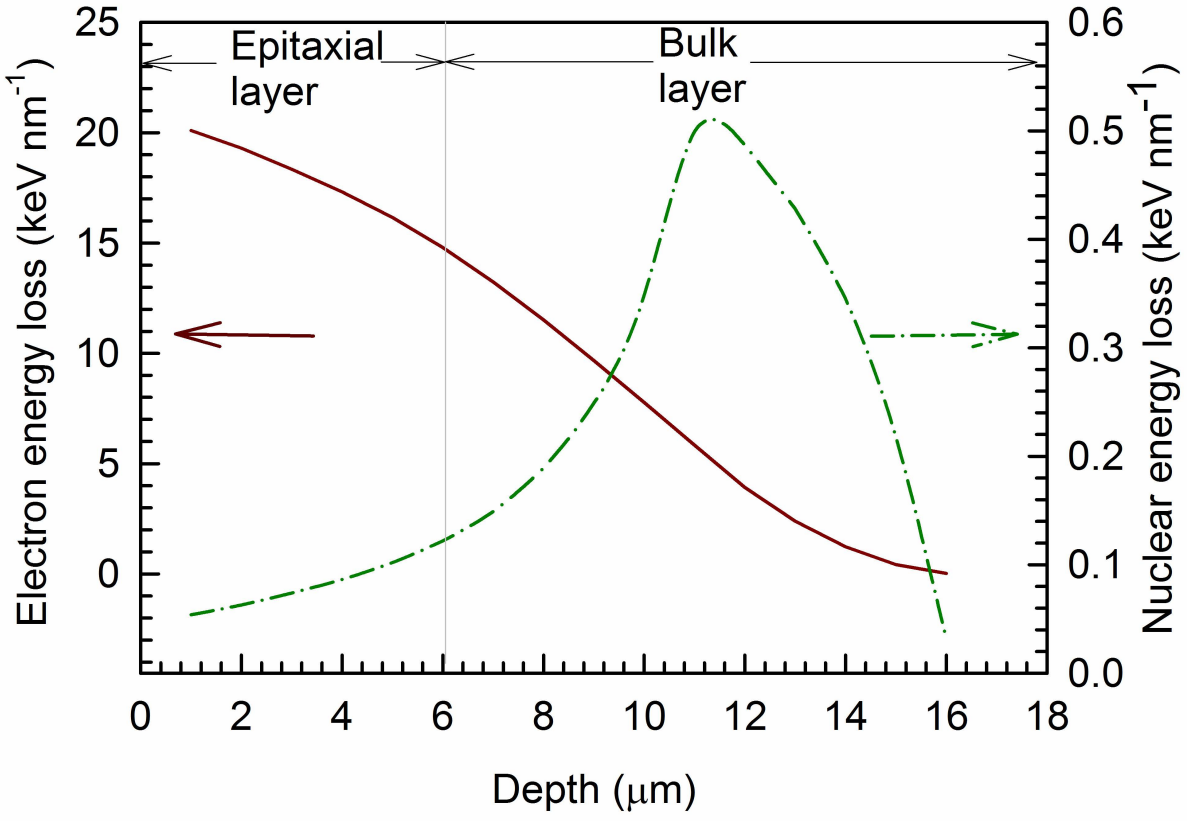

Figure 5.14: Predicted electron and nuclear energy loss with depth obtained from SRIM simulations on 4H-SiC at a fluence of 5×10^{11} cm^{-2} .

5.5.4 Confocal Raman microscopy

The vibrational modes both perpendicular and parallel to the c-axis have been discussed in section 2.8. Figure 5.15 shows the depth profile and the cluster spectrum associated with each layer of the un-irradiated wafer. The profile is consistent with the material specifications. The epitaxial layer is approximately 6.0 μm (brick red) and the bright red layer represents the bulk. The Longitudinal optical mode (LO) at 978 cm^{-1} has been attributed to free carrier (N-doping) interactions (Nakashima and Harima, 1997). However, the peak intensity ratios $I_{978} : I_{778}$ is constant for both layers at 0.38. This suggests that the difference in N-dopant concentration between layers has an overall effect on the whole material not on individual vibrational modes.

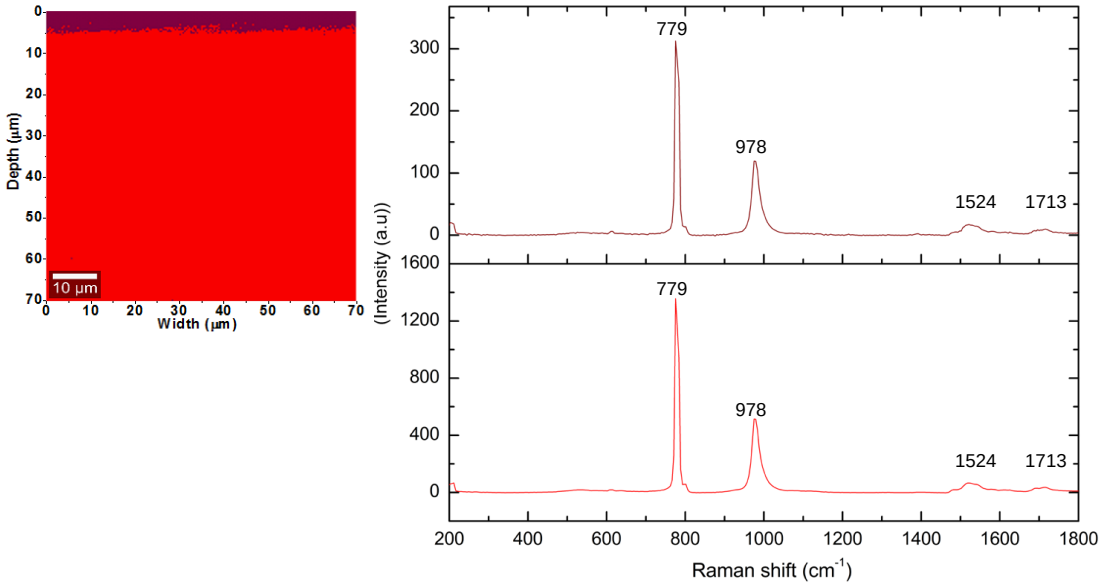

Figure 5.15: (top left) Depth profile of as-grown 4*H*-SiC obtained from cluster distributions showing an epitaxial layer (brick red), a bulk layer (red). The graphs show the cluster average Raman spectra which constitute the depth profile.

Table 5.5: Frequency in cm^{-1} and assignment for peaks for as-grown 4*H*-SiC.

Layer	Frequency (cm^{-1})	Mode	FWHM	Reference
Epitaxial	778	TO	11.3	(Sorieul *et al.*, 2006)
Epitaxial	978	LO	22.3	(Burton *et al.*, 1998)
Bulk layer	779	TO	10.2	(Nakashima and Harima, 1997)
Bulk layer	978	LO	21.4	(Burton *et al.*, 1998)

The longitudinal optical peak at 776 cm^{-1} is slightly more intense in the epitaxial layer. The observed peaks are listed in Table 5.5.

Figure 5.16 depicts a depth profile of the wafer after 167 MeV Xe irradiation and the associated cluster spectra. Three layers are displayed; a top layer (blue), thicker than the epitaxial layer, a medium layer (green) and the bulk layer (red). The top layer has a thickness of approximately 13 μm. This value is consistent with the maximum dpa predicted from SRIM simulations in Figure 5.14, hence the blue layer and average spectra represent the top part of the wafer with maximum damage induced by the incident radiation.

The highest background is observed on the blue spectrum with a peak like structure at 883 cm^{-1}. Increase in background is disorder-related, showing that the top layer had a relatively large amount of induced defects on the wafer. The second layer (green)

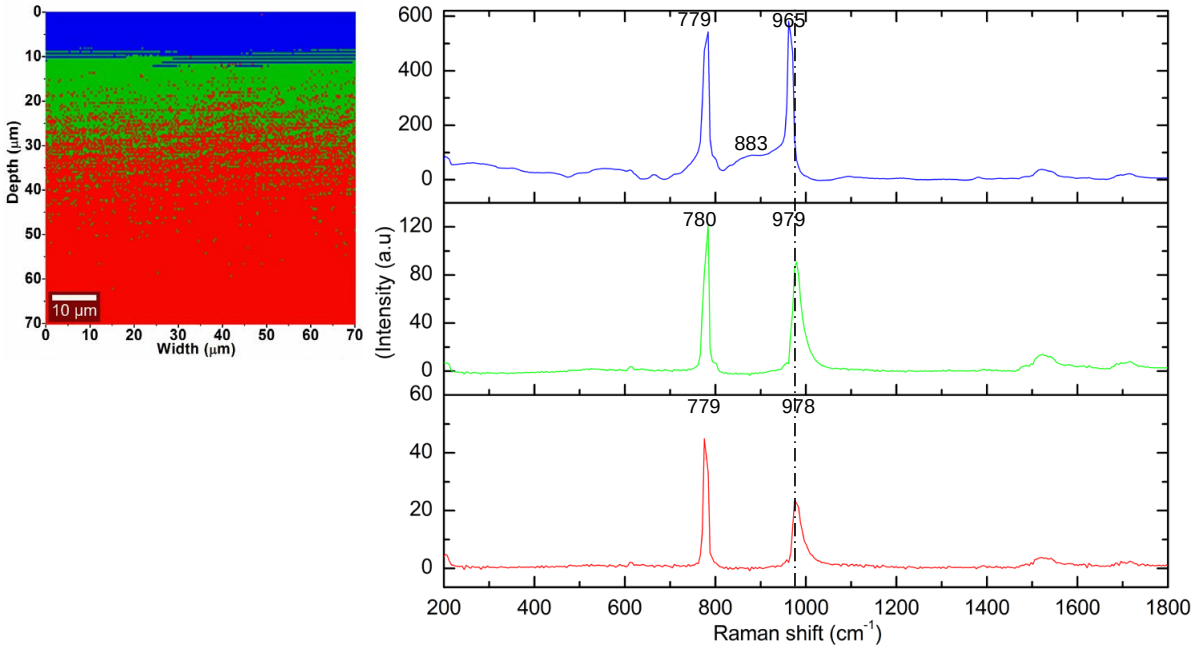

Figure 5.16: (top left) Depth profile of 167 MeV Xe irradiated 4H-SiC obtained from cluster distributions showing a damaged top layer (blue), a damaged bulk layer (green) and a pristine bulk layer (red). The graphs show the cluster average Raman spectra which constitute the depth profile.

does not have a uniform spectral distribution on the depth profile;and disorder is observed at a depth up to twice the projected range. This uneven damage, according to Malherbe (2013), can be attributed to a small population of displaced atoms recoiling through the lattice to produce other displacements resulting in a cascade effect and extended damage micro-regions. A similar result has also been observed by Hlatshwayo *et al.* (2016) after irradiating SiC with slow moving 167 MeV Xe ions. The SRIM projected range was 160 nm but damage was observed at 190 nm. The observed peaks are listed in Table 5.6

The red layer represents the bulk of the wafer which was not penetrated by the incident radiation.

A peak shift was observed on the longitudinal optical peak at 965 cm^{-1} on the different layers. Peak shifts have been associated with compressive stress in the c-plane due to lattice mismatch between layers. Jiang *et al.* (2016) have shown that stress results from interstitial type defects or clusters formed by the irradiation.

Raman intensities of the irradiated samples are lower than those of the pristine samples at the peaks. The peak intensity ratios I_{978} : I_{778} were 0.51, 0.75 and 1.08 for the three layers respectively, starting from the bottom. This can be attributed to

Table 5.6: Frequency in cm^{-1} and assignment for peaks for 167 MeV Xe irradiated epitaxial 4*H*-SiC.

Layer	Frequency (cm^{-1})	Mode	FWHM	Reference
Damaged Epitaxial	779	TO	14.5	(Sorieul *et al.*, 2006)
Damaged Epitaxial	996	LO	13.2	(Burton *et al.*, 1998)
Damaged Bulk	780	TO	13.5	(Nakashima and Harima, 1997)
Damaged Bulk	979	LO	21.7	(Burton *et al.*, 1998)
Pristine Bulk	779	TO	10.2	(Nakashima and Harima, 1997)
Pristine Bulk	978	LO	21.3	(Burton *et al.*, 1998)

carrier removal, a phenomenon which occurs due to irradiation induced defects capturing carriers. As a result a reduced intensity of the N-dopant related 978 cm^{-1} is observed. There is also a broadening of the TO peak as observed in the comparison of FWHM on Tables 5.6 and 5.5 which results from radiation damage . The pristine bulk layer spectrum is less intense on irradiated samples because the irradiation damage increases optical absorption centers which reduce the Raman signal as it passes the top layers.

When the samples are exposed to incident Xe radiation, ion solid interactions result in point defect build-up due to lattice distortions. Ballistic processes result in damage cascades with vacancies trapping gas particles and creation of interstitial defects (Jiang *et al.*, 2016). The spectra confirmed modifications of the crystal structure consistent with degradation without armophization. A relatively low fluence was used therefore the bond structure and lattice order is preserved and the electronic structure has minor perturbations (Sorieul *et al.*, 2012).

The decreases in intensity after irradiation, is attributed the breaking of bonds and changes in the lattice arrangement. Loss in Raman signal has been correlated to optical absorption in the damaged layer by point defects created in the band gap (Sorieul *et al.*, 2012).

A comparison of the depth profile from irradiated samples shows that the result is consistent with what was predicted by the SRIM simulations. Maximum density of Xe ions is observed at around 13 μm where nuclear energy loss is at its maximum. This shows that confocal Raman depth profiles can give results comparable to those obtained by the more established, accepted methods like SRIM simulations, regarding the distribution of defects in the lattice structure. Similar observations were reported by (Huang *et al.*, 2017).

5.5.5 AFM

Figure 5.17 depicts the morphology of 4H-SiC obtained in ScanAsyst mode. Figure 5.17 a) shows pristine and Figure 5.17 b) shows irradiated 4H-SiC. It is clear that the irradiated material has elongated protrusions on the surface in the direction of the incident irradiation. Compositional analysis on these structures using energy dispersive X-ray analysis (EDS) showed that they were purely Si and C and were not emanating from any contamination of the samples. Ochedowski *et al.* (2014) also irradiated 6H-SiC with 81 MeV Ta^{24+} and 117 MeV Pb^{31+} at angles of incidence varying from 0.6° – 1.1°. They observed narrow graphitic grooves and speculated that they emanated from the sublimation of silicon atoms in the SiC matrix by incident ions. Their differences with Figure 5.17 can be due to the lower energy they used and may also be because they did not use inert elements. From the AFM micrographs the areal density of the protrusions with ion dose is not direct. This discrepancy and the origin of these protrusions is still under investigation.

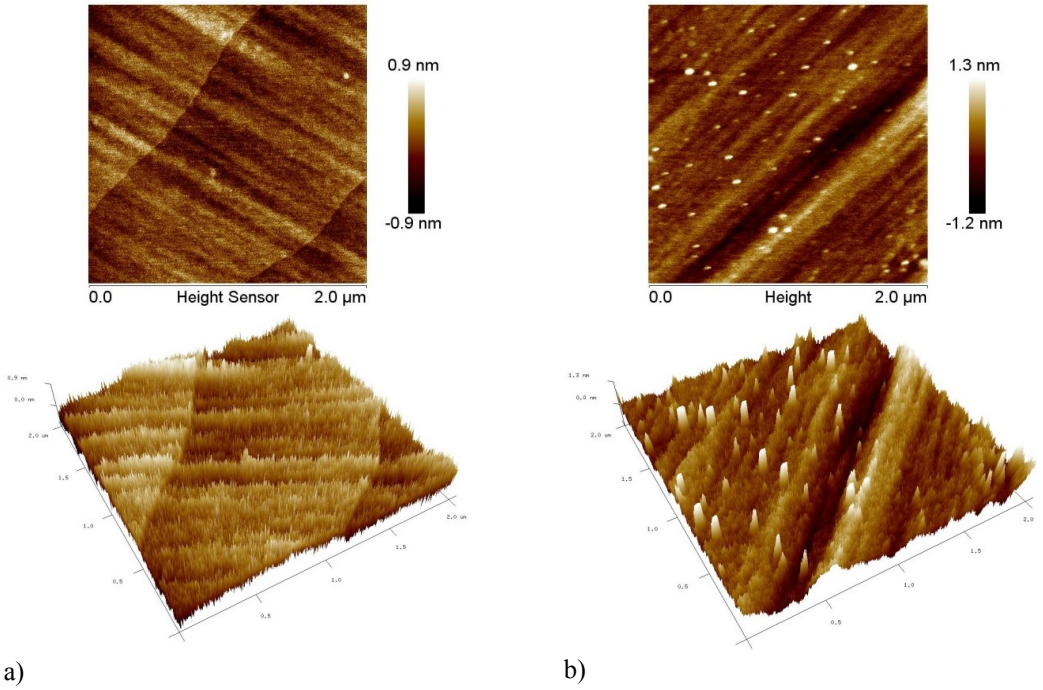

Figure 5.17: 2 μm × 2 μm AFM 2D and 3D images for a)pristine 4H-SiC and b) 167 MeV Xe irradiated 4H-SiC

5.5.6 DLTS

Figure 5.18 shows the DLTS spectra obtained using the 50 s^{-1} rate window. Curve (a) is the control spectrum obtained from un-irradiated samples and curve (b) is from samples irradiated by the Xe^{26+} ions. From curve (b) we notice that Xe irradiation introduced two electron traps $E_{0.40}$ and $E_{0.69}$ in addition to the native ones. A similar observation was made by Kalinina *et al.* (2002) in Kr irradiated 4*H*-SiC. The defect signatures (activation energy E_a and capture cross section (σ_n)) were determined from the slope and intercept of Arrhenius plots in Figure 5.19.

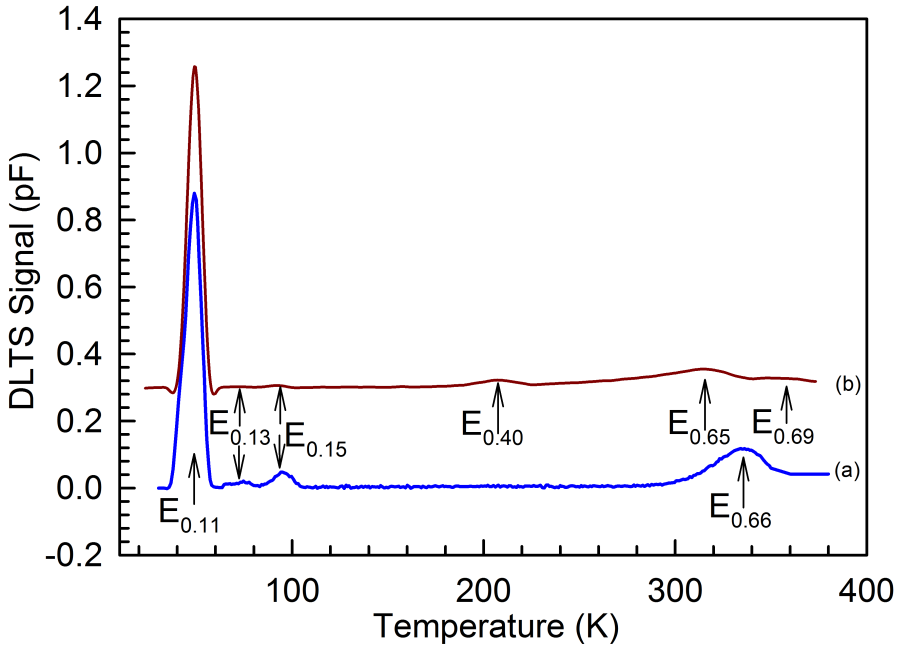

Figure 5.18: DLTS spectra of (a) as deposited Ni/4*H*-SiC Schotky barrier diodes. (b) Ni/4*H*-SiC Schottky barrier diodes on 167 MeV Xe^{26+} irradiated 4*H*-SiC. The spectra were recorded using a quiescent reverse bias of -5 V, filling pulse 1 V, pulse width of 2 ms

The $E_{0.69}$ donor level of the Z_1 center and the $E_{0.40}$ acceptor level of the Z_2 center defects have also been observed in n-4*H*-SiC after irradiation by radionuclides and after the electron beam metalization processes (Paradzah *et al.*, 2015; Omotoso *et al.*, 2016). As a result none of the electrically active defect states can be directly attributed specifically to Xe interactions with silicon carbide. The V_{Si} is realised in the $E_{0.69}$ defect. From the Raman spectroscopy results and the SRIM it is clear that the Xe penetrated deep into the lattice structure introducing defects. These defects have already been discussed in the sputter deposition section.

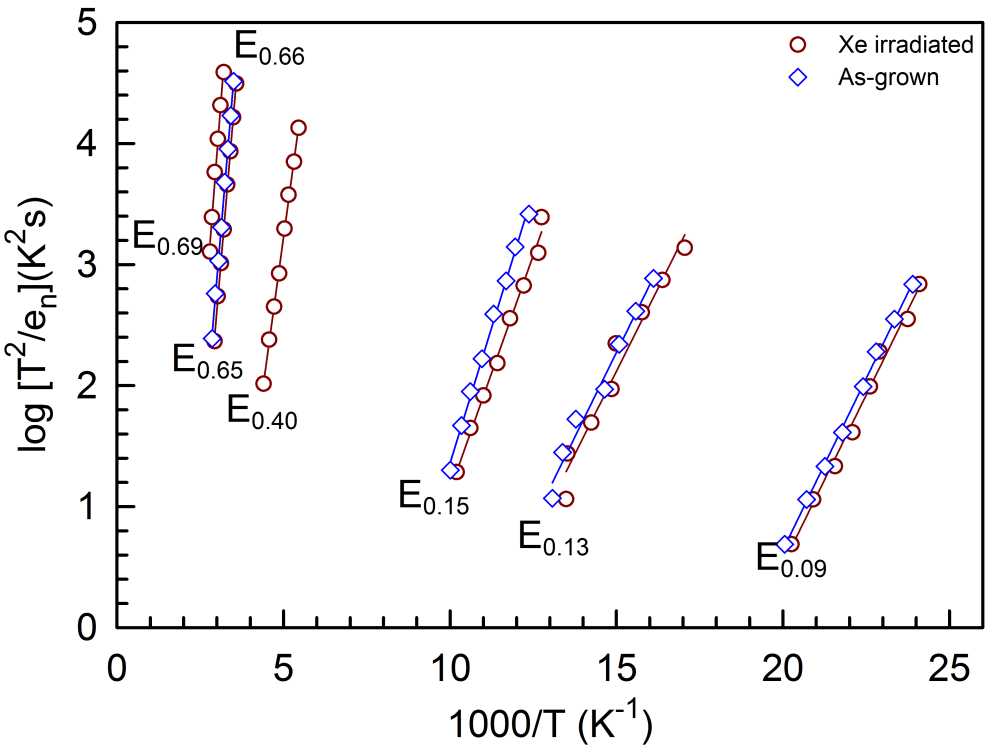

Figure 5.19: Arrhenius plots of defects in resistively evaporated Ni/4*H*-SiC Schottky barrier diodes on as-grown and 167 MeV Xe ion irradiated 4*H*-SiC

The Arrhenius plots (Figure 5.19) show that the heavy ion irradiation impacts the native defects and results in a shift in their signatures. Overall the results confirmed the radiation hardness of 4*H*-SiC, as they showed that despite swift heavy ion irradiation, the material remained intact both structurally and electronically.

5.5.7 Concluding remarks

n-4*H*-SiC was irradiated with 167 MeV Xe^{26+} ions at room temperature. From Raman spectroscopy depth profiles it was observed that the damage was moderate and the integrity of the lattice structure was conserved. Confocal Raman spectroscopy was successfully used for depth profiling. The depth profiles were consistent with SRIM predictions. AFM showed that elongated protrusions were introduced on the surface. DLTS results showed that the swift heavy ions induced the $E_{0.69}$ donor level of the Z_2 center and the $E_{0.40}$ acceptor level of the Z_1 center.

Chapter 6

Conclusions

6.1 Introduction

The research contained in this dissertation is an excerpt of the investigations done on the defect characteristics of n-4H-SiC. Characterization of defects introduced through various processing techniques was succesfully achieved. A V_{Si} related defect was induced through sputter deposition and swift heavy ion irradiation. In this chapter conclusions specific to each section in chapter 5 are summarized.

6.1.1 Sputter deposition

The study showed that sputter deposition as a metalization technique has a profound effect on the electrical characteristics of 4H-SiC based devices. The influence of the defects induced by the technique resulted in devices with poorer diode characteristics compared to those fabricated by resistive evaporation. From the results it was deduced that the plasma and incident metal particles induced the $E_{0.39}$, a unique defect observed after sputter deposition and the $E_{0.69}$ which is related to the silicon vacancy (V_{Si}). It was inferred that sputter deposition induces the V_{Si} which after thermal treatment has been employed as a single photon source with potential applications in quantum computation. The technique is therefore recommended for both metalization and to induce beneficial defects

6.1.2 Annealing

Once the V_{Si} defect was induced by sputtering, thermal treatment was carried out to transform it into the $C_{Si}V_C$. Annealing the W/4*H*-SiC interface resulted in a significant degradation of diode *I-V* and *C-V* characteristics. DLTS was successfully used to track defects associated with the diffusion of W into the 4*H*-SiC lattice structure. Owing to the sensitivity of L-DLTS the diffusion was detected at a lower temperature when compared to what had been reported from ToF-SIMS and other techniques used in past studies. From the depth profiles, the diffusion rate was calculated as 6 $\times 10^{-10}$ μm s^{-1} at 1100 °C. It was concluded that exposure of W/4*H*-SiC contacts to temperatures above 800 °C, during operation or thermal treatment may result in the migration of interfacial reaction products into the semiconductor wafer, contaminating the devices in the process, despite strict cleanliness practice during fabrication. The resulting phase compositions and defects significantly affect the device's electrical characteristics. Laplace DLTS accurately tracked diffusion of defects and detected them earlier than other experimental methods.L-DLTS was only successfully used after annealing at high temperatures to reduce the spectral baseline on conventional DLTS scans.

6.1.3 Swift heavy ion irradiation

Swift heavy Xe^{+26} were considered for inducing the silicon vacancy. Xe is inert therefore it would not react with the silicon carbide to cause contamination. Irradiating n-type 4*H*-SiC with swift heavy Xe^{+26} ions at room temperature resulted in moderate to low damage one week later. This confirmed the radiation hardness of 4*H*-SiC and its potential use in high radiation environments. From the Raman spectroscopy it was observed that the damage was moderate and the lattice structure was conserved. This was despite a SRIM maximum depth of ion penetration at 13.02 μm below the surface of 4*H*-SiC.

Ni Schottky barrier diodes were fabricated on swift heavy ion irradiated epitaxial layers and characterized with DLTS. DLTS results on Ni/4*H*-SiC Schottky barrier diodes were consistent with other swift heavy ions such as Kr, inducing the $E_{0.69}$ donor level of the Z_2 center and the $E_{0.40}$ acceptor level of the Z_1 center. There was also a considerable increase in defect concentration after irradiation accompanied by a decrease in Raman intensity. Confocal Raman spectroscopy was successfully used for depth profiling of the structure of the wafers after irradiation. Its accuracy was consistent with SRIM simulations.

6.2 Future work

Several defect states were reported within this thesis. However, the chemical identity and microscopic structure of most of them remain uncertain due to the limitations of DLTS and L-DLTS. It is therefore necessary to adopt other defect identification techniques like photoluminescence, electron paramagnetic resonance (EPR), transmissionelectron microscopy (TEM) Hall effect measurements and controlled chemical treatments in a bid to understand the nature of these defects. TEM not only shows defects but gives their quantitative properties e.g. strain fields.

The irradiation experiments were done at room temperature where the vacancies and interstitials are mobile. A study of the first generation defects has to be carried out. This is achievable by irradiation at very low temperatures. It is also essential to relook at the fine structure of defects introduced by other incident ion types in $4H$-SiC that were reported in the past using conventional DLTS.

Furthermore, RBS wil be done to verify diffusion of defects after annealing W/$4H$-SiC as observed using L-DLTS.

Finally, all the experimental work that has been carried out can be extended to include p-type $4H$-SiC, n-type $4H$-SiC of different free carrier densities and $4H$-SiC grown using different techniques like molecular beam epitaxy (MBE). Generally MBE produces purer semiconductors.

Bibliography

Archilla J. F. R., Coelho S. M. M., Auret F. D., Nyamhere C., Dubinko V. I., and Hizhnyakov V. Experimental observation of intrinsic localized modes in germanium. *Quodons in mica*, pages 343–362. Springer, 2015.

Asghar M., Hussain I., Noor H. S., Iqbal F., Wahab Q., and Bhatti A. S. Properties of dominant electron trap center in n-type SiC epilayers by means of deep level transient spectroscopy. *Journal of applied physics*, 101(7):073706, 2007.

Auret F. D. and Deenapanray P. N. Deep level transient spectroscopy of defects in high-energy light-particle irradiated Si. *Critical reviews in solid state and materials sciences*, 29(1):1–44, 2004.

Auret F. D., Goodman S. A., Leclerc Y., Myburg G. and Schutte C. Electronic properties of defects introduced in GaAs during sputter deposition of gold Schottky contacts. *Materials science and technology*, 13(11):945–948, 1997.

Auret F. D., Meyer W. E., Goodman S. A., Koschnick F. K., Spaeth J.-M., Beaumont B. and Gibart P. Metastable-like behaviour of a sputter deposition-induced electron trap in n-GaN. *Physica B: Condensed matter*, 273:92–95, 1999.

Baca A. G. and Ashby C. I. *Fabrication of GaAs devices*. Number 6. IET, 2005., ISBN 9780863413537

Benton J. L. Characterization of defects in semiconductors by deep level transient spectroscopy. *Journal of crystal growth*, 106(1):116 – 126, 1990.

Bergman J. P., Lendenmann H., Nilsson P. A., Lindefelt U., Skytt P., *et al* . Crystal defects as source of anomalous forward voltage increase of 4H-SiC diodes. In *Materials science forum,* 353, 299–302, 2001.

Berthou M., Godignon P., Montserrat J., Millan J., and Planson D. Study of 4H-SiC JBS diodes fabricated with tungsten schottky barrier. *Journal of electronic materials*, 40(12):2355, 2011.

Biderman N., Sundaramoorthy R., Haldar P. and Lloyd J. Dissociative diffusion mechanism in vacancy-rich materials according to mass action kinetics. *AIP advances,* 6(5):055211, 2016.

Blood P. and Orton J. W. The electrical characterisation of semiconductors. *Reports on progress in physics*, 41(2):157, 1978.

Blood P. and Orton J. W. *The electrical characterization of semiconductors: majority carriers and electron states*. Academic Press, 1992. ISBN 9780125286275.

Bockstedte M., Mattausch A., and Pankratov O. *Ab initio* study of the annealing of vacancies and interstitials in cubic SiC: Vacancy-interstitial recombination and aggregation of carbon interstitials. *Physical review. B*, 69:235202, 2004.

Bourgoin J. *Point defects in semiconductors II: Experimental aspects*. Springer series in solid-state sciences. Springer, 2012. ISBN 9783642818325.

Bracht H., Stolwijk N. A., Laube M. and Pensl G. Diffusion of boron in silicon carbide: Evidence for the kick-out mechanism. *Applied physics letters*, 77(20):3188–3190, 2000.

Brillson L. *Surfaces and interfaces of electronic materials*. Wiley - IEEE. Wiley, 2012. ISBN 9783527665723.

Burton J. C., Sun L., Pophristic M., Lukacs S. J., Long F. H., Feng Z. C. and Ferguson I. T. Spatial characterization of doped SiC wafers by Raman spectroscopy. *Journal of applied physics*, 84(11):6268–6273, 1998.

Castelletto S., Johnson B. C., Iv´ady V., Stavrias N., Umeda T., Gali A. and Ohshima T. A silicon carbide room-temperature single-photon source. *Nature materials*, 13(2):151, 2014.

Castelletto S., Rosa L. and Johnson B. C. Silicon carbide for novel quantum technology devices. *Advanced silicon carbide devices and processing*. InTech, 2015. ISBN 9789535121688.

Choyke ,W., Matsunami ,H., and Pensl ,G. *Silicon carbide: Recent major advances*. Advanced texts in physics. Springer, 2003. ISBN 9783540404583.

Claeys ,C. and Simoen ,E. *Radiation effects in advanced semiconductor materials and devices*, 57. Springer Science & Business Media, 2013. ISBN 9783662049747.

Claeys C. and Simoen E. GaAs based field effect transistors for radiation-hard applications. *Radiation effects in advanced semiconductor materials and devices,* 245–280. Springer, 2002. ISBN 9783540433934

Coelho S. M. M., Auret F. D., Janse van Rensburg P. J. and Nel J. M. Electrical characterization of defects introduced in n-Ge during electron beam deposition or exposure. *Journal of applied physics*, 114(17):173708, 2013.

Crawford ,J. and Slifkin ,L. *Point defects in solids: General and ionic crystals*. Springer US, 2013. ISBN 9781468429701

Crofton J. and Sriram S. Reverse leakage current calculations for SiC Schottky contacts*, IEEE Transactions on electron Devices*, 43(12):2305–2307, 1996.

Cullity B. D. and Stock S. R. *Elements of X-ray diffraction*. Pearson Education, 2014. ISBN 9781292040547

Dalibor T., Pensl G., Nordell N., and Sch¨oner A. Electrical properties of the titanium acceptor in silicon carbide. *Physical review B*, 55(20):13618, 1997.

Dalibor T., Pensl G., Yamamoto T., Kimoto T., Matsunami H., Sridhara S. G., Nizhner D. G., Devaty R. P. and Choyke W. J. Oxygen-related defect centers in 4H-silicon carbide. *Materials science forum,* 264, 553–556. Trans Tech Publ, 1998.

Danno ,K. and Kimoto ,T. Deep level transient spectroscopy on as-grown and electron-irradiated p-type 4H-SiC epilayers. *Journal of applied physics*, 101(10): 103704, 2007.

Darken ,L. S. Diffusion, mobility and their interrelation through free energy in binary metallic systems. *Transactions of the american institute of mining, metalurgical and petroleum engineers*, 175:184–201, 1948.

de Luca A., Portavoce A., Texier M., Grosjean C., Burle N., Oison V. and Pichaud B. Tungsten diffusion in silicon. *Journal of Applied Physics*, 115(1):013501, 2014.

Debelle A., Backman M., Thome L., Weber W. J., Toulemonde M., Mylonas S., Boulle A., Pakarinen O. H., Juslin N., Djurabekova F. *et al.* Combined experimental and computational study of the recrystallization process induced by electronic interactions of swift heavy ions with silicon carbide crystals. *Physical review B*, 86(10):100102, 2012.

Dobaczewski L., Kaczor P., Hawkins I. D. and Peaker A. R. Laplace transform deep-level transient spectroscopic studies of defects in semiconductors. *Journal of applied physics*, 76(1):194–198, 1994.

Dobaczewski L., Peaker A. R. and Bonde Nielsen ,K. Laplace-transform deep level spectroscopy: The technique and its applications to the study of point defects in semiconductors. *Journal of applied physics*, 96(9):4689–4728, 2004.

Doyle J. P., Linnarsson M. K., Pellegrino P., Keskitalo N. Svensson B. G., Sch¨oner A., Nordell ,N. and Lindstr¨om ,J. L. Electrically active point defects in n-type 4H-SiC. *Journal of Applied Physics*, 84(3):1354–1357, 1998.

Dunwoody H. C. Wireless-telegraph system., December 4 1906. US Patent 837,616.

Eberlein T. A. G., Jones R., and Briddon P. R. z_1/z_2 defects in $4H-$SiC. *Physical Review. Letters.*, 90:225502, 2003.

Eiche C., Maier D., Schneider M., Sinerius D., Weese J., Benz K. W. and Honerkamp J. Analysis of photoinduced current transient spectroscopy (PICTS) data by a regularization method. *Journal of physics: Condensed matter*, 4(28):6131, 1992.

Enderlein R. and Horing ,N. *Fundamentals of semiconductor physics and devices*. World Scientific, 1997. ISBN 9789810223878.

Fan J. and Chu P. K. General properties of bulk SiC. *Silicon carbide nanostructures*, pages 7–114. Springer, 2014. ISBN 9783319087269.

Feng Z. *Handbook of solid-state lighting and LEDs*. Series in Optics and Optoelectronics. CRC Press, 2017. ISBN 9781351647649.

Fraga M. A., Bosi M. and Negri ,M. Silicon carbide in microsystem technology-thin film versus bulk material. *Advanced silicon carbide devices and processing*. InTech, 2015. ISBN 9789535121688.

Gao F., Chen N., Hernandez-Rivera E., Huang D. and LeVan P. D. Displacement damage and predicted non-ionizing energy loss in GaAs. *Journal of applied physics*, 121(9):095104, 2017.

Giridhar ,G., Manepalli ,R., and Apparao ,G. Confocal raman spectroscopy. *Spectroscopic methods for nanomaterials characterization*, 141–161. Elsevier, 2017.

Gou L., Qi C., Ran J., and Zheng C. SiC film deposition by DC magnetron sputtering. *Thin solid films*, 345(1):42–44, 1999.

Grundmann M. *The physics of semiconductors: An introduction including devices and nanophysics*. Springer Science and Business Media, 2006. ISBN 9783642138843

Guinier A. *X-Ray diffraction: Crystals, imperfect crystals, and amorphous bodies*. Dover Books on Physics. Dover Publications, 2013. ISBN 9780486141343.

Hemmingsson C., Son N. T., Kordina O., Bergman J. P., Janz´en E., Lindstr¨om J. L., Savage S., and Nordell N. Deep level defects in electron-irradiated 4H-SiC epitaxial layers. *Journal of applied physics,* 81(9):6155–6159, 1997.

Hemmingsson C. G., Son N. T., Ellison A., Zhang J., and Janz´en E. Negative-U centers in 4H-SiC. *Physical review B*, 58:R10119–R10122, 1998.

Hlatshwayo T. T., O'Connell J. H., Skuratov V. A., Wendler E., Njoroge E. G., Mlambo M., and Malherbe J. B. Comparative study of the effect of swift heavy ion irradiation at 500 ºC and annealing at 500 ºC on implanted silicon carbide. *RSC Advances*, 6(73):68593–68598, 2016.

Huang K., Jia Q., You T., Zhang S., Lin J., Zhang R., Zhou M., Yu W., Zhang B., Ou X., and *et al* . Defect formation in MeV H^+ implanted GaN and 4H-SiC investigated by cross-sectional Raman spectroscopy. *Nuclear instruments and methods in physics research section B: Beam interactions with materials and atoms,* 406:656–661, 2017.

Huang L. and Wang D. Barrier inhomogeneities and electronic transport of Pt contacts to relatively highly doped n-type 4H-SiC. *Journal of applied physics*, 117 (20):204503, 2015.

Hundhausen M., Psche R., Rhrl J. and Ley L. Characterization of defects in silicon carbide by raman spectroscopy. *physica status solidi (b)*, 245(7):1356–1368, 2008.

Jayant B. B. *Silicon carbide power devices*. World scientific, 2006. ISBN 9789814478946.

Jiang C., Nicola¨ı J., Decl´emy A., Gilabert E., Beaufort M.-F.,and Barbot J.-F. Implantation damage in heavy gas implanted 4H-SiC. *Nuclear instruments and methods in physics research Section B: Beam interactions with materials and atoms,* 374:71–75, 2016.

Jimenez J. and Tomm J. *Spectroscopic Analysis of Optoelectronic Semiconductors*. Springer Series in Optical Sciences. Springer International Publishing, 2016. ISBN 9783319423494.

Jovanovic M. M. and Jang Y. State-of-the-art, single-phase, active power-factor-correction techniques for high-power applications-an overview. *IEEE transactions on industrial electronics*, 52(3):701–708, 2005.

Kakanakova-Georgieva A., Marinova T., Noblanc O., Arnodo C., Cassette S. and Brylinski C. XPS characterization of tungsten-based contact layers on 4H–SiC. *Thin solid films*, 337(1-2):180–183, 1999.

Kalinina E., Onushkin G., Davidov D., Hallen A., Konstantinov A., Skuratov V. A. and Stano J. Electrical study of 4H-SiC irradiated with swift heavy ions. , *SIMC-XII-2002. 12th International conference on semiconducting and insulating materials*, pages 106–109. IEEE, 2002.

Kalinina E. V., Lebedev A. A., Bogdanova E., Berenquier B., Ottaviani L., Violina ,G. N. and Skuratov V. A. Irradiation of 4H-SiC UV detectors with heavy ions. *Semiconductors*, 49(4):540–546, 2015.

Kamata I., Tsuchida H., Jikimoto T., and Izumi K. Structural transformation of screw dislocations via thick 4H-SiC epitaxial growth. *Japanese journal of applied physics*, 39(12R):6496, 2000.

Karatas S. and Altndal S. Temperature dependence of barrier heights of Au/n-type GaAs Schottky diodes. *Solid-state electronics*, 49(6):1052 – 1054, 2005.

Kawasuso A., Redmann F., Krause-Rehberg R., Weidner M., Frank T., Pensl G., Sperr P., Triftsh¨auser W. and Itoh H. Annealing behavior of vacancies and Z 1/2 levels in electron-irradiated 4H–SiC studied by positron annihilation and deep-level transient spectroscopy. *Applied physics letters*, 79(24):3950–3952, 2001.

Kim S.-H., Shim G.-I., and Choi S.-Y. Fabrication of Nb-doped ZnO nanowall structure by RF magnetron sputter for enhanced gas-sensing properties. *Journal of alloys and compounds*, 698:77–86, 2017.

Kimoto T. and Cooper J. A. *Fundamentals of silicon carbide technology: Growth, characterization, devices and applications.* John Wiley & Sons, 2014. ISBN 9781118313527.

Kimoto T., Miyamoto N., and Matsunami H. Performance limiting surface defects in SiC epitaxial pn junction diodes. *IEEE Transactions on electron devices*, 46(3): 471–477, 1999.

Kuchuk A., Kladko V., Guziewicz M., Piotrowska A., Minikayev R., Stonert A., and Ratajczak R. Fabrication and characterization of nickel silicide ohmic contacts to n-type 4H–silicon carbide.*Journal of physics: Conference series*, 100, page 042003. IOP Publishing, 2008.

Lamichhane R. R., Ericsson N., Frank S., Britton C., Marlino L., Mantooth A., Francis M., Shepherd P., Glover M., Perez S., and *et al* . A wide bandgap silicon carbide (SiC) gate driver for high-temperature and high-voltage applications. *, 2014 IEEE 26th International Symposium on* Power Semiconductor Devices & IC's (ISPSD), 414–417. IEEE, 2014.

Lang D. V. Deeplevel transient spectroscopy: A new method to characterize traps in semiconductors. *Journal of applied physics*, 45(7):3023–3032, 1974.

Larkin P. *Infrared and raman spectroscopy: Principles and spectral interpretation*. Elsevier Science, 2017. ISBN 9780128042090.

Laskar A., Bocquet J., Br´ebec G., and Monty C. *Diffusion in materials*. Nato science series E:. Springer, 2012. ISBN 9789400919761.

Li S. *Semiconductor physical electronics*. Microdevices. Springer US, 2012. ISBN 9781461304890

Li Z. and Wang Q. Molecular dynamics simulation of coulomb explosion in SiC. *Progress report on nuclear science and technology in China (Vol. 3). Proceedings of academic annual meeting of China Nuclear Society in 2013, No. 4–nuclear material sub-volume*, 2014.

Lindhard J., Scharff M. and Schiott H. K. danske vidensk selskab., mat. *Fys Medd*, 31:1, 1963.

Lohrmann A., Castelletto S., Klein J., Ohshima T., Bosi M., Negri M., Lau D., Gibson B., Prawer S., McCallum J., *et al* . Activation and control of visible single defects in 4H-, 6H-, and 3C-SiC by oxidation. *Applied physics letters*, 108(2): 021107, 2016.

Løvlie L. S. and Svensson B. G. Enhanced annealing of implantation-induced defects in 4H-SiC by thermal oxidation. *Applied physics letters*, 98(5):052108, 2011.

Lundberg N., ¨Otling M., T¨agtstr¨om P., and Jansson U. Chemical vapor deposition of tungsten schottky diodes to 6H-SiC. *Journal of the electrochemical society*, 143 (5):1662–1667, 1996.

Madhusoodhanan S., Bhattacharya S. and Hatua K. Control technique for 15 kV SiC IGBT based active front end converter of a 13.8 kV grid tied 100 kVA transformerless intelligent power substation. *Energy Conversion Congress and Exposition (ECCE), 2013 IEEE*, pages 4697–4704. IEEE, 2013.

Malherbe J. B. Diffusion of fission products and r adiation damage in SiC. *Journal of physics D: Applied physics*, 46(47):473001, 2013.

Mehrer H. *Diffusion in solids: Fundamentals, methods, materials, diffusion-controlled processes*. Springer series in solid-state sciences. Springer, 2007. ISBN 9783540714880.

Mikelsen M., Grossner U., Bleka J. H., Monakhov E. V., Svensson B. G., Yakimova R., Henry A., Janz´en E. and Lebedev A. A. Carrier removal in electron irradiated 4H and 6H SiC. *Materials science forum*, 600, 425–428. Trans Tech Publ, 2009.

Mishra U. and Singh J. *Semiconductor device physics and design*. Springer Netherlands, 2007. ISBN 9781402064814.

M¨onch W. *Electronic properties of semiconductor interfaces*. Springer Series in Surface Sciences. Springer, 2013. ISBN 9783662069455.

Nakamura D., Gunjishima I., Yamaguchi S., Ito T., Okamoto A., Kondo H., Onda ,S., and Takatori K. Ultra high-quality silicon carbide single crystals. *Nature*, 430 (7003):1009, 2004.

Nakashima S.-i. and Harima H. Raman investigation of SiC polytypes. *physica status solidi (a)*, 162(1):39–64, 1997.

Nappi E. and Seguinot J. *Innovative detectors for supercolliders: Proceedings of the 42nd workshop of the INFN ELOISATRON project, Erice, Italy, 28 Sept - 4 Oct 2003*. Science and culture series (Singapore).: Physics. World Scientific, 2004. ISBN 9789812387455.

Neamen D. A. *Semiconductor physics and devices*. McGraw-Hill, 2012. ISBN 9780071070102.

O ˜Connell J., Skuratov V., Sohatsky A., and Neethling J. 1.2 MeV/amu Xe ion induced damage recovery in SiC. *Nuclear instruments and methods in physics research section B: Beam interactions with materials and atoms*, 326:337–340, 2014.

Ochedowski O., Osmani O., Schade M., Bussmann B. K., Ban-dEtat B., Lebius H., and Schleberger M. Graphitic nanostripes in silicon carbide surfaces created by swift heavy ion irradiation. *Nature communications*, 5:3913, 2014.

Omotoso E., Meyer W. E., Auret F. D., Paradzah A. T., Diale M., Coelho S. M. M., and van Rensburg P. J. J. The influence of high energy electron irradiation on the Schottky barrier height and the Richardson constant of Ni/4H-SiC Schottky diodes. *Materials science in semiconductor processing*, 39:112–118, 2015.

Omotoso E., Meyer W. E., Coelho S. M. M., Diale M., Ngoepe P. N. M. and Auret F. D. Electrical characterization of defects introduced during electron beam deposition of W Schottky contacts on n-type 4H-SiC. *Materials science in Semiconductor Processing*, 51:20–24, 2016.

Paradzah A. T., Auret F. D., Legodi M. J., Omotoso E. and Diale M. Electrical characterization of 5.4 MeV alpha-particle irradiated 4H-SiC with low doping density. *Nuclear instruments and methods in physics research section B: Beam interactions with materials and atoms*, 358:112–116, 2015.

Park J., Kim K., Park Y., Kim M., Lee H., Jun C., Koo S. and Ko S. Surface Al doping of 4H-SiC via low temperature annealing. *Applied physics letters*, 109(3): 031603, 2016.

Paul A. and Divinski S. *Handbook of solid st ate di ffusion: Diffusion fundamentals and techniques*. Elsevier Science, 2017. ISBN 9780128043608.

Paul A., Laurila T., Vuorinen V. and Divinski S. V. *Thermodynamics, diffusion and the Kirkendall effect in solids*. Springer, 2014. ISBN 9783319074603.

Peaker A., Markevich V., Hawkins I., Hamilton B., Nielsen K. B. and Gociski K. Laplace deep level transient spectroscopy: Embodiment and evolution. *Physica B: Condensed matter*, 407(15):3026 – 3030, 2012. 26th International Conference on Defects in Semiconductors.

Perevostchikov ,V. and Skoupov ,V. *Gettering defects in semiconductors*. Advanced microelectronics. Springer, 2005. ISBN 9783540262442.

Pierce ,G. WCrystal rectifiers for electric currents and electric oscillations. Part i. carborundum. *Physical review (Series I)*, 25(1):31, 1907.

Pintilie I., Pintilie L., Irmscher K., and Thomas B. Formation of the Z_1/Z_2 deep-level defects in 4H-SiC epitaxial layers: Evidence for nitrogen participation. *Applied physics letters*, 81(25):4841–4843, 2002.

Poole J. and Charles P. *Encyclopedic dictionary of condensed matter physics*. Academic Press, 2004. ISBN 9780080545233.

Queisser H., Spaeth J., and Overhof H. *Point Defects in semiconductors and insulators: Determination of atomic and electronic structure from paramagnetic hyperfine interactions*. Springer Series in Materials Science. Springer Berlin Heidelberg, 2003. ISBN 9783540426950.

Rahimo M., Canales F., Minamisawa R. A., Papadopoulos C., Vemulapati U., Mihaila A., Kicin S. and Drofenik U. Characterization of a silicon IGBT and silicon carbide MOSFET cross-switch hybrid. *IEEE Transactions on power electronics*, 30(9): 4638–4642, 2015.

Roccaforte F., La Via F., Raineri V., Pierobon R., and Zanoni E. Richardsons constant in inhomogeneous silicon carbide schottky contacts. *Journal of applied Physics*, 93(11):9137–9144, 2003.

Rogowski J. and Kubiak A. Time-of-flight SIMS depth profiling and imaging of the interface of al contact to n-type 4H silicon carbide. *Surface and interface analysis*, 45(1):381–385, 2013.

Rogowski J. and Kubiak A. Effects of annealing temperature on the structure and electrical properties of tungsten contacts to n-type silicon carbide. *Materials science and engineering: B*, 191:57–65, 2015.

Ryoken H., Sakaguchi I., Ohashi N., Sekiguchi T., Hishita S. and Haneda H. Non-equilibrium defects in aluminum-doped zinc oxide thin films grown with a pulsed laser deposition method. *Journal of materials research*, 20(10):28662872, 2005.

Saddow S. and Agarwal A. *Advances in silicon carbide processing and applications*. Artech House semiconductor materials and devices library. Artech House, 2004. ISBN 9781580537414.

Schroder D. K. *Semiconductor material and device characterization*. Wiley, 2006.

ISBN 9780471749080.

Seebauer E. G. and Noh K. W. Trends in semiconductor defect engineering at the nanoscale. *Materials science and engineering: R: Reports*, 70(3-6):151–168, 2010.

Seebauer E. and Kratzer M. *Charged semiconductor defects: Structure, thermodynamics and diffusion*. Engineering Materials and Processes. Springer London, 2008. ISBN 9781848820593.

Seng W. F. and Barnes P. A. Calculations of tungsten silicide and carbide formation on SiC using the Gibbs free energy. *Materials Science and Engineering: B*, 72(1):13–18, 2000.

Sequeira C. A. C. and Amaral L. Role of Kirkendall effect in diffusion processes in solids. *Transactions of nonferrous metals society of China*, 24(1):1–11, 2014.

Sharma A., Kumar P., Singh B., Chaudhuri S. R. and Ghosh S. Capacitance-voltage characteristics of organic Schottky diode with and without deep traps. *Applied physics letters*, 99(2), 2011.

Shul R. J. *Wide-bandgap electronic devices: symposium held April 24-27, 2000, San Francisco, California, USA*, volume 622. Materials Research Society, 2001. ISBN 9781558995307.

Simoen E., Lauwaert J. and Vrielinck H. Analytical techniques for electrically active defect detection. *Defects in semiconductors*, 91, *Semiconductors and semimetals*, pages 205 – 250. Elsevier, 2015.

Smith Z. E. and Wagner S. Band tails, entropy, and equilibrium defects in hydrogenated amorphous silicon. *Physical review letters*, 59(6):688, 1987.

Son N. T., Trinh X. T., Løvlie L. S., Svensson B. G., Kawahara K., Suda J., Kimoto T., Umeda T., Isoya J., Makino T., *et al* . Negative-U system of carbon vacancy in 4H-SiC. *Physical review letters*, 109(18):187603, 2012.

Sorieul S., Costantini J. M., Gosmain L., Thom´e L., and Grob J. J. Raman spectroscopy study of heavy-ion-irradiated α-SiC. *Journal of physics: Condensed matter*, 18(22):5235, 2006.

Sorieul S., Kerbiriou X., Costantini J., Gosmain L., Calas G., and Trautmann C. Optical spectroscopy study of damage induced in 4H-SiC by swift heavy ion irradiation. *Journal of physics: Condensed matter*, 24(12):125801, 2012.

Storasta L., Bergman J. P., Janz´en E., Henry A., and Lu J. Deep levels created by low energy electron irradiation in 4H-SiC. *Journal of applied physics*, 96(9): 4909–4915, 2004.

Storasta L., Tsuchida H., Miyazawa T., and Ohshima T. Enhanced annealing of the $Z_{1/2}$ defect in 4H-SiC epilayers. *Journal of applied physics*, 103(1):013705, 2008.

S¨udkamp T. and Bracht H. Self-diffusion in crystalline silicon: A single diffusion activation enthalpy down to 755 °C. *Physical review B*, 94:125208, 2016.

Sukkaew P., Danielsson O. and Ojam¨ae L. Growth mechanism of SiC CVD-surface etching by H_2, H atoms and HCl. *The Journal of physical chemistry. A*, 112:2503–2512, 2018.

Sze S. and Kwong K. *Metal-semiconductor contacts*. John Wiley and Sons, Inc., 2006.

Thabethe T. T., Njoroge E. G., Hlatshwayo T. T., Ntsoane T. and Malherbe J. B. Surface and interface structural analysis of W deposited on 6H–SiC substrates annealed in argon. *RSC advances*, 7(1):2–7, 2017.

Thang X. *Electron paramagnetic resonance studies of point defects in AlGaN and SiC*. Linköping studies in science and technology. Linköping University Electronic Press, 2015. ISBN 9789175190648.

Tilley R. J. D. *Defects in solids*. John Wiley & Sons, 2008. ISBN 9780470380734.

Toporski J., Dieing T. and Hollricher O. *Confocal raman microscopy*. Springer Series in Surface Sciences. Springer International Publishing, 2018. ISBN 9783319753805.

Trinh X. T., Sz´asz K., Hornos T., Kawahara K., Suda J., Kimoto T., Gali A., Janz´en E. and Son N. T. Negative-U carbon vacancy in 4H-SiC: Assessment of charge correction schemes and identification of the negative carbon vacancy at the quasicubic site. *Physical review B*, 88(23):235209, 2013.

Tunhuma S. M., Auret F. D., Legodi M. J., and Diale M. The effect of high temperatures on the electrical characteristics of Au/n-GaAs schottky diodes. *Physica B: Condensed matter*, 480:201–205, 2016.

Tunhuma S., Auret F., Legodi M., and Diale ,M. Electrical characterisation of 5.4 MeV alpha-particle irradiated; low doped, n-type gallium arsenide. pages 136–140, 2016. *Proceedings of SAIP 2015*, SAIP 2015, 136-140 ISBN 9780620707145

van Rensburg P. J., Auret F. D., Matias V. and Vantomme A. Electrical characterization of rare-earth implanted GaN. *Physica B: Condensed matter*, 404(22): 4411–4414, 2009.

Volpi F., Peaker A. R., Berbezier I. and Ronda A. Electrically active defects induced by sputtering deposition on silicon: The role of hydrogen. *Journal of applied physics*, 95(9):4752–4760, 2004.

Vorel P. and ˇCervinka D. High-power charger for super-el electric passenger car. *ECS Transactions*, 48(1):237–244, 2014.

Ward Y., Young R. J., and Shatwell R. A. Application of Raman microscopy to the analysis of silicon carbide monofilaments. *Journal of materials science*, 39(22): 6781–6790, 2004.

Waseda Y., Matsubara E., and Shinoda K. *X-Ray diffraction crystallography: Introduction, examples and solved problems*. Springer Berlin Heidelberg, 2011. ISBN 9783642166358.

Wilhelm C., Kranzer D. and Burger B. Development of a highly compact and efficient solar inverter with silicon carbide transistors. *2010 6th International Conference on Integrated Power Electronics Systems (CIPS)*, 1–6. IEEE, 2010.

Yeom H., Maier B., Mariani R., Bai D., Fronek S., Xu P. and Sridharan K. Magnetron sputter deposition of zirconium-silicide coating for mitigating high temperature oxidation of zirconium-alloy. *Surface and coatings technology*, 316:30–38, 2017.

Yue-Hu W., Yi-Men Z., Yu-Ming Z., Qing-Wen S., and Ren-Xu J. Al/Ti/4H-SiC Schottky barrier diodes with inhomogeneous barrier heights. *Chinese physics B*, 20 (8):087305, 2011.

Zhang J., Storasta L., Bergman J. P., Son N. T., and Janz´en E. Electrically active defects in n-type 4H-SiC grown in a vertical hot-wall reactor. *Journal of applied physics*, 93(8):4708–4714, 2003.

Zhang X., Miyazawa T. and Tsuchida H. Critical conditions of misfit dislocation formation in 4H-SiC epilayers. In *Materials science forum*, 717, 313–318. Trans Tech Publ, 2012.

Zhang Y., Sachan R., Pakarinen O. H., Chisholm M. F., Liu P., Xue H., and Weber W. J. Ionization-induced annealing of pre-existing defects in silicon carbide. *Nature communications*, 6:8049, 2015.

Zhu H., Qi Q., and Shi L. SiC nanorods of highly preferred orientation prepared by radio frequency magnetron sputtering. *Journal of vacuum science & technology B*, 31(6):060604, 2013.

Ziegler J. F., Ziegler M. D., and Biersack J. P. SRIM–the stopping and range of ions in matter (2010). *Nuclear instruments and methods in physics research section B: Beam interactions with materials and atoms*, 268(11-12):1818–1823, 2010.

Zohta Y. and Watanabe M. O. On the determination of the spatial distribution of deep centers in semiconducting thin films from capacitance transient spectroscopy. *Journal of applied physics*, 53(3):1809–1811, 1982.

Appendix A : Summary of prominent defects in 4*H*-SiC

Defect label	$E_T \pm 0.02$ (eV)	Defect ID	Nature	Origin
$E_{0.09}$	0.09	N	impurity	growth
$E_{0.13}$	0.13	Ti	impurity	growth
$E_{0.15}$	0.15	Ti	impurity	growth
Z_1	0.43	Z_1	donor	growth
Z_1	0.61 – 0.66	Z_1	acceptor	growth
Z_2	0.46	Z_2	donor	growth
Z_2	0.69	Z_2	acceptor	growth